Truncation Analysis and Numerical Method Improvements for the Thermal Radiative Transfer Equations

by

Jesse R. Cheatham

A dissertation submitted in partial fulfillment
of the requirements for the degree of
Doctor of Philosophy
(Nuclear Engineering and Radiological Sciences)
in The University of Michigan
2010

Doctoral Committee:

Professor James P. Holloway, Co-Chair
Professor William R. Martin, Co-Chair
Professor Paul R. Drake
Professor Edward W. Larsen
Forrest Brown

A paper is never finished, only abandoned. — Todd Palmer

to my parents Tom and Pat Gipson & Dick and Pam Cheatham

Acknowledgments

I would like to thank my entire family for their support, guidance and wisdom over the years on a host of topics. In particular, Gary and Lynn Kenworthy for their countless efforts to make Michigan a home away from home for me.

I wish to also acknowledge my advisers James Holloway and William Martin whose guidance was indispensable for my research. It was a pleasure to work with both of them.

I would like to thank the many students from Michigan for all the laughs and support. Notably, Greg "F" Davidson (assuming the continued existence of youTube http://www.youtube.com/watch?v=EfpTbXpW6-E) and Seth Johnson for their incredible help with my C++ questions. I would also like to thank Troy Becker for his conceptual help in mathematical methods and farming.

Finally, I would like to thank Christina Anderson for her continued support of my efforts to graduate.

Contents

List of Tables

List of Figures

Figure

Chapter 1

Introduction

Heat transfer is usually dominated by conduction and convection processes. However, at sufficiently high material temperatures, it becomes necessary to add another mode of heat transfer called Thermal Radiative Transfer (TRT). It is known that materials in equilibrium emit photons with a power proportional to T^4, where T is material temperature. Because of this rapid growth of emitted power with increasing material temperature, at high temperatures TRT will dominate the heating and cooling of a material over both conduction and convection.

The Thermal Radiative Transfer process couples the heating and cooling of a material by the absorption and emission of photons by a material. This results in two equations, one for the transportation (absorption and scattering) of photons and the other for the emission of photons. In this thesis we will omit any consideration of scattering as a simplification. These equations can be recast so that there are two fundamental unknowns that describe the radiation field and the temperature of the material, which is assumed to be in local thermodynamic equilibrium (LTE). The material equation and the radiative field equation are coupled together by absorption and emission of radiation.

1.1 Radiative Transfer Equations

In radiative transport, energy is transfered by photons that are emitted from material at one location and absorbed by material in another location. To understand this process, it is worthwhile to consider the example of a stellar atmosphere with a particle density $N = 10^{16}\text{cm}^{-3}$, implying an average distance between atoms of $\approx 3 \times 10^{-6}\text{cm}$ (14). The large atomic density makes it currently impossible to create a model that

can treat every particle exactly. This implies that any practical solution to radiative transfer problems must use a statistical approach to the interaction of photons and matter. Therefore a probabilistic description of photon interaction is introduced as an opacity (or cross-section) which is defined as the probability to interact per cm traveled.

The de Broglie wavelength of the photon is small compared to the particle spacing of the material (14). Therefore, a photon will travel in a straight line to the next interaction without changing frequency or energy. Photon-material absorption mechanisms of interest are those of photon-electron interactions. These interactions include line absorption, photoelectric effect, and photon absorption by free state electrons. Compton scattering has been omitted as one of the simplifications used in this thesis, but is typically considered in production level codes. At higher energies, additional material interactions can occur like nuclear excitation and pair-production but these are "seldom of interest in usual radiative transfer problems" (17).

To simplify the relationship between the radiation field and the material, local thermodynamic equilibrium (LTE) is assumed. LTE means that "the matter is in thermal equilibrium at the temperature T, emitting photons in a Planckian spectrum (with temperature T), and the radiation field, which may be far from equilibrium, does not affect this thermal equilibrium."(11) The LTE assumption also allows for the absorption and emission coefficients of the material to be related through the Planck function (17).

A photon traveling through phase space is described using:

$$\boldsymbol{x} = \text{particle location (three variables)} \tag{1.1}$$

$$\boldsymbol{\Omega} = \text{particle direction of movement (two variables)} \tag{1.2}$$

$$\nu = \text{particle frequency (one variable)} \tag{1.3}$$

$$t = \text{time (one variable).} \tag{1.4}$$

The combination of the above seven variables describes the phase space in which a photon resides while traveling at the speed of light, c. A photon can leave its differential phase space volume dV by leaking spatially or interacting with an electron. Photons may enter the phase space dV by streaming into the phase space spatially or

by being emitted from the material into the phase space. The material is assumed to be purely absorbing so that there is no scattering. The combination of these processes represents the gains and losses of photons within a phase space volume.

By balancing these processes, the equations of radiation transfer may be stated as (17)

$$\frac{1}{c}\frac{dI(\boldsymbol{x},\boldsymbol{\Omega},\nu,t)}{dt}+\boldsymbol{\Omega}\cdot\nabla I(\boldsymbol{x},\boldsymbol{\Omega},\nu,t)+\sigma(\boldsymbol{x},\nu,T)I(\boldsymbol{x},\boldsymbol{\Omega},\nu,t)=\sigma(\boldsymbol{x},\nu,T)B(\nu,T)+q \tag{1.5}$$

$$\frac{dU_m(\boldsymbol{x},t)}{dt}=\int_0^{4\pi}\int_0^{\infty}\sigma(\boldsymbol{x},\nu,T)(I(\boldsymbol{x},\boldsymbol{\Omega},\nu,t)-B(\nu,T))d\nu d\boldsymbol{\Omega} \tag{1.6}$$

where

$$\begin{aligned}
I(\boldsymbol{x},\boldsymbol{\Omega},\nu,t) &= ch\nu n(\boldsymbol{x},\boldsymbol{\Omega},\nu,t) && (1.7)\\
&= \text{Specific Intensity (keV / (steradians } \cdot cm^2\cdot \text{ s))},\\
n(\boldsymbol{x},\boldsymbol{\Omega},\nu,t) &= \text{Number of photons in a unit phase space,} && (1.8)\\
h &= 4.135667\times 10^{-18}(\text{keV}\cdot\text{s}) = \text{Planck's constant,} && (1.9)\\
c &= 299,792,458 \text{ meters per second} = \text{speed of light,} && (1.10)\\
B(\nu,T) &= \frac{2h\nu^3}{c^2}(e^{\frac{h\nu}{T}}-1)^{-1} = \text{Planck's function for radiation,} && (1.11)\\
T=T(\boldsymbol{x},t) &= \text{Material temperature (keV)} && (1.12)\\
\sigma(\boldsymbol{x},\nu,T) &= \text{Opacity (probability of absorption per cm),} && (1.13)\\
U_m(\boldsymbol{x},t) &= \rho\int_0^T C_v(\boldsymbol{x},T)dT = \text{Material energy density,} && (1.14)\\
C_v(\boldsymbol{x},T) &= \text{Specific heat capacity of material (keV / (g}\cdot\text{ keV)),} && (1.15)\\
\rho &= \text{Material density (g / } cm^3) = 1 \text{ in this thesis,} && (1.16)\\
q(\boldsymbol{x},\nu,t) &= \text{External source.} && (1.17)
\end{aligned}$$

Equation (1.5) represents the photon transport equation while Eq. (1.6) represents the material energy density equation. The equilibrium radiation energy density, $U_r(\boldsymbol{x},t)$ is defined as

$$U_r(\boldsymbol{x},t)=\frac{4\pi}{c}\int_0^{\infty}B(\nu,T)d\nu=aT^4 \tag{1.18}$$

with the radiation constant a

$$a=\frac{8k^4\pi^5}{15c^3h^3} \tag{1.19}$$

where

$$k = 8.617343 \times 10^{-5}\text{eV per Kelvin} = \text{Boltzmann's constant.} \tag{1.20}$$

The equilibrium radiation density can also be described in terms of the number density $n(\boldsymbol{x}, \boldsymbol{\Omega}, \nu, t)$ as

$$U_r(\boldsymbol{x}, t) = \int_0^\infty \int_{4\pi} h\nu n(\boldsymbol{x}, \boldsymbol{\Omega}, \nu, t) d\Omega d\nu.$$

In other words, both the specific radiation intensity and the equilibrium radiation density can be described by modeling individual particles, a necessity for Monte Carlo transport. Because they are both monotonic functions of temperature, the equilibrium radiation energy density, $U_r(\boldsymbol{x}, t)$, and the material energy density, $U_m(\boldsymbol{x}, t)$, can be related (11) by defining the quantity $\beta(\boldsymbol{x}, t)$ as

$$\frac{dU_m(\boldsymbol{x}, t)}{dU_r(\boldsymbol{x}, t)} = \frac{1}{\beta(\boldsymbol{x}, t)}, \tag{1.21}$$

which allows the thermal radiative transfer material energy density equation to be recast as

$$\frac{1}{\beta(\boldsymbol{x}, t)} \frac{dU_r(\boldsymbol{x}, t)}{dt} = \int_0^{4\pi} \int_0^\infty \sigma(\boldsymbol{x}, \nu, T)(I(\boldsymbol{x}, \boldsymbol{\Omega}, \nu, t) - B(\nu, T)) d\nu d\boldsymbol{\Omega}. \tag{1.22}$$

It is worthwhile to note that Eqs. (1.6) and (1.22) are mathematically equivalent. However, to solve the coupled thermal radiative transfer equations, approximations will be made that will make the two equations mathematically different.

1.1.1 Gray Thermal Radiative Transfer in One-Dimension

The seven independent variables make the TRT equations computationally intensive to solve, and therefore not conducive to numerical solution even in the presence of a supercomputer. We will assume a 1D semi-infinite slab geometry for most of this thesis since it will capture the temporal and spatial discretizations that are of interest. The vector $\boldsymbol{x}$ is now one variable denoted by x, instead of three. Similarly, $\boldsymbol{\Omega}$ may now be expressed as only one angular variable, $\mu = \cos\theta$ where θ is the angle measured from the positive x direction. Finally, the opacities are assumed to be independent of the frequency of the photon. Defining

$$\int_0^\infty I(x, \mu, \nu, t) d\nu = I(x, \mu, t) \tag{1.23}$$

yields the 1D Gray Thermal Radiative Transfer (GTRT) equations

$$\frac{1}{c}\frac{dI(x,\mu,t)}{dt}+\mu\frac{dI(x,\mu,t)}{dx}+\sigma(x,T)I(x,\mu,t)=\frac{1}{2}\sigma(x,T)U_r(x,t)+\frac{Q}{2} \tag{1.24}$$

$$\frac{dU_m(x,t)}{dt}+\sigma(x,T)U_r(x,t)=\sigma(x,T)\int_{-1}^{1}I(x,\mu,t)d\mu \tag{1.25}$$

$$\frac{1}{\beta(x,t)}\frac{dU_r(x,t)}{dt}+\sigma(x,T)U_r(x,t)=\sigma(x,T)\int_{-1}^{1}I(x,\mu,t)d\mu. \tag{1.26}$$

Equations (1.24) and (1.26) represent a coupled system of equations that can be solved for two unknowns U_r and I. However, this system of equations still has very strong non-linearities in the definitions of both σ and β, which can both depend on temperature. Although there exist non-physical problems that will remove these non-linearities, in this dissertation solution methods are sought for the general case.

Typically, the values of β and σ are fixed at the beginning of a time step as

$$\beta(x,t)\approx\beta(x,t_n)=\beta_n(x) \tag{1.27}$$

$$\sigma(x,t)\approx\sigma(x,t_n)=\sigma_n(x) \tag{1.28}$$

and then held constant over a time step Δt. Fixing β to a specific value makes Eqs. (1.25) and (1.26) mathematically different. Therefore Eq. (1.26) is used for the solution of the specific intensity I but Eq. (1.25) is required for the conservation of energy in the material energy update.

1.1.2 Gray Thermal Radiative Transfer in Zero-Dimension

To examine the truncation error associated with the time approximations made to both β and σ, a detailed truncation analysis via Taylor expansion has been conducted on two different solution methods for the TRT equations. The Carter-Forrest (CF) method (10), which solves the TRT equations exactly for a time step (excepting the constant β and σ approximations), and the Implicit Monte Carlo (IMC) method (5) which is the current industry standard for the solution of the TRT equations. For simplicity, the analysis of the GTRT equations will be conducted in 0D with no source since there is no time dependent truncation in either the source or the spatial leakage. For clarification the internal arguments will be suppressed except the time dependent

variables. Finally, defining the angle integrated specific intensity as

$$\int_{-1}^{1} I(x,\mu,t)d\mu = \phi(x,t) \tag{1.29}$$

the 0D radiative transfer equations are defined as

$$\frac{1}{c}\frac{d\phi(t)}{dt} + \sigma(t)\phi(t) = c\sigma(t)U_r(t) \tag{1.30}$$

$$\frac{dU_m(t)}{dt} + c\sigma(t)U_r(t) = \sigma(t)\phi(t) \tag{1.31}$$

$$\frac{1}{\beta(t)}\frac{dU_r(t)}{dt} + c\sigma(t)U_r(t) = \sigma(t)\phi(t). \tag{1.32}$$

When solving the TRT equations in any form, a certain number of simplifying approximations must be made. The typical approach is to find a solution to Eq. (1.32) for $U_r(t)$, then substitute that result into Eq. (1.30). This usually requires the values of $\beta(t)$ and $\sigma(t)$ to be evaluated at the beginning of the time step and then held constant over the calculation. Next, Eq. (1.30) is solved as a linear radiation transport problem for the absorption of photons. Finally, the Material Balance Equation (1.31) is solved to update the material temperature. The updated material temperature is then used to update the values of $\beta(t)$ and $\sigma(t)$ to be used in the next time step.

How the solution to $U_r(t)$ is calculated will differentiate the two methods that will be discussed in this thesis. The current approach is the Implicit Monte Carlo (IMC) method (5) which was created in 1971. While Monte Carlo is in the title of this method, the IMC assumptions can also be implemented in a deterministic code. The IMC method has proven to be robust in a host of problems in arriving at the equilibrium solution. More recently however, there has been a focus on the stability issues of the IMC method as well as ways to try and improve its accuracy (20).

An alternative method called the Carter-Forest (CF) method (10) was proposed in 1973 and makes fewer approximations than the IMC method. In particular the CF method more accurately treats the transport of photons within a time step than the IMC method. However, the CF method was never adopted due to being more computationally expensive than the IMC method while not giving a significant improvement in accuracy to warrant a new code development effort.

1.2 Thesis Synopsis

While the Implicit Monte Carlo has been used for a number of years, there has been little work to identify the sources of error that occur due to its approximations. In this thesis, we will explore the effect of these assumptions and how the error associated with them will propagate through the solution. After the sources of error have been identified, methods will be suggested for the reduction of the effect of these errors. This thesis will be organized as follows:

Chapter 2: Error Associated with the Solutions to the Gray Thermal Radiative Transfer Equations

For simplified, zero dimensional results there exists an exact solution for the Gray Thermal Radiative Transfer equations. This exact solution will be used to determine the bias in the IMC method. Next, a detailed truncation error analysis (in time) will be conducted to show how the approximations used to solve the GTRT equations will propagate. These results will give insight into how predictor-corrector methods may be employed to change the order of the accuracy of the solution.

Chapter 3: Zero Dimensional Numerical Results

Here we will show numerical results and compare them to the analytical work of the previous chapter. We will graphically demonstrate the bias in the IMC method as well as the effect of employing predictor-corrector techniques. These predictor-corrector techniques will demonstrate the ability to change the order of accuracy of both the IMC and CF method. Furthermore, the numerical results will show definitively the $O(\Delta t)$ sources of global error and how they can be removed.

Chapter 4: 1D Radiative Transfer

The introduction of a spatial dependence in the GTRT equations will add another source of error known as "Photon Teleportation". The effects of this error will be examined and Functional Expansion Tallies (FET's) will be introduced to reduce this error. Next, the predictor-corrector scheme will be examined in a more realistic problem and a variable-weight predictor-corrector scheme will be examined to reduce the computation time.

Chapter 5: Time Step Controllers

Knowing the leading sources of time truncation error from the previous truncation analysis, a time step controller is proposed to control it. The resulting controller is then compared to two different approaches that are currently implemented. Then, predictor-corrector methods are combined with a time step controller to make the most of both methods. The predictor step can be used to estimate the correct time step size to be used in the corrector step while also updating pertinent information to improve accuracy in the solution.

Chapter 6: Conclusions and Future Work

Finally we discuss the results presented in this thesis to give a larger perspective on the work. We will also discuss future work that could be continued.

Chapter 2

Error Associated with the Solutions to the Gray Thermal Radiative Transfer Equations

To solve the nonlinear TRT equations, a couple of simplifying approximations are required. Each time that an approximation is made, a new source of error is added to the solution of the equations. To understand and quantify these errors, it is necessary to build models that can isolate and quantify the error produced by a certain approximation. For this purpose, a simple zero dimensional Gray problem allows for the isolation of the IMC approximations and the temporal approximations that are made to both $\beta(t)$ and $\sigma(t)$.

2.1 Residual Error Analysis of the Zero Dimensional Gray TRT Linear Problem

To determine the effect of the IMC approximations, an artificial problem is proposed. When both the $\sigma(t)$ and $\beta(t)$ terms are constant with respect to time, the zero dimensional TRT equations become linear. Under these conditions the CF solution to the linear 0-D TRT problem is exact, while the IMC results are an approximation. While this problem is not physically meaningful, it allows for the isolation of the IMC approximations compared to the exact solution. By performing a residual analysis of the solutions to the CF and IMC methods, the error of the IMC method can be quantified. There has been no previous quantification of this error.

The analytic solution (12) to the Carter-Forest formulation of the Gray RT equa-

tions yields

$$\phi(t_{n+1})_{CF} = \phi(t_n) + \frac{c^2\sigma\beta Q_o\Delta t}{\gamma} + \left[\frac{c^2\sigma}{\gamma}U_r(t_n) - \frac{c\sigma}{\gamma}\phi(t_n)\right](1-e^{-\gamma\Delta t}) \\ - \left[\frac{cQ_o}{\gamma} - \frac{c^2\sigma\beta Q_o}{\gamma^2}\right](1-e^{-\gamma\Delta t}) \tag{2.1}$$

where $\gamma = c\sigma(1+\beta)$. It is worth noting that in this particular problem, the solution to the CF method is exact while the Implicit Monte Carlo (IMC) analytic solution (16),

$$\phi(t_{n+1})_{IMC} = \phi(t_n)e^{-c\sigma f(\Delta t)} + [cU_r(t_n) + \frac{Q_o}{\sigma f}]\left(1 - e^{-c\sigma f(\Delta t)}\right) \tag{2.2}$$

is an approximation. The residual error of the IMC is determined to by subtracting the IMC estimate of $\phi(t_{n+1})$ from the CF value of $\phi(t_{n+1})$ to quantify the error in the IMC approximations as

$$\begin{aligned}\phi_{CF}(t_{n+1}) - \phi_{IMC}(t_{n+1}) = \phi(t_n) &+ \frac{c^2\sigma\beta Q_o\Delta t}{\gamma} + \frac{c^2\sigma}{\gamma}U_r(t_n) - \frac{c\sigma}{\gamma}\phi(t_n) \\ &+ \frac{cQ_o}{\gamma} - \frac{c^2\sigma\beta Q_o}{\gamma^2} - \frac{c^2\sigma}{\gamma}U_r(t_n)e^{-\gamma\Delta t} + \frac{c\sigma}{\gamma}\phi(t_n)e^{-\gamma\Delta t} \\ &- \frac{cQ_o}{\gamma}e^{-\gamma\Delta t} + \frac{c^2\sigma\beta Q_o}{\gamma^2}e^{-\gamma\Delta t} - \phi(t_n)e^{-c\sigma f\Delta t} \\ &- cU_r(t_n) + cU_r(t_n)e^{-c\sigma f\Delta t} - \frac{Q_o}{\sigma f} + \frac{Q_o}{\sigma f}e^{-c\sigma f\Delta t}.\end{aligned} \tag{2.3}$$

Similar terms are grouped from Eq. (2.3) as follows

$$R_\phi = \phi(t_n) - \frac{c\sigma}{\gamma}\phi(t_n) + \frac{c\sigma}{\gamma}\phi(t_n)e^{-\gamma\Delta t} - \phi(t_n)e^{-c\sigma f\Delta t}. \tag{2.4}$$

Expanding around $\Delta t = 0$, the exponentials may be rewritten as

$$e^{-\gamma\Delta t} = 1 - \gamma\Delta t + \frac{\gamma^2\Delta t^2}{2} + O(\Delta t^3) \tag{2.5}$$

and

$$e^{-c\sigma f\Delta t} = 1 - c\sigma f\Delta t + \frac{c^2\sigma^2 f^2\Delta t^2}{2} + O(\Delta t^3). \tag{2.6}$$

Substituting Eqs. (2.6) and (2.5) into (2.4) yields

$$R_\phi = c\sigma\phi(t_n)\Delta t\left[(f-1) + \frac{\gamma\Delta t}{2} - \frac{c\sigma f^2\Delta t}{2}\right] + O(\Delta t^3). \tag{2.7}$$

Now, Taylor expand the Fleck factor with the assumption that $\alpha\beta c\sigma\Delta t \ll 1$ as

$$f = \frac{1}{1+\alpha\beta c\sigma\Delta t} = 1 - \alpha\beta c\sigma\Delta t + \frac{\alpha^2\beta^2c^2\Delta t^2}{2} + O(\Delta t^3). \tag{2.8}$$

Using the Fleck factor expansion and neglecting terms that are $O(\Delta t^2)$, the residual for $\phi(t_n)$ terms becomes

$$R_\phi = c\sigma\phi(t_n)\Delta t\left[-\alpha\beta c\sigma\Delta t + \frac{\beta c\sigma\Delta t}{2}\right] + O(\Delta t^3). \tag{2.9}$$

Next, the source terms are grouped together as

$$R_{Q_o} = \frac{\beta c^2\sigma Q_o\Delta t}{\gamma} + \frac{cQ_o}{\gamma} - \frac{\beta c^2\sigma Q_o}{\gamma^2} - \frac{cQ_o}{\gamma}e^{-\gamma\Delta t} + \frac{\beta c^2\sigma Q_o}{\gamma^2}e^{-\gamma\Delta t} - \frac{Q_o}{\sigma f} + \frac{Q_o}{\sigma f}e^{-c\sigma f\Delta t}. \tag{2.10}$$

Expanding the exponentials by using Eqs. (2.5) and (2.6) yields

$$R_{Q_o} = \frac{\beta c^2\sigma Q_o\Delta t^2}{2} - \frac{cQ_o\gamma\Delta t^2}{2} + \frac{c^2\sigma f Q_o\Delta t^2}{2} + O(\Delta t^3), \tag{2.11}$$

which is simplified again by expanding the Fleck factor f to give the expected small truncation error result

$$R_{Q_o} = O(\Delta t^3). \tag{2.12}$$

Finally, the $U_r(t_n)$ terms are grouped together as

$$R_{U_r} = \frac{c^2\sigma}{\gamma}U_r(t_n) - \frac{c^2\sigma}{\gamma}U_r(t_n)e^{-\gamma\Delta t} - cU_r(t_n) + cU_r(t_n)e^{-c\sigma f\Delta t}. \tag{2.13}$$

Simplify by expanding the exponentials in Eq. (2.13) to get

$$R_{U_r} = c^2\sigma U_r(t_n)\Delta t - \frac{c^2\sigma\gamma\Delta t^2}{2}U_r(t_n) - c^2\sigma f\Delta t U_r(t_n) + \frac{c^3\sigma^2f^2\Delta t^2}{2}U_r(t_n) + O(\Delta t^3), \tag{2.14}$$

and expanding the Fleck factor f will yield the final U_r residual,

$$R_{U_r} = \alpha\beta c^3\sigma^2\Delta t^2U_r(t_n) - \frac{\beta c^3\sigma^2\Delta t^2}{2}U_r(t_n) + O(\Delta t^3). \tag{2.15}$$

Combining the residual terms from Eqs. (2.9), (2.12), and (2.15) yields the local

residual error of the IMC equations

$$R = \alpha\beta c^3\sigma^2\Delta t^2 U_r(t_n) - \frac{\beta c^3\sigma^2\Delta t^2}{2}U_r(t_n) + \frac{\beta c^2\sigma^2\Delta t^2\phi(t_n)}{2} - \alpha\beta c^2\sigma^2\Delta t^2\phi(t_n) + O(\Delta t^3). \tag{2.16}$$

Local error is the result of taking one time step from the initial conditions. However, this local error accumulates through the course of the simulation. After taking a second time step away from the initial conditions, the numerical solution has an error of $2O(\Delta t^m)$ where m is the order of the method. Over the course of a simulation, the local error accumulates as (6)

$$\sum_1^n \text{Error} = \sum_1^n O(\Delta t^m) = nO(\Delta t^m) \tag{2.17}$$

where n is the number of time steps used to get to time t_n. Assuming a uniformly distributed time mesh, the number of steps n can be described as $n = (t_n - t_o)/\Delta t$. Replacing the value of n in Eq. (2.17) gives the global error at time t_n as

$$\text{Total Error} = \frac{t_n - t_o}{\Delta t}O(\Delta t^m) = O(\Delta t^{m-1}). \tag{2.18}$$

In short, the accumulation of local truncation error builds up over multiple times steps decreasing the accuracy of the method on the global scale. In numerical simulations, it is the global error that counts since it dictates the accuracy of the final numerical solution.

In the case of $\alpha = 1$ the local residual error term may be simplified to

$$R = c^2\beta\sigma^2\Delta t^2\left[c\frac{U_r(t_n)}{2} - \frac{\phi(t_n)}{2}\right]. \tag{2.19}$$

If $\alpha = 0.5$ the residual terms in Eq. (2.16) clearly cancel out yielding

$$R = O(\Delta t^3) \tag{2.20}$$

and when $\alpha = 0$

$$R = c^2\beta\sigma^2\Delta t^2\left[\frac{\phi(t_n)}{2} - c\frac{U_r(t_n)}{2}\right]. \tag{2.21}$$

Eqs. (2.19) to (2.21) shows the local residual error after a time step for a given value of α. The result for $\alpha = 0.5$ is a special case since the order of the residual error in the method changes. This result is expected since Mosher has already demonstrated that the solution to the IMC equation would be $O(\Delta t^2)$ accurate numerically in a

linear 0-D problem without explanation (16).

The residual error analysis also yields a non-intuitive result. One of the IMC approximations assumes an instantaneous re-emission of photon absorptions, a nonphysical process. However, since the residual error depends only on α, the approximation that all emissions occur instantaneously is not a dominant source of error in the IMC approximations. Numerical results exist that confirm this explanation since Wollaber was able to achieve $O(\Delta t^2)$ accuracy in a linear 0D Gray problem using a time dependent fleck factor (20) with instantaneous emissions. These results will also be confirmed in Chapter 3 using the more traditional IMC implementation.

Since the industry practice is to set the value of $\alpha = 1$, we will examine the residual error that comes from that approximation in more detail. It is important to consider the types of problems being solved when examining the residual error. In particular, for warming problems where $\phi(t_n) \gg cU_r(t_n)$, the residual will be negative when setting $\alpha = 1$. In other words, the IMC method will store more energy in the photon field $\phi(t)$ than it should, leaving a cooler material temperature T. Conversely, if the problem is cooling when $\alpha = 1$ then the residual will be positive. A positive residual means that the IMC method will store less energy in the photon field $\phi(t)$ and more energy in the material giving a higher material temperature T. The results of the residual error will be exactly the opposite of $\alpha = 1$ if $\alpha = 0$, but no one ever uses $\alpha = 0$ in practice for stability concerns. Of course this residual error, hence forth called bias, is only of concern during a transient since at equilibrium $\phi(t_n) \approx cU_r(t_n)$, and the IMC bias vanishes.

This bias in the IMC method has never been examined before and we will show that it will have unintuitive effects to the accuracy of a numerical solution. As one might expect, the influence of the IMC bias will be the greatest during rapid transients with sources or at a Marshak wave front where the incident radiation is much higher than the material equilibrium radiation density. In some situations, this bias will improve the accuracy of the problem by canceling out other sources of error, but in general this bias will have detrimental effects for the accurate transport of radiation. Throughout this thesis numerical results can be seen of how the IMC method, with $\alpha = 1$, maintains a cooler material temperature than the CF method during rapid warming transients.

2.2 Detailed Truncation Error Analysis of the Carter-Forest and Implicit Monte Carlo Solutions to the Nonlinear TRT Equations

To fully understand the differences of the CF and IMC methods, a detailed truncation error analysis is conducted on the 0-D nonlinear GTRT equations. The addition of the truncation error associated with approximating both $\sigma(t)$ and $\beta(t)$ as constant over a time step significantly changes the accuracy of the Carter-Forest method. While the CF method is an exact solution for the linear GTRT equations, it is an approximation in the nonlinear GTRT equations. By examining the propagation of error in both the CF and IMC methods, a more intuitive feel can be developed about the limitations of each method.

2.2.1 Carter-Forest (CF) Truncation Error

Starting with the 0D radiative transfer equations with gray approximation

$$\frac{1}{c}\frac{d\phi(t)}{dt} + \sigma(t)\phi(t) = c\sigma(t)U_r(t) \tag{2.22}$$

$$\frac{1}{\beta(t)}\frac{dU_r(t)}{dt} + c\sigma(t)U_r(t) = \sigma(t)\phi(t) \tag{2.23}$$

equation (1.32) is solved exactly for $U_r(t)$ by integrating factor.

$$\frac{d}{dt'}\left[U_r(t')e^{\int_{t_n}^{t'} c\beta(t'')\sigma(t'')dt''}\right] = \phi(t')\beta(t')\sigma(t')e^{\int_{t_n}^{t'} c\beta(t'')\sigma(t'')dt''} \tag{2.24}$$

Integrating from t_n to t over dt'

$$U_r(t)e^{\int_{t_n}^{t} c\beta(t'')\sigma(t'')dt''} = U_r(t_n) + \int_{t_n}^{t} \phi(t')\beta(t')\sigma(t')e^{\int_{t_n}^{t'} c\beta(t'')\sigma(t'')dt''}dt' \tag{2.25}$$

then simplifying the equation for $U_r(t)$ and combining the bounds of integration for the two exponentials

$$U_r(t) = U_r(t_n)e^{\int_{t_n}^{t} -c\beta(t'')\sigma(t'')dt''} + e^{\int_{t_n}^{t} -c\beta(t'')\sigma(t'')dt''} \int_{t_n}^{t} \phi(t')\beta(t')\sigma(t')e^{\int_{t_n}^{t'} c\beta(t'')\sigma(t'')dt''} dt' \tag{2.26}$$

$$= U_r(t_n)e^{\int_{t_n}^{t} -c\beta(t'')\sigma(t'')dt''} + \int_{t_n}^{t} \phi(t')\beta(t')\sigma(t')e^{-\int_{t'}^{t} c\beta(t'')\sigma(t'')dt''} dt'.$$

Now, substituting equation (2.26) into equation (1.30) yields the exact expression for the photon intensity for the 0D and gray approximation radiative transfer as

$$\begin{aligned} \frac{1}{c}\frac{d\phi(t)}{dt} + \sigma(t)\phi(t) &= c\sigma(t)U_r(t_n)e^{-\int_{t_n}^{t} c\beta(t'')\sigma(t'')dt''} \\ &\quad + c\sigma(t)\int_{t_n}^{t} \beta(t')\sigma(t')\phi(t')e^{-\int_{t'}^{t} c\beta(t'')\sigma(t'')dt''} dt'. \end{aligned} \tag{2.27}$$

To solve this equation, $\sigma(t)$ and $\beta(t)$ are Taylor expanded around the value t_n yielding

$$\beta(t) = \beta(t_n) + \frac{d\beta(t_n)}{dt}(t - t_n) + O(\Delta t^2) \tag{2.28}$$

$$\sigma(t) = \sigma(t_n) + \frac{d\sigma(t_n)}{dt}(t - t_n) + O(\Delta t^2) \tag{2.29}$$

where $\beta(t_n) = \beta_n$ and $\sigma(t_n) = \sigma_n$. The $\frac{d\beta(t_n)}{dt}(t - t_n)$ and $\frac{d\sigma(t_n)}{dt}(t - t_n)$ terms are $O(\Delta t)$ terms that are followed explicitly through the truncation analysis. Now, substitute (2.28) and (2.29) into (2.27) then integrate over a time step to yield

$$\begin{aligned} \int_{t_n}^{t_{n+1}} \frac{1}{c}\frac{d\phi(t)}{dt}dt + \int_{t_n}^{t_{n+1}} \left[\sigma_n + \frac{d\sigma_n}{dt}(t - t_n) + O(\Delta t^2)\right]\phi(t)dt \\ = \int_{t_n}^{t_{n+1}} R(t)dt + \int_{t_n}^{t_{n+1}} S(t)dt \end{aligned} \tag{2.30}$$

where

$$R(t) = c\left[\sigma_n + \frac{d\sigma_n}{dt}(t - t_n) + O(\Delta t^2)\right] U_r(t_n)e^{-F(t)} \tag{2.31}$$

and

$$S(t) = c\left[\sigma_n + \frac{d\sigma_n}{dt}(t - t_n) + O(\Delta t^2)\right] \int_{t_n}^{t}\left[\beta_n + \frac{d\beta_n}{dt}(t^{'} - t_n)\right]\left[\sigma_n + \frac{d\sigma_n}{dt}(t^{'} - t_n)\right]\phi(t^{'})e^{-F(t,t^{'})}dt^{'} \tag{2.32}$$

with

$$F(t) = \int_{t_n}^{t} c\left[\beta_n + \frac{d\beta_n}{dt}(t^{''} - t_n)\right]\left[\sigma_n + \frac{d\sigma_n}{dt}(t^{''} - t_n)\right] + O(\Delta t^2)dt^{''} \tag{2.33}$$

$$F(t, t^{'}) = \int_{t^{'}}^{t} c\left[\beta_n + \frac{d\beta_n}{dt}(t^{''} - t_n)\right]\left[\sigma_n + \frac{d\sigma_n}{dt}(t^{''} - t_n)\right] + O(\Delta t^2)dt^{''}. \tag{2.34}$$

Each term in equation in (2.30) will be examined separately to determine the truncation error from the Taylor expansion approximation then combined back together to find the error in the estimate of ϕ.

The $\int_{t_n}^{t_{n+1}} \frac{1}{c}\frac{d\phi(t)}{dt}dt$ Term

With no approximation, this term is evaluated to yield

$$\int_{t_n}^{t_{n+1}} \frac{1}{c}\frac{d\phi(t)}{dt}dt = \frac{1}{c}\phi(t_{n+1}) - \frac{1}{c}\phi(t_n) \tag{2.35}$$

The $\int_{t_n}^{t_{n+1}}[\sigma_n + \frac{d\sigma_n}{dt}(t - t_n) + O(\Delta t^2)]\phi(t)dt$ Term

Simplifying this term will yield

$$\int_{t_n}^{t_{n+1}}[\sigma_n + \frac{d\sigma_n}{dt}(t - t_n) + O(\Delta t^2)]\phi(t)dt = \int_{t_n}^{t_{n+1}} \sigma_n\phi(t)dt + \int_{t_n}^{t_{n+1}} \frac{d\sigma_n}{dt}(t - t_n)\phi(t)dt + O(\Delta t^3) \tag{2.36}$$

Using the mean value theorem of integration which states

$$\int_a^b G(x)D(x)dx = G(x^*)\int_a^b D(x)dx \tag{2.37}$$

where

$$a \leq x^* \leq b. \tag{2.38}$$

Equation (2.36) can be rewritten as

$$\begin{aligned}\int_{t_n}^{t_{n+1}} [\sigma_n + \frac{d\sigma_n}{dt}(t-t_n) + O(\Delta t^2)]\phi(t)dt &= \int_{t_n}^{t_{n+1}} \sigma_n\phi(t)dt + \frac{d\sigma_n}{dt}\phi(t^*)\int_{t_n}^{t_{n+1}}(t-t_n)dt \\ &\quad + O(\Delta t^3) \\ &= \int_{t_n}^{t_{n+1}} \sigma_n\phi(t)dt + O(\Delta t^2)\end{aligned} \tag{2.39}$$

where

$$t_n \leq t^* \leq t_{n+1}. \tag{2.40}$$

Inherent in using the mean value theorem of integration is the assumption that $\phi(t)$ is a smooth, continuous function over the time step.

The $\int_{t_n}^{t_{n+1}} R(t)dt$ Term

The expression of $R(t)$ is still fairly complicated and will be evaluated in parts. First, the exponential will be evaluated for and then Taylor expanded such that,

$$\begin{aligned} e^{-F(t)} &= \exp\left[\int_{t_n}^{t} -c[\beta_n + \frac{d\beta_n}{dt}(t^{''}-t_n)][\sigma_n + \frac{d\sigma_n}{dt}(t^{''}-t_n)] + O(\Delta t^2)dt^{''}\right] \\ &= \exp\left[-c\beta_n\sigma_n(t-t_n) - \frac{c}{2}(\sigma_n\frac{d\beta_n}{dt} + \beta_n\frac{d\sigma_n}{dt})(t-t_n)^2 + O(\Delta t^3)\right] \\ &= \exp\left[-c\beta_n\sigma_n(t-t_n)\right]\exp\left[-\frac{c}{2}(\sigma_n\frac{d\beta_n}{dt} + \beta_n\frac{d\sigma_n}{dt})(t-t_n)^2 + O(\Delta t^3)\right]\end{aligned} \tag{2.41}$$

Now, Taylor expand the error portion of equation (2.41) to get a simplified expression of $e^{-F(t)}$. The error can be expanded as

$$\exp\left[-\frac{c}{2}(\sigma_n\frac{d\beta_n}{dt} + \beta_n\frac{d\sigma_n}{dt})(t-t_n)^2 + O(\Delta t^3)\right] = 1 - \frac{c}{2}(\sigma_n\frac{d\beta_n}{dt} + \beta_n\frac{d\sigma_n}{dt})(t-t_n)^2 + O(\Delta t^3) \tag{2.42}$$

which allows for the simplification

$$e^{-F(t)} = \exp\left[-c\beta_n\sigma_n(t-t_n)\right] + O(\Delta t^2). \tag{2.43}$$

Neglecting higher order errors, the integration of $R(t)$ can now be examined as

$$\begin{aligned}\int_{t_n}^{t_{n+1}} R(t)dt &= \int_{t_n}^{t_{n+1}} c\left[\sigma_n + \frac{d\sigma_n}{dt}(t-t_n) + O(\Delta t^2)\right] U_r(t_n)e^{-F(t)}dt \qquad (2.44)\\ &= \int_{t_n}^{t_{n+1}} c\left[\sigma_n + \frac{d\sigma_n}{dt}(t-t_n)\right] U_r(t_n)\times \\ &\qquad \left[1 - c(\sigma_n\frac{d\beta_n}{dt} + \beta_n\frac{d\sigma_n}{dt})(t-t_n)^2\right]\exp^{-c\beta_n\sigma_n(t-t_n)}\,dt \\ &= \int_{t_n}^{t_{n+1}} c\sigma_n U_r(t_n)\exp^{-c\beta_n\sigma_n(t-t_n)}\,dt \\ &+ \int_{t_n}^{t_{n+1}} c\frac{d\sigma_n}{dt}(t-t_n)U_r(t_n)\exp^{-c\beta_n\sigma_n(t-t_n)}\,dt + O(\Delta t^3)\end{aligned}$$

Expanding the exponential in the error term, Eq. (2.44) may be rewritten as

$$\begin{aligned}\int_{t_n}^{t_{n+1}} R(t)dt &= \int_{t_n}^{t_{n+1}} c\sigma_n U_r(t_n)\exp^{-c\beta_n\sigma_n(t-t_n)}\,dt \qquad (2.45)\\ &+ \int_{t_n}^{t_{n+1}} c\frac{d\sigma_n}{dt}(t-t_n)U_r(t_n)\exp^{-c\beta_n\sigma_n(t-t_n)}\,dt + O(\Delta t^3) \\ &= \int_{t_n}^{t_{n+1}} c\sigma_n U_r(t_n)\exp^{-c\beta_n\sigma_n(t-t_n)}\,dt \\ &+ c\frac{d\sigma_n}{dt}U_r(t_n)\int_{t_n}^{t_{n+1}}\left[(t-t_n) - c\beta_n\sigma_n(t-t_n)^2\right]dt + O(\Delta t^3) \\ &= \int_{t_n}^{t_{n+1}} c\sigma_n U_r(t_n)\exp^{-c\beta_n\sigma_n(t-t_n)}\,dt + O(\Delta t^2)\end{aligned}$$

The $\int_{t_n}^{t_{n+1}} S(t)dt$ Term

Now, the expression for $\int_{t_n}^{t_{n+1}} S(t)dt$ is expanded into the parts shown below

$$\begin{aligned}
\int_{t_n}^{t_{n+1}} S(t)dt = &\int_{t_n}^{t_{n+1}} \sigma_n \int_{t_n}^{t} \beta_n \sigma_n \phi(t^{'}) e^{-F(t,t^{'})} dt^{'} dt \\
&+ \int_{t_n}^{t_{n+1}} \sigma_n \int_{t_n}^{t} \beta_n \frac{d\sigma_n}{dt} (t^{'} - t_n) \phi(t^{'}) e^{-F(t,t^{'})} dt^{'} dt \\
&+ \int_{t_n}^{t_{n+1}} \sigma_n \int_{t_n}^{t} \frac{d\beta_n}{dt} (t^{'} - t_n) \sigma_n \phi(t^{'}) e^{-F(t,t^{'})} dt^{'} dt \\
&+ \int_{t_n}^{t_{n+1}} \sigma_n \int_{t_n}^{t} \frac{d\beta_n}{dt} \frac{d\sigma_n}{dt} (t^{'} - t_n)^2 \phi(t^{'}) e^{-F(t,t^{'})} dt^{'} dt \\
&+ \int_{t_n}^{t_{n+1}} \frac{d\sigma_n}{dt} (t - t_n) \int_{t_n}^{t} \beta_n \sigma_n \phi(t^{'}) e^{-F(t,t^{'})} dt^{'} dt \\
&+ \int_{t_n}^{t_{n+1}} \frac{d\sigma_n}{dt} (t - t_n) \int_{t_n}^{t} \beta_n \frac{d\sigma_n}{dt} (t^{'} - t_n) \phi(t^{'}) e^{-F(t,t^{'})} dt^{'} dt \\
&+ \int_{t_n}^{t_{n+1}} \frac{d\sigma_n}{dt} (t - t_n) \int_{t_n}^{t} \frac{d\beta_n}{dt} (t^{'} - t_n) \sigma_n \phi(t^{'}) e^{-F(t,t^{'})} dt^{'} dt \\
&+ \int_{t_n}^{t_{n+1}} \frac{d\sigma_n}{dt} (t - t_n) \int_{t_n}^{t} \frac{d\beta_n}{dt} \frac{d\sigma_n}{dt} (t^{'} - t_n)^2 \phi(t^{'}) e^{-F(t,t^{'})} dt^{'} dt
\end{aligned} \tag{2.46}$$

The expression of $S(t)$ will be broken down in a similar manner as $R(t)$ was done previously. First, the exponential is expanded to better characterize its error.

$$\begin{aligned}
e^{-F(t,t^{'})} &= \exp\left[- \int_{t^{'}}^{t} c[\beta_n + \frac{d\beta_n}{dt}(t^{''} - t_n)][\sigma_n + \frac{d\sigma_n}{dt}(t^{''} - t_n)] + O(\Delta t^2) dt^{''} \right] \qquad (2.47) \\
&= \exp\left[-c\beta_n \sigma_n (t - t^{'}) \right] \times \\
&\qquad \exp\left[-c(\sigma_n \frac{d\beta_n}{dt} + \beta_n \frac{d\sigma_n}{dt})(\frac{t^2}{2} - t t_n - \frac{t^{'2}}{2} + t_n t^{'}) + O(\Delta t^3) \right] \\
&= \exp\left[-c\beta_n \sigma_n (t - t^{'}) \right] \times \qquad (2.48) \\
&\qquad \exp\left[-\frac{c}{2}(\sigma_n \frac{d\beta_n}{dt} + \beta_n \frac{d\sigma_n}{dt})((t - t_n)^2 - (t^{'} - t_n)^2) + O(\Delta t^3) \right]
\end{aligned}$$

Taylor expanding the first order error of Eq. (2.47) around t_n with regard to $t^{'}$ yields

$$\exp\left[-\frac{c}{2}(\sigma_n\frac{d\beta_n}{dt}+\beta_n\frac{d\sigma_n}{dt})((t-t_n)^2-(t^{'}-t_n)^2)+O(\Delta t^3)\right] \tag{2.49}$$
$$\approx \exp\left[-\frac{c}{2}(\sigma_n\frac{d\beta_n}{dt}+\beta_n\frac{d\sigma_n}{dt})(t-t_n)^2\right]\left[1+\frac{c}{2}(\sigma_n\frac{d\beta_n}{dt}+\beta_n\frac{d\sigma_n}{dt})(t^{'}-t_n)^2+O(\Delta t^3)\right].$$

Next, expanding the error of Eq. (2.49) around t_n with regard to t results in

$$\begin{aligned}
&\exp\left[-\frac{c}{2}(\sigma_n\frac{d\beta_n}{dt}+\beta_n\frac{d\sigma_n}{dt})((t-t_n)^2-(t^{'}-t_n)^2)+O(\Delta t^3)\right] \qquad (2.50)\\
&=\left[1-\frac{c}{2}(\sigma_n\frac{d\beta_n}{dt}+\beta_n\frac{d\sigma_n}{dt})(t-t_n)^2+O(\Delta t^3)\right]\times\\
&\qquad\left[1+\frac{c}{2}(\sigma_n\frac{d\beta_n}{dt}+\beta_n\frac{d\sigma_n}{dt})(t^{'}-t_n)^2+O(\Delta t^3)\right]\\
&=1-\frac{c}{2}(\sigma_n\frac{d\beta_n}{dt}+\beta_n\frac{d\sigma_n}{dt})((t-t_n)^2-(t^{'}-t_n)^2)
\end{aligned}$$

therefore

$$e^{-F(t,t^{'})}\approx\exp\left[-c\beta_n\sigma_n(t-t^{'})\right]+O(\Delta t^2). \tag{2.51}$$

Expanding $e^{-F(t,t^{'})}$ and using the mean value theorem of integration, Eq. (2.46) can be rewritten as

$$\int_{t_n}^{t_{n+1}} S(t)dt = \int_{t_n}^{t_{n+1}} \sigma_n \int_{t_n}^{t} \beta_n\sigma_n\phi(t^{'}) \exp[-c\beta_n\sigma_n(t-t^{'})] + O(\Delta t^2)dt^{'}dt \tag{2.52}$$

$$+ \int_{t_n}^{t_{n+1}} \sigma_n\phi(t^{**})e^{-c\beta_n\sigma_n t}\beta_n\frac{d\sigma_n}{dt}\times$$

$$\int_{t_n}^{t}(t^{'}-t_n)\left[1+c\beta_n\sigma_n(t^{'}-t_n)+O(\Delta t^2)\right]dt^{'}dt$$

$$+ \int_{t_n}^{t_{n+1}} \sigma_n\phi(t^{**})e^{-c\beta_n\sigma_n t}\frac{d\beta_n}{dt}\sigma_n\times$$

$$\int_{t_n}^{t}(t^{'}-t_n)\left[1+c\beta_n\sigma_n(t^{'}-t_n)+O(\Delta t^2)\right]dt^{'}dt$$

$$+ \int_{t_n}^{t_{n+1}} \sigma_n\phi(t^{**})e^{-c\beta_n\sigma_n t}\frac{d\beta_n}{dt}\frac{d\sigma_n}{dt}\times$$

$$\int_{t_n}^{t}(t^{'}-t_n)^2\left[1+c\beta_n\sigma_n(t^{'}-t_n)+O(\Delta t^2)\right]dt^{'}dt$$

$$+ \int_{t_n}^{t_{n+1}} \frac{d\sigma_n}{dt}(t-t_n)\beta_n\sigma_n\phi(t^{**})\exp\left[-c\beta_n\sigma_n(t-t^{**})\right]+O(\Delta t^3)dt$$

$$+ \int_{t_n}^{t_{n+1}} \frac{d\sigma_n}{dt}(t-t_n)\phi(t^{**})e^{-c\beta_n\sigma_n t}$$

$$\times\beta_n\frac{d\sigma_n}{dt}\int_{t_n}^{t}(t^{'}-t_n)\left[1+c\beta_n\sigma_n(t^{'}-t_n)+O(\Delta t^2)\right]dt^{'}dt$$

$$+ \int_{t_n}^{t_{n+1}} \frac{d\sigma_n}{dt}(t-t_n)\phi(t^{**})e^{-c\beta_n\sigma_n t}$$

$$\times\frac{d\beta_n}{dt}\sigma_n\int_{t_n}^{t}(t^{'}-t_n)\left[1+c\beta_n\sigma_n(t^{'}-t_n)+O(\Delta t^2)\right]dt^{'}dt$$

$$+ \int_{t_n}^{t_{n+1}} \frac{d\sigma_n}{dt}(t-t_n)\phi(t^{**})e^{-c\beta_n\sigma_n t}$$

$$\times\frac{d\beta_n}{dt}\frac{d\sigma_n}{dt}\int_{t_n}^{t}(t^{'}-t_n)^2\left[1+c\beta_n\sigma_n(t^{'}-t_n)+O(\Delta t^2)\right]dt^{'}dt$$

where

$$t_n \le t^{**} \le t. \tag{2.53}$$

Simplifying Eq. (2.52), complete the integration of the error terms and use the mean value theorem to yield

$$\int_{t_n}^{t_{n+1}} S(t)dt = \int_{t_n}^{t_{n+1}} \sigma_n \int_{t_n}^{t} \beta_n\sigma_n\phi(t^{'}) \exp[-c\beta_n\sigma_n(t-t^{'})] + O(\Delta t^2)dt^{'}dt \tag{2.54}$$
$$+ \phi(t^*) \int_{t_n}^{t_{n+1}} \sigma_n\beta_n \frac{d\sigma_n}{dt} \left[1 - c\beta_n\sigma_n(t-t_n)\right] \frac{(t-t_n)^2}{2} dt$$
$$+ \phi(t^*) \int_{t_n}^{t_{n+1}} \sigma_n \frac{d\beta_n}{dt}\sigma_n \left[1 - c\beta_n\sigma_n(t-t_n)\right] \frac{(t-t_n)^2}{2} dt$$
$$+ \phi(t^*) \int_{t_n}^{t_{n+1}} \sigma_n \frac{d\beta_n}{dt}\frac{d\sigma_n}{dt} \left[1 - c\beta_n\sigma_n(t-t_n)\right] \frac{(t-t_n)^3}{3} dt$$
$$+ \phi(t^*) \exp\left[-c\beta_n\sigma_n(t^* - t^{**})\right] \int_{t_n}^{t_{n+1}} \frac{d\sigma_n}{dt}(t-t_n)\beta_n\sigma_n + O(\Delta t^3)dt$$
$$+ \phi(t^*) \int_{t_n}^{t_{n+1}} \frac{d\sigma_n}{dt}(t-t_n)\beta_n \frac{d\sigma_n}{dt} \left[1 - c\beta_n\sigma_n(t-t_n)\right] \frac{(t-t_n)^2}{2} dt$$
$$+ \phi(t^*) \int_{t_n}^{t_{n+1}} \frac{d\sigma_n}{dt}(t-t_n)\frac{d\beta_n}{dt}\sigma_n \left[1 - c\beta_n\sigma_n(t-t_n)\right] \frac{(t-t_n)^2}{2} dt$$
$$+ \phi(t^*) \int_{t_n}^{t_{n+1}} \frac{d\sigma_n}{dt}(t-t_n)\frac{d\beta_n}{dt}\frac{d\sigma_n}{dt} \left[1 - c\beta_n\sigma_n(t-t_n)\right] \frac{(t-t_n)^3}{3} dt$$

where

$$t_n \leq t^{**} \leq t^* \leq t_{n+1}, \tag{2.55}$$

finally yielding

$$\int_{t_n}^{t_{n+1}} S(t)dt = \int_{t_n}^{t_{n+1}} \sigma_n \int_{t_n}^{t} \beta_n\sigma_n\phi(t^{'}) e^{-F(t,t^{'})} dt^{'}dt + O(\Delta t^2). \tag{2.56}$$

Therefore, the $\int_{t_n}^{t_{n+1}} S(t)dt$ is $O(\Delta t^2)$ accurate locally.

Carter-Forest Material Temperature Update

Now, Eq. (2.27) with the Taylor expansion approximations to $\sigma(t)$ and $\beta(t)$ may be rewritten as

$$\phi(t_{n+1}) = \phi(t_n) - \int_{t_n}^{t_{n+1}} c\sigma_n\phi(t)dt + \int_{t_n}^{t_{n+1}} c^2\sigma_n U_r(t_n) e^{-c\beta_n\sigma_n(t-t_n)} dt \tag{2.57}$$
$$+ \int_{t_n}^{t_{n+1}} \sigma_n \int_{t_n}^{t} \beta_n\sigma_n\phi(t^{'}) \exp[-c\beta_n\sigma_n(t-t^{'})] dt^{'}dt + O(\Delta t^2).$$

It is worthwhile to note that the error in the Taylor expansion approximations was dominated by the approximation to $\sigma(t)$ but not $\beta(t)$. By examining each term in the CF equation and following the truncation error in time through temporal integration, the approximation to $\sigma(t)$ added $O(\Delta t^2)$ local error while the $\beta(t)$ term added $O(\Delta t^3)$ local error. The difference in the order of error that is added by each term is related to the number of times that the approximation is integrated. In the CF method, the truncation error for the $\beta(t)$ term is integrated at least two times while the approximations of $\sigma(t)$ are sometimes integrated only once. Assuming small values of Δt, each temporal integration diminishes the size of the error of the values from the Taylor expansion of each coefficient. Combining all of the terms, the approximation of $\phi(t_{n+1})$ is $O(\Delta t^2)$ locally and $O(\Delta t)$ globally.

To get the end of time step temperature, the conservation of energy equation is found by summing Eqs. (1.30) and (1.31),

$$\frac{1}{c}\frac{d\phi(t)}{dt} + \frac{dU_m(t)}{dt} = 0 \tag{2.58}$$

and then integrating over a time step to yield

$$U_m(t_{n+1}) = U_m(t_n) - \frac{1}{c}(\phi(t_{n+1}) - \phi(t_n)). \tag{2.59}$$

Knowing the start of time step values of $U_m(t_n)$ and $\phi(t_n)$, then using Eq. (2.57) for the value of $\phi(t_{n+1})$, the material energy density update becomes

$$U_m(t_{n+1}) = U_m(t_n) - \frac{1}{c}(\phi(t_{n+1}) - \phi(t_n)) + O(\Delta t^2). \tag{2.60}$$

The temperature is related to the material energy density U_m by

$$U_m(t) = \int_0^{T(t)} C_v(T(t))dT. \tag{2.61}$$

The approximation of $U_m(t)$ means the temperature at time t will be estimated with $O(\Delta t^2)$ local and $O(\Delta t)$ global accuracy. Therefore the error in the Carter-Forest method is $O(\Delta t^2)$ locally and $O(\Delta t)$ globally.

2.2.2 Implicit Monte Carlo (IMC) Truncation Error

Restating the 0D radiative transfer equations,

$$\frac{1}{c}\frac{d\phi(t)}{dt} + \sigma(t)\phi(t) = c\sigma(t)U_r(t) \tag{2.62}$$

$$\frac{1}{\beta(t)}\frac{dU_r(t)}{dt} + c\sigma(t)U_r(t) = \sigma(t)\phi(t) \tag{2.63}$$

the IMC method solves this set of equations in a significantly different way then the Carter-Forest method. Instead of solving the equation for $U_r(t)$ exactly, the IMC method makes two approximations. First, $U_r(t)$ is expressed as a combination of the emissivity at the beginning and end of the time step with a user defined parameter α which has the properties $0 \leq \alpha \leq 1$. $U_r(t)$ is approximated by first Taylor expanding around different time steps,

$$U_r(t) = U_r(t_n) + \frac{d}{dt}U_r(t_n)(t - t_n) + O(\Delta t^2) \tag{2.64}$$

$$U_r(t) = U_r(t_{n+1}) + \frac{d}{dt}U_r(t_{n+1})(t - t_{n+1}) + O(\Delta t^2) \tag{2.65}$$

then multiplying Eq. (2.64) by $(1-\alpha)$ and Eq. (2.65) by α. Adding the two modified equations together yields

$$\begin{aligned} U_r(t) = {} & \alpha U_r(t_{n+1}) + (1-\alpha)U_r(t_n) + (1-\alpha)\frac{d}{dt}U_r(t_n)(t - t_n) \\ & + \alpha\frac{d}{dt}U_r(t_{n+1})(t - t_{n+1}) + O(\Delta t^2). \end{aligned} \tag{2.66}$$

Substituting this estimate of $U_r(t)$ into Eq. (2.63), then integrating over a time step yields

$$\begin{aligned} \int_{t_n}^{t_{n+1}} \frac{dU_r(t)}{dt}dt = {} & \int_{t_n}^{t_{n+1}} \beta(t)\sigma(t)\phi(t)dt - \int_{t_n}^{t_{n+1}} c\beta(t)\sigma(t)\times \\ & \Big[\alpha U_r(t_{n+1}) + (1-\alpha)U_r(t_n) + (1-\alpha)\frac{d}{dt}U_r(t_n)(t - t_n) \\ & + \alpha\frac{d}{dt}U_r(t_{n+1})(t - t_{n+1})\Big]dt + O(\Delta t^3). \end{aligned} \tag{2.67}$$

Applying the Taylor expansion approximation to $\sigma(t)$ and $\beta(t)$ shown in Eqs. (2.28) and (2.29) to (2.67) and simplifying by removing higher than $O(\Delta t^2)$ errors

gives

$$
\begin{aligned}
U_r(t_{n+1}) - U_r(t_n) &= \int_{t_n}^{t_{n+1}} (\beta_n + \frac{d\beta_n}{dt}(t-t_n))(\sigma_n + \frac{d\sigma_n}{dt}(t-t_n))\phi(t)dt \qquad (2.68)\\
&- \int_{t_n}^{t_{n+1}} c(\beta_n + \frac{d\beta_n}{dt}(t-t_n))(\sigma_n + \frac{d\sigma_n}{dt}(t-t_n))\times \\
&\quad \Bigg[\alpha U_r(t_{n+1}) + (1-\alpha)U_r(t_n) + (1-\alpha)\frac{d}{dt}U_r(t_n)(t-t_n) \\
&\quad + \alpha\frac{d}{dt}U_r(t_{n+1})(t-t_{n+1})\Bigg]dt \\
&= \beta_n\sigma_n \int_{t_n}^{t_{n+1}} \phi(t)dt - c\beta_n\sigma_n\Delta t\Bigg[\alpha U_r(t_{n+1}) + (1-\alpha)U_r(t_n)\Bigg] \\
&+ \frac{1}{2}\Bigg[\sigma_n\frac{d\beta_n}{dt} + \beta_n\frac{d\sigma_n}{dt}\Bigg]\phi(t^*)\Delta t^2 \\
&+ \left[\frac{c\beta_n\sigma_n}{2}\right]((1-\alpha)\frac{d}{dt}U_r(t_n) - \alpha\frac{d}{dt}U_r(t_{n+1}))\Delta t^2 \\
&+ \frac{c}{2}(\sigma_n\frac{d\beta_n}{dt} + \beta\frac{d\sigma_n}{dt})\Bigg[\alpha U_r(t_{n+1}) + (1-\alpha)U_r(t_n)\Bigg]\Delta t^2
\end{aligned}
$$

where

$$t_n \le t^* \le t_{n+1}. \qquad (2.69)$$

Now solve for the value of $U_r(t_{n+1})$ neglecting detailed $O(\Delta t^2)$ terms

$$(1+\alpha\beta_n c\sigma_n\Delta t)U_r(t_{n+1}) = U_r(t_n) + \beta_n\sigma_n\int_{t_n}^{t_{n+1}}\phi(t)dt - \beta_n c\sigma_n\Delta t(1-\alpha)U_r(t_n) + O(\Delta t^2) \qquad (2.70)$$

which simplifies to the expression

$$U_r(t_{n+1}) = \frac{U_r(t_n) + (\alpha-1)\beta_n c\sigma_n\Delta t U_r(t_n)}{1+\alpha\beta_n c\sigma_n\Delta t} + \frac{\beta_n\sigma_n\int_{t_n}^{t_{n+1}}\phi(t)dt}{1+\alpha\beta_n c\sigma_n\Delta t} + O(\Delta t^2). \qquad (2.71)$$

Substituting Eq. (2.71) into Eq. (2.66), the $U_r(t_{n+1})$ term is now replaced in the IMC

approximation of the equilibrium radiation density as

$$U_r(t) = \frac{\alpha U_r(t_n) + \alpha(\alpha-1)\beta_n c\sigma_n \Delta t U_r(t_n)}{1+\alpha\beta_n c\sigma_n\Delta t} + \frac{\alpha\beta_n\sigma_n\int_{t_n}^{t_{n+1}}\phi(t)dt}{1+\alpha\beta_n c\sigma_n\Delta t} + (1-\alpha)U_r(t_n) \tag{2.72}$$

$$\begin{aligned}
&+ (1-\alpha)\frac{d}{dt}U_r(t_n)(t-t_n) + \alpha\frac{d}{dt}U_r(t_{n+1})(t-t_{n+1}) + O(\Delta t^2)\\
&= \frac{\alpha U_r(t_n) + \alpha^2\beta_n c\sigma_n\Delta t U_r(t_n) - \alpha\beta_n c\sigma_n\Delta t U_r(t_n)}{1+\alpha\beta_n c\sigma_n\Delta t}\\
&+ \frac{\alpha\beta_n\sigma_n\int_{t_n}^{t_{n+1}}\phi(t)dt}{1+\alpha\beta_n c\sigma_n\Delta t} + (1-\alpha)U_r(t_n)\frac{1+\alpha\beta_n c\sigma_n\Delta t}{1+\alpha\beta_n c\sigma_n\Delta t}\\
&+ (1-\alpha)\frac{d}{dt}U_r(t_n)(t-t_n) + \alpha\frac{d}{dt}U_r(t_{n+1})(t-t_{n+1}) + O(\Delta t^2)\\
&= \frac{U_r(t_n)}{1+\alpha\beta_n c\sigma_n\Delta t} + \frac{\alpha\beta_n\sigma_n\int_{t_n}^{t_{n+1}}\phi(t)dt}{1+\alpha\beta_n c\sigma_n\Delta t}\\
&+ (1-\alpha)\frac{d}{dt}U_r(t_n)(t-t_n) + \alpha\frac{d}{dt}U_r(t_{n+1})(t-t_{n+1}) + O(\Delta t^2).
\end{aligned}$$

The second IMC approximation is applied to $\phi(t)$ changing the time dependency as

$$\phi(t) \approx \phi(t^{'}) + \frac{d\phi(t^{'})}{dt}(t-t^{'}) + O(\Delta t^2) \tag{2.73}$$

or more pertantly stated as

$$\int_{t_n}^{t_{n+1}}\phi(t)dt \approx \phi(t^{'})\Delta t + O(\Delta t^2). \tag{2.74}$$

The approximation to $\phi(t)$ has the effect that all photons absorbed into the material will be emitted instantaneously instead of being held as in the CF equations. Applying the second IMC approximation from Eq. (2.73) to (2.72) yields

$$\begin{aligned}
U_r(t) = &\frac{U_r(t_n)}{1+\alpha\beta_n c\sigma_n\Delta t} + \frac{\alpha\beta_n\sigma_n\Delta t\phi(t^{'})}{1+\alpha\beta_n c\sigma_n\Delta t} + (1-\alpha)\frac{d}{dt}U_r(t_n)(t-t_n)\\
&+ \alpha\frac{d}{dt}U_r(t_{n+1})(t-t_{n+1}) + O(\Delta t^2).
\end{aligned} \tag{2.75}$$

Note that $O(\Delta t^2)$ error terms are dominated by $O(\Delta t)$ error terms,

$$(1-\alpha)\frac{d}{dt}U_r(t_n)(t-t_n) + \alpha\frac{d}{dt}U_r(t_{n+1})(t-t_{n+1}),$$

and therefore will be disregarded. Defining the Fleck Factor as

$$f = \frac{1}{1 + \alpha\beta_n c\sigma_n \Delta t} \tag{2.76}$$

equation (2.75) may be rewritten as

$$\begin{aligned} U_r(t) &= fU_r(t_n) + \frac{1-f}{c}\phi(t^{'}) + O(\Delta t) \\ &= fU_r(t_n) + \frac{1-f}{c}\phi(t) + O(\Delta t) \end{aligned} \tag{2.77}$$

where the dummy variable $t^{'}$ has been replaced by t. It is worthy to note that the $O(\Delta t)$ error in the expression for $U_r(t)$ is in fact caused by the IMC approximations and not the Taylor expansions of $\sigma(t)$ or $\beta(t)$.

Next, the equation for photon intensity is solved by substituting $U_r(t)$ with the approximation from equation (2.77) into (2.62) to yield

$$\frac{1}{c}\frac{d\phi(t)}{dt} + \sigma(t)\phi(t) = c\sigma(t)\left[fU_r(t_n) + \frac{1-f}{c}\phi(t) + O(\Delta t)\right]. \tag{2.78}$$

Like the equation for emissivity, $\sigma(t)$ is approximated by a Taylor expansion shown in equation (2.29)

$$\frac{1}{c}\frac{d\phi(t)}{dt} + (\sigma_n + \frac{d\sigma_n}{dt}(t-t_n))\phi(t) = c(\sigma_n + \frac{d\sigma_n}{dt}(t-t_n))\left[fU_r(t_n) + \frac{1-f}{c}\phi(t) + O(\Delta t)\right] \tag{2.79}$$

which is simplified to give the IMC estimated intensity equation

$$\frac{1}{c}\frac{d\phi(t)}{dt} + f\sigma_n\phi(t) = c\sigma_n f U_r(t_n) + \left[c\sigma_n - \frac{d\sigma_n}{dt}\phi(t) + \frac{d\sigma_n}{dt}cfU_r(t_n)\right]O(\Delta t). \tag{2.80}$$

Using an integrating factor to solve the differential IMC flux gives

$$\frac{d}{dt}[\phi(t)e^{c\sigma_n f t}] = c^2\sigma_n f U_r(t_n)e^{c\sigma_n f t} + O(\Delta t) \tag{2.81}$$

and integrating over the time step from t_n to t_{n+1}

$$\phi(t_{n+1})e^{c\sigma_n f t_{n+1}} - \phi(t_n)e^{c\sigma_n f t_n} = cU_r(t_n)\left[e^{c\sigma_n f t_{n+1}} - e^{c\sigma_n f t_n}\right] + O(\Delta t^2) \tag{2.82}$$

which is simplified to give the final solution

$$\phi(t_{n+1}) = \phi(t_n)e^{-c\sigma_n f\Delta t} + cU_r(t_n)(1 - e^{-c\sigma_n f\Delta t}) + O(\Delta t^2). \tag{2.83}$$

Therefore, the estimate of the flux is in fact $O(\Delta t^2)$ locally and $O(\Delta t)$ globally. This is the same order of error that the Carter-Forest method had for the same Taylor expanded values for both $\sigma(t)$ and $\beta(t)$. However, it should be noted that the dominating error in this expression comes from both the estimate of $\sigma(t)$ and the actual IMC approximations, meaning that while more approximations were made in the derivation of the Implicit Monte Carlo method, the order accuracy of the method is the same as the more exact Carter-Forest.

Implicit Monte Carlo Temperature Update

Just as before with the CF equations, the temperature is updated by using the conservation of energy

$$\frac{dU_m(t)}{dt} + \frac{1}{c}\frac{d\phi(t)}{dt} = 0. \tag{2.84}$$

Integrating over a time step and including the approximation to the flux $\phi(t)$

$$U_m(t_{n+1}) = U_m(t_n) - \frac{1}{c}(\phi(t_{n+1}) - \phi(t_n)) + O(\Delta t^2). \tag{2.85}$$

Using the relation between specific heat and temperature,

$$U_m(t) = \int_0^{T(t)} C_v(T(t))dT \tag{2.86}$$

the IMC estimates of the temperature after a time step are $O(\Delta t^2)$ locally and $O(\Delta t)$ globally.

The order accuracy of the IMC and CF methods are exactly the same. However, the increased use of exponentials in the CF method makes it computationally more intensive than the traditional IMC method. Therefore, it appears the higher fidelity of the Carter-Forest method is not a clear improvement on the Implicit Monte Carlo method. It is worth noting that the IMC method has two sources of $O(\Delta t)$ global error coming from the approximation of the equilibrium radiation density and the estimation of $\sigma(t)$ while the CF method has only one, due to the $\sigma(t)$ approximation. Therefore predictor-corrector methods are examined to determine if the error associated with the time truncation of $\sigma(t)$ can be reduced and yield a more accurate solution.

2.3 Predictor-Corrector Truncation Error for the Carter-Forest and Implicit Monte Carlo Solutions

Since both the CF and IMC methods have a leading order error term caused by the truncation of $\sigma(t)$, a predictor-corrector is applied to better resolve the nonlinearity in $\sigma(t)$. If the predictor-corrector removes the leading order error, the CF method will become $O(\Delta t^2)$ globally accurate in the zero dimensional, nonlinear problem. However, since there are two dominant sources of error for the IMC method, a predictor-corrector alone will not be able to change the order error of the method.

2.3.1 Carter-Forest Predictor-Corrector Truncation Error

To reduce the truncation error caused by the approximation to $\sigma(t)$, the midpoint method is used. First, $\sigma(t)$ will be expanded as

$$\sigma(t) = \sigma(t_{n+\frac{1}{2}}) + \frac{d\sigma(t_{n+\frac{1}{2}})}{dt}(t - t_{n+\frac{1}{2}}) + \frac{1}{2}\frac{d^2\sigma(t_{n+\frac{1}{2}})}{dt^2}(t - t_{n+\frac{1}{2}})^2 + O(\Delta t^3). \quad (2.87)$$

Therefore, estimates of $\sigma(t_{n+1})$ and $\sigma(t_n)$ may be expressed as

$$\sigma(t_{n+1}) = \sigma(t_{n+\frac{1}{2}}) + \frac{d\sigma(t_{n+\frac{1}{2}})}{dt}(t - t_{n+\frac{1}{2}}) + \frac{1}{2}\frac{d^2\sigma(t_{n+\frac{1}{2}})}{dt^2}(t - t_{n+\frac{1}{2}}) \quad (2.88)$$

and

$$\sigma(t_n) = \sigma(t_{n+\frac{1}{2}}) - \frac{d\sigma(t_{n+\frac{1}{2}})}{dt}(t - t_{n+\frac{1}{2}}) + \frac{1}{2}\frac{d^2\sigma(t_{n+\frac{1}{2}})}{dt^2}(t - t_{n+\frac{1}{2}}). \quad (2.89)$$

Adding equations (2.88) and (2.89) yields

$$\sigma(t_{n+1}) + \sigma(t_n) = 2\sigma(t_{n+\frac{1}{2}}) + \frac{d^2\sigma(t_{n+\frac{1}{2}})}{dt^2}(t - t_{n+\frac{1}{2}}) \quad (2.90)$$

which can be rearranged to show

$$\sigma(t_{n+\frac{1}{2}}) = \frac{\sigma(t_{n+1}) + \sigma(t_n)}{2} + O(\Delta t^2). \quad (2.91)$$

The value of $\sigma(t_{n+1})$ must be estimated with an accuracy that is at least $O(\Delta t^2)$ for the midpoint method to work. To that end, a predictor step is used to get an estimate

of the temperature at the time t_{n+1} which is $O(\Delta t^2)$ accurate since only one step is being taken. Next, the opacity is evaluated at the predicted temperature to yield an $O(\Delta t^2)$ estimate of $\sigma(t_{n+1})$ defined as $\tilde{\sigma}(t_{n+1})$. Equation (2.91) can be restated with the estimated value $\tilde{\sigma}(t_{n+1})$ as

$$\begin{aligned}\sigma(t_{n+\frac{1}{2}}) &= \frac{[\tilde{\sigma}(t_{n+\frac{1}{2}}) + O(\Delta t^2)] + \sigma(t_n)}{2} + O(\Delta t^2) \\ &= \frac{\tilde{\sigma}(t_{n+\frac{1}{2}}) + \sigma(t_n)}{2} + O(\Delta t^2).\end{aligned} \tag{2.92}$$

After calculating the end of time step temperature (and therefore opacity), a corrector step is used to run the same time step again with the updated values for the opacity. Using the predictor-corrector equation (2.92) in (2.27), the truncation error is examined in all terms that contain the new approximation to $\sigma(t)$ but still use the old approximation to $\beta(t)$. The $\sigma(t_{n+\frac{1}{2}})$ term will be written as $\sigma_{n+\frac{1}{2}}$ for simplicity.

The $\int_{t_n}^{t_{n+1}}[\sigma_{n+\frac{1}{2}} + O(\Delta t^2)]\phi(t)dt$ Term

Simplifying this term will yield

$$\begin{aligned}\int_{t_n}^{t_{n+1}}[\sigma_{n+\frac{1}{2}} + O(\Delta t^2)]\phi(t)dt &= \int_{t_n}^{t_{n+1}}\sigma_{n+\frac{1}{2}}\phi(t)dt + \int_{t_n}^{t_{n+1}}\phi(t)O(\Delta t^2)dt \\ &= \int_{t_n}^{t_{n+1}}\sigma_{n+\frac{1}{2}}\phi(t)dt + O(\Delta t^3)\end{aligned} \tag{2.93}$$

The $\int_{t_n}^{t_{n+1}} R(t)dt$ Term

The expression of $R(t)$ is still fairly complicated and will be evaluated in parts. First, the exponential will be Taylor expanded such that,

$$\begin{aligned}e^{-F^*(t)} &= \exp\left[\int_{t_n}^{t} -c[\beta_n + \frac{d\beta_n}{dt}(t'' - t_n)][\sigma_{n+\frac{1}{2}} + O(\Delta t^2)]dt''\right] \\ &= \exp\left[-c\beta_n\sigma_{n+\frac{1}{2}}(t - t_n) - \frac{1}{2}\frac{d\beta_n}{dt}\sigma_{n+\frac{1}{2}}(t - t_n)^2 + O(\Delta t^3)\right] \\ &= \exp\left[-c\beta_n\sigma_{n+\frac{1}{2}}(t - t_n)\right]\exp\left[-\frac{1}{2}(\frac{d\beta_n}{dt}\sigma_{n+\frac{1}{2}})(t - t_n)^2 + O(\Delta t^3)\right]\end{aligned} \tag{2.94}$$

As shown previously, the Taylor expansion of the error will yield

$$e^{-F^*(t)} \approx \exp\left[- c\beta_n \sigma_{n+\frac{1}{2}}(t - t_n)\right] + O(\Delta t^2). \tag{2.95}$$

Neglecting higher order errors,the integration of $R(t)$ can now be examined as

$$\begin{aligned}\int_{t_n}^{t_{n+1}} R(t)dt &= \int_{t_n}^{t_{n+1}} c[\sigma_{n+\frac{1}{2}} + O(\Delta t^2)]U_r(t_n)e^{-F^*(t)}dt \\ &= \int_{t_n}^{t_{n+1}} c\sigma_{n+\frac{1}{2}}U_r(t_n)\exp^{-c\beta_n\sigma_{n+\frac{1}{2}}(t-t_n)} + O(\Delta t^2)dt \\ &= \int_{t_n}^{t_{n+1}} c\sigma_{n+\frac{1}{2}}U_r(t_n)\exp^{-c\beta_n\sigma_{n+\frac{1}{2}}(t-t_n)}\, dt + O(\Delta t^3).\end{aligned} \tag{2.96}$$

The $\int_{t_n}^{t_{n+1}} S(t)dt$ Term

As shown previously in Eq. (2.46), the expansion of $e^{-F^*(t,t^{'})}$ is

$$\begin{aligned}e^{-F^*(t,t^{'})} &\approx \exp\left[-\int_{t^{'}}^{t} c[\beta_n + \frac{d\beta_n}{dt}(t^{''} - t_n)][\sigma_{n+\frac{1}{2}} + O(\Delta t^2)]dt^{''}\right] \\ &\approx \exp\left[-c\beta_n\sigma_{n+\frac{1}{2}}(t - t^{'})\right] + O(\Delta t^2).\end{aligned} \tag{2.97}$$

Now, the expression for $\int_{t_n}^{t_{n+1}} S(t)dt$ is rewritten with the error approximation for the exponential already included

$$\int_{t_n}^{t_{n+1}} S(t)dt = \tag{2.98}$$
$$\int_{t_n}^{t_{n+1}} \sigma_{n+\frac{1}{2}} \int_{t_n}^{t} \beta_n \sigma_{n+\frac{1}{2}} \phi(t^{'}) [\exp\left[- c\beta_n \sigma_{n+\frac{1}{2}} (t - t^{'}) \right] + O(\Delta t^2)] dt^{'} dt$$
$$+ \int_{t_n}^{t_{n+1}} \sigma_{n+\frac{1}{2}} \int_{t_n}^{t} \beta_n O(\Delta t^2) \phi(t^{'}) [\exp\left[-c\beta_n \sigma_{n+\frac{1}{2}} (t - t^{'}) \right] + O(\Delta t^2)] dt^{'} dt$$
$$+ \int_{t_n}^{t_{n+1}} \sigma_{n+\frac{1}{2}} \int_{t_n}^{t} \frac{d\beta_n}{dt} (t^{'} - t_n) \sigma_{n+\frac{1}{2}} \phi(t^{'}) [\exp\left[-c\beta_n \sigma_{n+\frac{1}{2}} (t - t^{'}) \right] + O(\Delta t^2)] dt^{'} dt$$
$$+ \int_{t_n}^{t_{n+1}} \sigma_{n+\frac{1}{2}} \int_{t_n}^{t} \frac{d\beta_n}{dt} (t^{'} - t_n) O(\Delta t^2) \phi(t^{'}) [\exp\left[-c\beta_n \sigma_{n+\frac{1}{2}} (t - t^{'}) \right] + O(\Delta t^2)] dt^{'} dt$$
$$+ \int_{t_n}^{t_{n+1}} O(\Delta t^2) \int_{t_n}^{t} \beta_n \sigma_{n+\frac{1}{2}} \phi(t^{'}) [\exp\left[-c\beta_n \sigma_{n+\frac{1}{2}} (t - t^{'}) \right] + O(\Delta t^2)] dt^{'} dt$$
$$+ \int_{t_n}^{t_{n+1}} O(\Delta t^2) \int_{t_n}^{t} \beta_n O(\Delta t^2) \phi(t^{'}) [\exp\left[-c\beta_n \sigma_{n+\frac{1}{2}} (t - t^{'}) \right] + O(\Delta t^2)] dt^{'} dt$$
$$+ \int_{t_n}^{t_{n+1}} O(\Delta t^2) \int_{t_n}^{t} \frac{d\beta_n}{dt} (t^{'} - t_n) \sigma_{n+\frac{1}{2}} \phi(t^{'}) [\exp\left[-c\beta_n \sigma_{n+\frac{1}{2}} (t - t^{'}) \right] + O(\Delta t^2)] dt^{'} dt$$
$$+ \int_{t_n}^{t_{n+1}} O(\Delta t^2) \int_{t_n}^{t} \frac{d\beta_n}{dt} (t^{'} - t_n) O(\Delta t^2) \phi(t^{'}) [\exp\left[-c\beta_n \sigma_{n+\frac{1}{2}} (t - t^{'}) \right] + O(\Delta t^2)] dt^{'} dt.$$

Following the same steps before in applying the mean value theorem of integration, the error again is dominated by one of the expanded terms such that

$$\int_{t_n}^{t_{n+1}} S(t)dt = \int_{t_n}^{t_{n+1}} \sigma_{n+\frac{1}{2}} \int_{t_n}^{t} \beta_n \sigma_{n+\frac{1}{2}} \phi(t^{'}) \exp\left[-c\beta \sigma_{n+\frac{1}{2}} (t - t^{'}) \right] dt^{'} dt + O(\Delta t^3). \tag{2.99}$$

Carter-Forest Predictor-Corrector Temperature Update

Now, Eq. (2.27) with the Taylor expansion predictor-corrector approximations to $\sigma(t)$ and $\beta(t)$ may be rewritten as

$$\phi(t_{n+1}) = \phi(t_n) + \int_{t_n}^{t_{n+1}} c\sigma_{n+\frac{1}{2}}\phi(t)dt + \int_{t_n}^{t_{n+1}} c^2\sigma_{n+\frac{1}{2}}U_r(t_n)\exp^{-c\beta_n\sigma_{n+\frac{1}{2}}(t-t_n)}dt \tag{2.100}$$
$$+ \int_{t_n}^{t_{n+1}} \sigma_{n+\frac{1}{2}} \int_{t_n}^{t} \beta_n\sigma_{n+\frac{1}{2}}\phi(t^{'})e^{-F^*(t,t^{'})}dt^{'}dt + O(\Delta t^3).$$

The most significant difference between equations (2.57) and (2.100) is the order of their approximation. For the predictor-corrector method, the order error is $O(\Delta t^3)$ locally and $O(\Delta t^2)$ globally when used to solve the energy balance equation to calculate the end of time step temperature, while the traditional approach is $O(\Delta t^2)$ locally and $O(\Delta t)$ globally. It appears that the predictor-corrector method can be an improvement over the traditional Carter-Forest method implementation even though twice the amount of work must be done to get the next temperature estimate. The higher order error after the predictor-corrector approach will allow an over-all faster convergence to the correct solution.

2.3.2 Implicit Monte Carlo Predictor-Corrector Truncation Error

As with the Carter-Forest method, the IMC method has an $O(\Delta t^2)$ error in estimating of the temperature for one time step and therefore can be used in the midpoint method predictor-corrector. Restating equation (2.67), the IMC approximation to $U_r(t)$ before the Taylor expansion of the $\sigma(t)$ and $\beta(t)$ terms is

$$\int_{t_n}^{t_{n+1}} \frac{dU_r(t)}{dt}dt = \int_{t_n}^{t_{n+1}} \beta(t)\sigma(t)\phi(t)dt - \int_{t_n}^{t_{n+1}} c\beta(t)\sigma(t)\times \tag{2.101}$$
$$\Big[\alpha U_r(t_{n+1}) + (1-\alpha)U_r(t_n) + (1-\alpha)\frac{d}{dt}U_r(t_n)(t-t_n)$$
$$+ \alpha\frac{d}{dt}U_r(t_{n+1})(t-t_{n+1})\Big]dt.$$

Applying the predictor-corrector estimate for $\sigma(t)$ given in Eqs. (2.67) to (2.91) yields

$$
\begin{aligned}
U_r(t_{n+1}) - U_r(t_n) &= \int_{t_n}^{t_{n+1}} (\beta_n + \frac{d\beta_n}{dt}(t-t_n))(\sigma_{n+\frac{1}{2}} + O(\Delta t^2))\phi(t)dt \qquad (2.102)\\
&- \int_{t_n}^{t_{n+1}} c(\beta_n + \frac{d\beta_n}{dt}(t-t_n))(\sigma_{n+\frac{1}{2}} + O(\Delta t^2))\times \\
&\quad \Bigg[\alpha U_r(t_{n+1}) + (1-\alpha)U_r(t_n) + (1-\alpha)\frac{d}{dt}U_r(t_n)(t-t_n) \\
&\quad + \alpha\frac{d}{dt}U_r(t_{n+1})(t-t_{n+1})\Bigg]dt \\
&= \beta_n\sigma_{n+\frac{1}{2}}\int_{t_n}^{t_{n+1}}\phi(t)dt - c\beta_n\sigma_{n+\frac{1}{2}}\Delta t\Bigg[\alpha U_r(t_{n+1}) + (1-\alpha)U_r(t_n)\Bigg] \\
&+ \frac{1}{2}\Bigg[\sigma_{n+\frac{1}{2}}\frac{d\beta_n}{dt}\Bigg]\phi(t^*)\Delta t^2 \\
&+ \Bigg[\frac{c\beta_n\sigma_{n+\frac{1}{2}}}{2}\Bigg]((1-\alpha)\frac{d}{dt}U_r(t_n) - \alpha\frac{d}{dt}U_r(t_{n+1}))\Delta t^2 \\
&+ \frac{c}{2}(\sigma_n\frac{d\beta_n}{dt})\Bigg[\alpha U_r(t_{n+1}) + (1-\alpha)U_r(t_n)\Bigg]\Delta t^2.
\end{aligned}
$$

Solving for $U_r(t_{n+1})$ yields a similar result to (2.71),

$$
U_r(t_{n+1}) \approx \frac{U_r(t_n) + (\alpha-1)\beta_n c\sigma_{n+\frac{1}{2}}\Delta t U_r(t_n)}{1+\alpha\beta_n c\sigma_{n+\frac{1}{2}}\Delta t} + \frac{\beta_n\sigma_{n+\frac{1}{2}}\int_{t_n}^{t_{n+1}}\phi(t)dt}{1+\alpha\beta_n c\sigma_{n+\frac{1}{2}}\Delta t} + O(\Delta t^2). \qquad (2.103)
$$

Next, the second IMC approximation is applied to (2.103). Simplifying this yields

$$
U_r(t) = f_{n+\frac{1}{2}}U_r(t_n) + \frac{1-f_{n+\frac{1}{2}}}{c}\phi(t) + O(\Delta t) \qquad (2.104)
$$

where

$$
f_{n+\frac{1}{2}} = \frac{1}{1+\alpha\beta_n c\sigma_{n+\frac{1}{2}}\Delta t}. \qquad (2.105)
$$

It appears at this stage that the IMC approximations themselves are unaffected by this particular predictor-corrector method. Next, Eq. (2.104) is substituted into the predictor-corrector modified photon intensity Eq. (2.106)

$$
\frac{1}{c}\frac{d\phi(t)}{dt} + (\sigma_{n+\frac{1}{2}} + O(\Delta t^2))\phi(t) = c(\sigma_{n+\frac{1}{2}} + O(\Delta t^2))\Bigg[f_{n+\frac{1}{2}}U_r(t_n) + \frac{1-f_{n+\frac{1}{2}}}{c}\phi(t) + O(\Delta t)\Bigg] \qquad (2.106)
$$

which is simplified to give the IMC estimated intensity equation

$$\frac{1}{c}\frac{d\phi(t)}{dt} + f_{n+\frac{1}{2}}\sigma_{n+\frac{1}{2}}\phi(t) = c\sigma_{n+\frac{1}{2}}f_{n+\frac{1}{2}}U_r(t_n) + \left[c\sigma_{n+\frac{1}{2}}\right]O(\Delta t). \tag{2.107}$$

Using an integrating factor and then integrating over a time step, (2.107) can be rewritten as

$$\phi(t_{n+1}) = \phi(t_n)e^{-c\sigma_{n+\frac{1}{2}}f_{n+\frac{1}{2}}\Delta t} + cU_r(t_n)(1 - e^{-c\sigma_{n+\frac{1}{2}}f_{n+\frac{1}{2}}\Delta t}) + O(\Delta t^2). \tag{2.108}$$

The truncation error for the IMC predictor-corrector method is $O(\Delta t^2)$ locally and $O(\Delta t)$ globally. Unfortunately, this is not an improvement over the traditional implementation of the IMC equations. The lack of improvement occurs because of the IMC approximation shown in Eq. (2.66) that is made in addition to the time truncation to $\sigma(t)$. However, it is still possible to achieve $O(\Delta t^2)$ global convergence with the IMC method in the 0D equations using a predictor-corrector if the value of $\alpha = 0.5$. However, for stability reasons α is almost always set equal to 1. The reason that $\alpha = 0.5$ is different than other values of α in terms of accuracy in the IMC equations was determined by the previous residual error analysis.

Chapter 3

Zero Dimensional Numerical Results

For the TRT (Thermal Radiative Transfer) equations, the 0D test bed allows for the testing of the fundamental mechanics of photon transport with energy deposition and the coupled material emissions in computationally easy manner. The linear zero dimensional Gray Thermal Radiation Transport (GTRT) equations can be solved exactly during a time step by the CF method. By comparing the results of the CF and IMC methods in this problem, the IMC bias can be examined graphically.

Additional approximations must be made to solve the nonlinear zero dimensional GTRT problems since both β and σ are functions of temperature. In this nonlinear problem, the CF solution is no longer exact. However, a very good estimate of the true solution can be made by using a highly refined time step size. The result of the refined solution is then used as the benchmark to test the predicted accuracy of the predictor-corrector methods.

3.1 Bias in the Implicit Monte Carlo Method

Equation (2.19) demonstrates mathematically that there is a bias in the GTRT linear analytic solution of the IMC equation. Depending on whether the problem is warming or cooling, the material temperature will be cooler or warmer than the correct solution respectively. To confirm the mathematical result, a numerical simulation is performed here. A linear radiative 0D radiative transfer problem is solved with the radiation constant $a = 1$, the speed of light $c = 1$, $\beta(t) = 1$, $\sigma(t) = 1$, using a time step size of $\Delta t = 0.1$ and a starting temperature of $T = 0.1$. Figure 3.1 shows the difference between the IMC and CF method. The IMC method with $\alpha = 1$ clearly has a lower transient temperature for the material than the CF method even though both methods

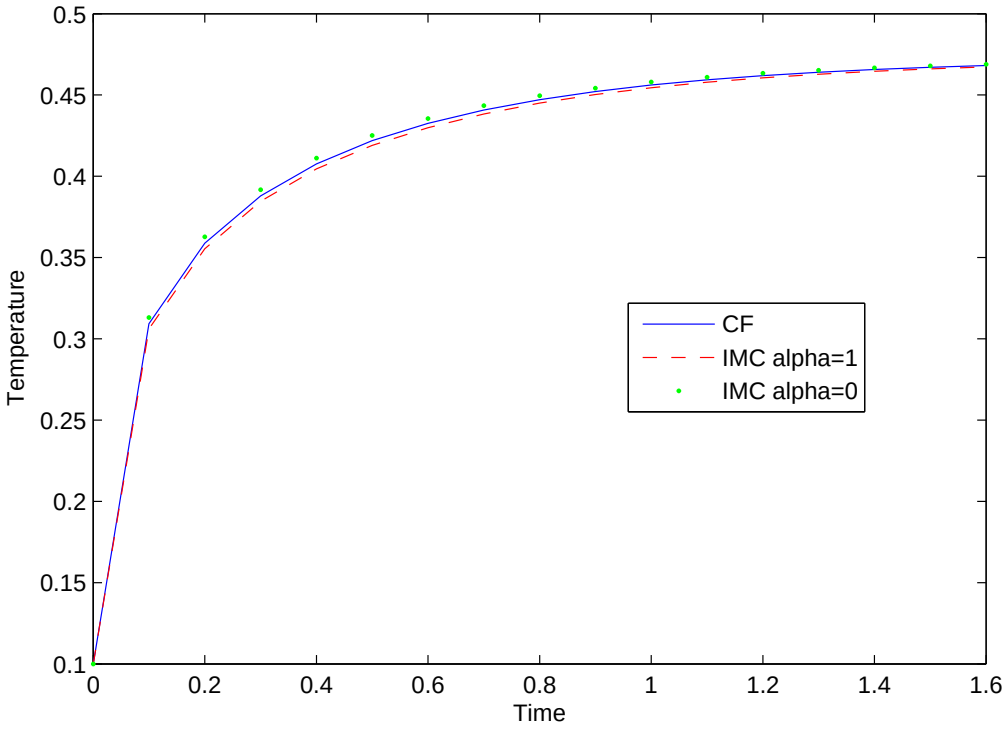

Figure 3.1: Temperature vs. time for IMC and CF.

eventually reach the same equilibrium material temperature. Similarly, when $\alpha = 0$, the IMC method has a warmer temperature than the CF method during the transient. In this particular problem, the CF method is exact, exposing the residual error that comes from the IMC approximations described previously. As the size of the time step is decreased, the IMC bias is reduced and the computed solution during the transient becomes closer to the exact CF solution.

While the linear radiative transfer solutions are interesting, they are still unphysical. To determine the effects of the bias in the IMC method with more realistic problems, a warming and cooling problem are defined to explore the analytical results shown in Eqs. (2.19) and (2.21) Both the warming and cooling problems set $a = 1$, $c = 1$, have the nonlinear values of $\sigma(T) = 1000/T^3$ and a constant heat capacity C_v such that $\beta(T) = 40T^3$. The warming problem has a burst of photons with an intensity $\phi(0) = 1000cU_r(0)$ at the start of the problem with an initial temperature of $T = 0.1$. No new energy is added to the problem after this point. The cooling down problem starts with a temperature $T = 1.0$ and has a cooler radiation field starting at $\phi(0) = cU_r(0)/16$. Therefore, the warming problem starts with a higher radiation temperature which eventually will cause the material to warm and the cooling problem

has a colder radiation temperature which will cause less absorptions in the material causing it to cool. The material temperature of the infinite medium problem vs. time can be seen in Figs. 3.2a and 3.2b.

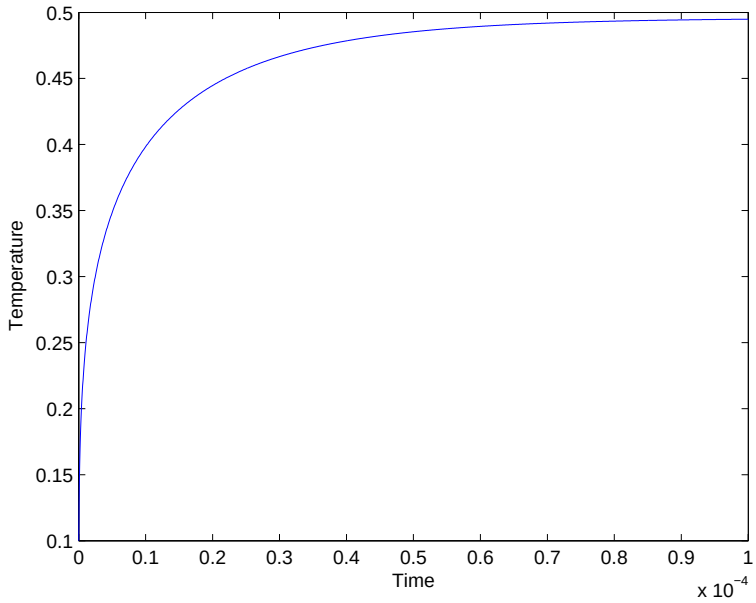

(a) Warming Problem

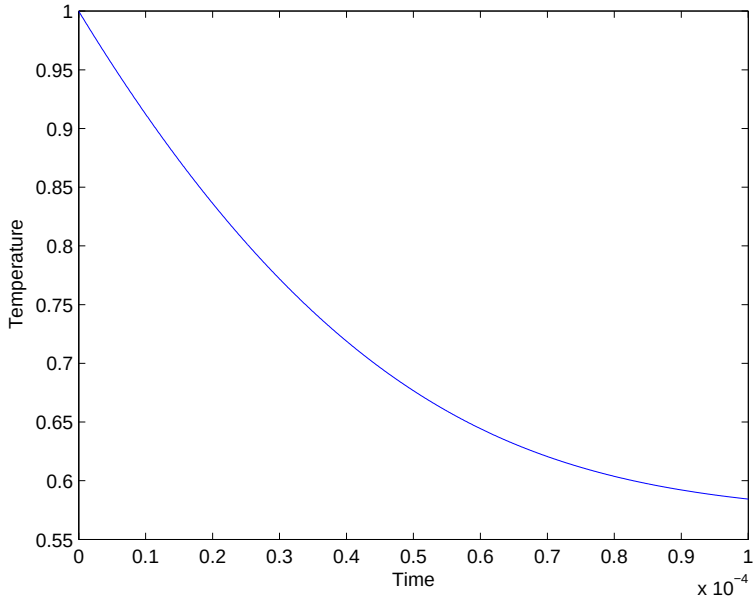

(b) Cooling Problem

Figure 3.2: Material temperature at different times for the warming and cooling problems.

To determine the error in the estimate of the temperature of both the CF method

and the IMC method, a finely resolved time step solution of $\Delta t = 10^{-13}$ is created using the CF method. Next, the instantaneous relative error defined as

$$R_e(t) = \frac{\mid T_r(t) - T_c(t) \mid}{T_r(t)} \tag{3.1}$$

where $T_r(t)$ represents the reference solution at time t and $T_c(t)$ represents the calculated solution. The relative error will be examined in both the heating and cooling problems at the times $t = 0.1 \times 10^{-4}$, $t = 0.5 \times 10^{-4}$, and $t = 1.0 \times 10^{-4}$ as a function of time step Δt.

The IMC method will be compared in both the heating and cooling problem to the CF method. Furthermore, the same problems will be run 3 times with different values of α to show the bias in the IMC solutions vs. the CF solutions predicted by the residual error analysis. In Figs. 3.3a and 3.3b the CF method is shown as lines and the IMC method is shown as symbols at three different time periods. In the warming problem with $\alpha = 1$, it appears that the IMC solution yields a more accurate solution than the CF method for smaller time step sizes later in the problem time. For the cooling problem, it is the CF method that is more accurate than IMC with $\alpha = 1$.

To understand the differences between the accuracy of the two methods, it is important to examine the change in the opacities during these transients. Plotting the first 20 points of both the warming and cooling problems in Figs. 3.4a and 3.4b it can be seen that the two problems have very different changes in opacity in the early transient.

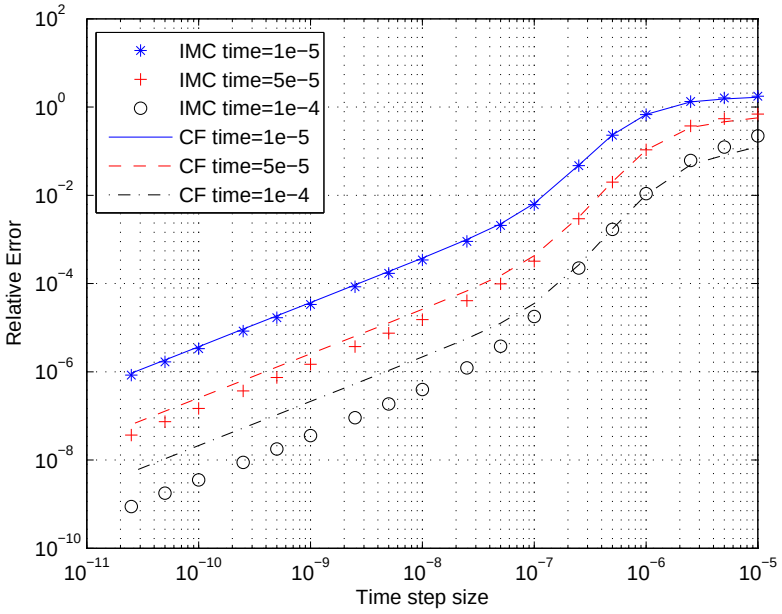

(a) Warming Problem

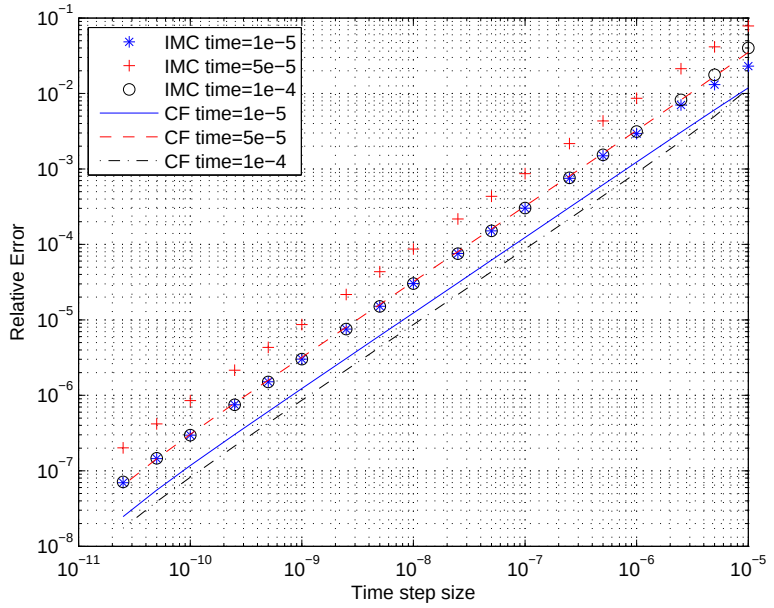

(b) Cooling Problem

Figure 3.3: Relative error at different times with $\alpha = 1$.

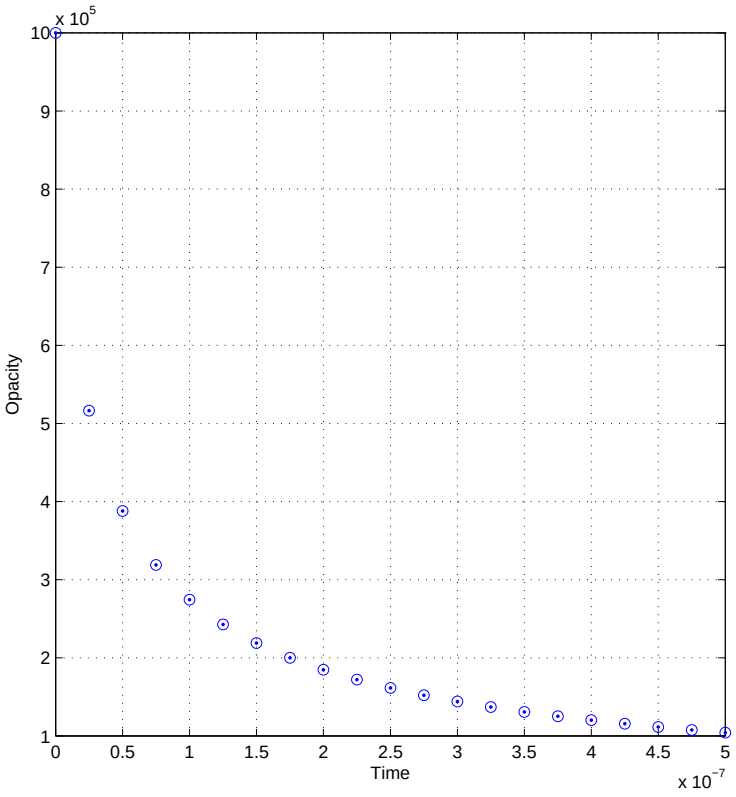

(a) Warming Problem

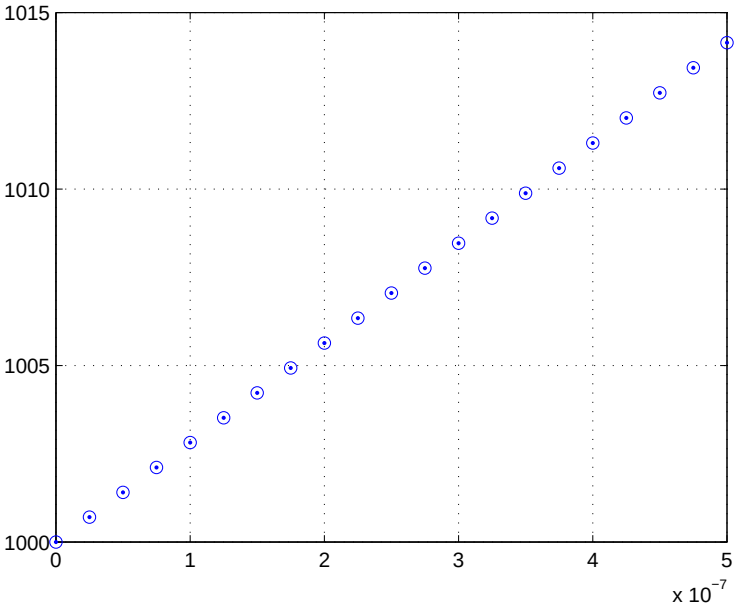

(b) Cooling Problem

Figure 3.4: Value of the opacity at different times with $\alpha = 1$.

For the warming problem, the opacities get halved between the first time step and the second. This implies that the GTRT is modeling radiation transport with a very poor estimate of the opacity during the first couple of time steps. Eventually, the opacities do not change as significantly from time step to time step, making the approximation of $\sigma(t_n)$ a better estimate than it was early on in the transient. By keeping the material overly opaque for an extended period of time there will be more absorptions than should have physically occurred during the time step. It is here that the IMC bias actually helps the approximation of the solution. Because of the higher number of absorptions, the material temperature becomes larger than it should be. This error in the temperature, caused by a poor approximation of $\sigma(t)$, is offset by the IMC bias. Since the IMC method in a warming problem causes the material temperature to be cooler than it should be, it gives a solution that is closer to the true transient than the CF method at the same larger time step size.

For the cooling down problem, the opacities are changing relative slowly compared to the warming problem, meaning the constant opacity approximation is more appropriate but still inaccurate since the number of particles emitted from the material is based on the value of σ. However, the IMC method in the cooling down problem will keep more energy in the material than should be there, keeping it artificially warm. This will keep the value of the opacity smaller than it should be, thus limiting the material emissions during a time step. As shown in the truncation analysis, when $\alpha = 0.5$ the IMC approximation error no longer dominates the temporal convergence. Rather, in this case, it is the estimation of the opacities that dominates. Figures 3.5a and 3.5b demonstrate that the IMC and CF method are effectively the same during the transients when $\alpha = 0.5$, as predicted by Eq. (2.16).

Finally, setting $\alpha = 0$, which is never done in practice, the effect of the bias in the IMC solutions is opposite of what occurs when setting $\alpha = 1$. Equation (2.21) predicts that the IMC solutions will keep too little energy in the radiation field and keep more in the material temperature. Figure 3.6a now shows the IMC method to be a worse approximation than the CF method in the warming problem because the bias makes the material temperature higher on top of extra energy added to the material due to poor opacity estimates. Figure 3.6b shows the IMC method to be a better than the CF method in the cooling problem (give better explanation). Though these numerical results have shown the range $0 \leq \alpha \leq 1$, for stability reasons the suggested range of α is (5) $0.5 \leq \alpha \leq 1$ but the most common practice is to simply set $\alpha = 1$.

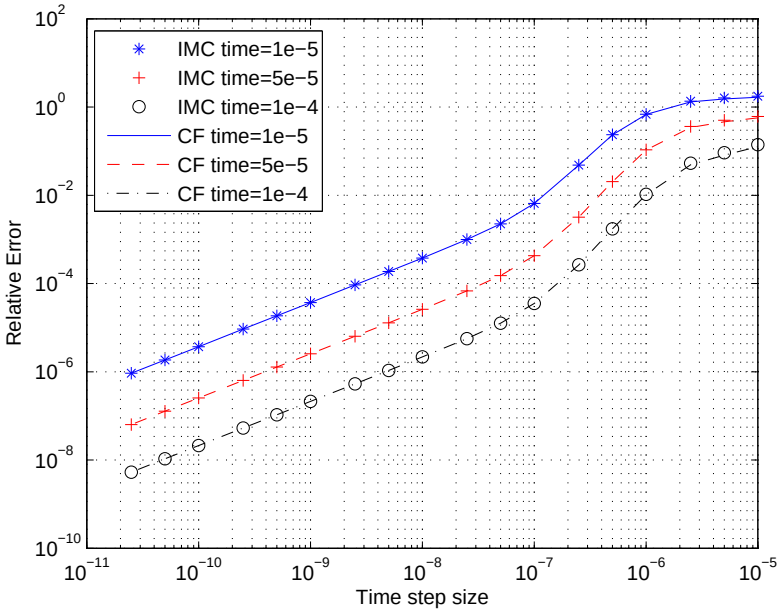

(a) Warming Problem

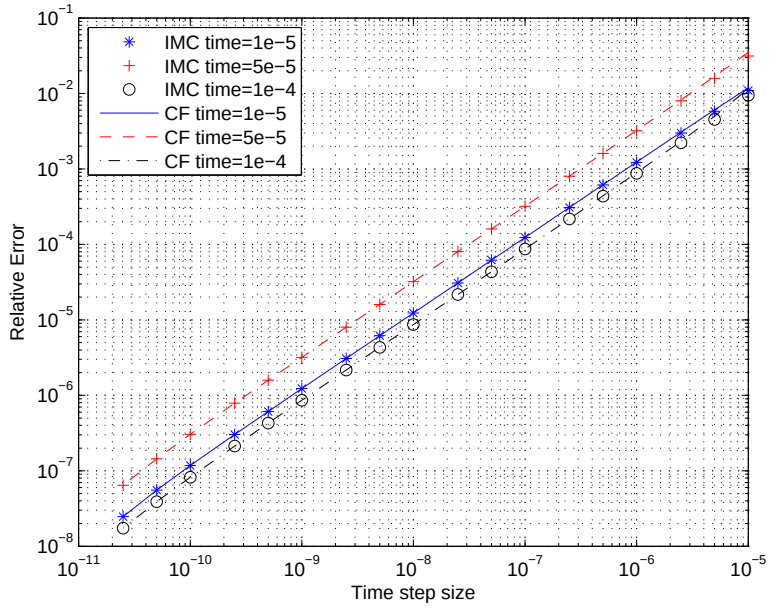

(b) Cooling Problem

Figure 3.5: Relative error at different times with $\alpha = 0.5$.

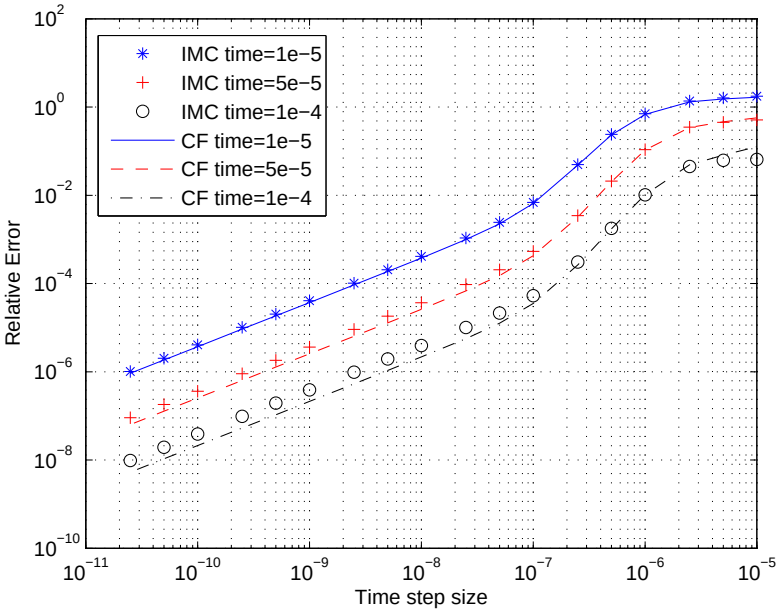

(a) Warming Problem

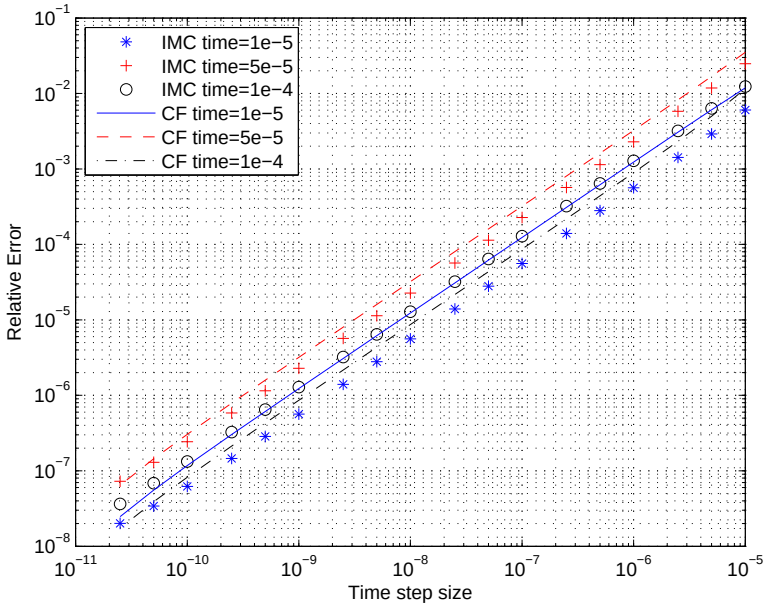

(b) Cooling Problem

Figure 3.6: Relative error at different times with $\alpha = 0$.

3.2 Predictor-Corrector Methods

Both the IMC method and the CF method approximate the values of both $\beta(t)$ and $\sigma(t)$ as constant during a time step to linearize a nonlinear problem. These approximations make the CF method inexact, and introduce an $O(\Delta t)$ global error into both the IMC and CF methods. Although two approximations are made in the linearization of the problem, it is the approximation to $\sigma(t)$ that introduces the $O(\Delta t)$ global error while the approximations to $\beta(t)$ are $O(\Delta t^2)$. A better prediction of the value of σ during a time step should allow for a more accurate solution. By running a simulation twice per time step, once to predict the end of time step temperature (or opacity) and once to correct that temperature (or opacity), a more accurate solution can be produced.

The Opacity Averaged Predictor-Corrector (OAPC) averages the beginning and end of time step opacities to achieve a higher order approximation as shown in equation (2.91). Using the OAPC, the relative error in temperature for the warming problem changes significantly. Figure 3.7 shows that the CF method becomes an $O(\Delta t^2)$

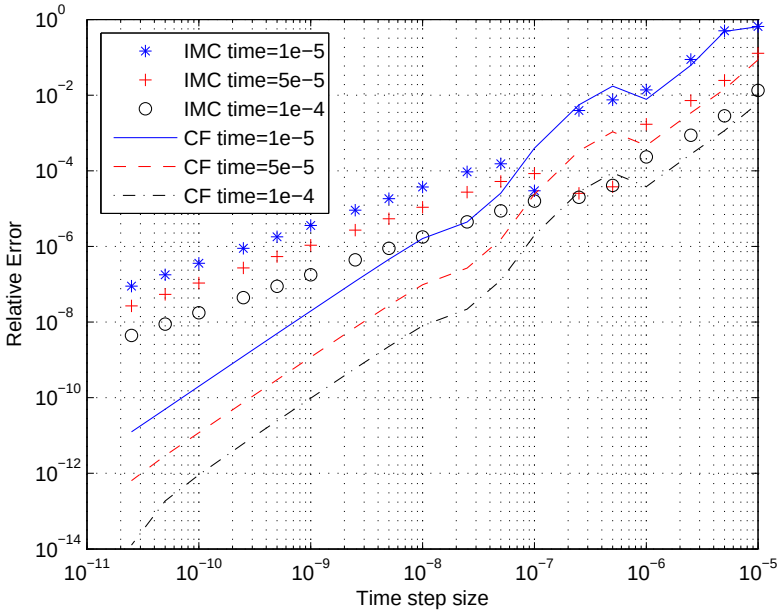

Figure 3.7: Relative error vs. time step size for Opacity Averaged Predictor-Corrector.

method while the IMC method remains an $O(\Delta t)$ global method. This is an expected result since it is the estimation of $\sigma(t)$ that is the main source of error in the CF method but only one source of $O(\Delta t)$ global error in the IMC method. While there is structure in the graph, it is worth while to consider that the linear averaging of the

opacity that is an inversely cubed function,

$$\sigma(t_{n+\frac{1}{2}}) = \frac{\tilde{\sigma}(t_{n+1}) + \sigma(t_n)}{2} + O(\Delta t^2) \tag{3.2}$$

$$= \frac{\frac{\gamma}{T_{n+1}^3} + \frac{\gamma}{T_n^3}}{2} + O(\Delta t^2) \tag{3.3}$$

where γ is material specific, is not expected to be a good estimation for large changes of temperature.

There are other ways to implement a predictor-corrector than simply averaging the opacity σ. Another method is the Temperature Averaged Predictor-Corrector (TAPC) which averages the beginning and predicted end of time step temperature as

$$T_{n+\frac{1}{2}} = \frac{T_{n+1} + T_n}{2}. \tag{3.4}$$

This averaged temperature can then be used to calculated the temperature dependent opacity used in the corrector step. Figure 3.8 demonstrates a similar order of global error as the averaging of σ for both the Implicit Monte Carlo method and the

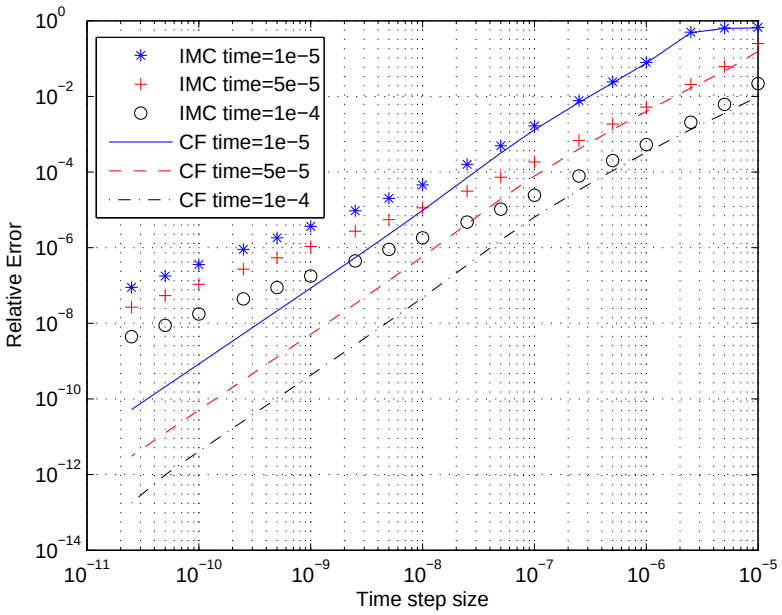

Figure 3.8: Relative error vs. time step size for Temperature Averaged Predictor-Corrector.

Carter-Forest method, but without the structure that was seen previously. At this point, there is no real reason to prefer one method over the other since the structure in the $\sigma(t_{n+\frac{1}{2}})$ predictor-corrector is related to inaccurate, large time step sizes.

Another temperature estimate proposed by A. Wollaber and E. Larsen (20) assumes a functional form of the opacity $\sigma(t) = \gamma/T(t)^3$, and that temperature change is approximately linear over a small time step. Then the average value of $\sigma(t)$ is preserved by

$$\bar{\sigma} = \frac{1}{\Delta t}\int_{t_n}^{t_{n+1}} \frac{\gamma}{T(t)^3} dt = \frac{\gamma}{T_*^3} \tag{3.5}$$

where

$$T_* = \left[\frac{T_n^2 T_{n+1}^2}{(T_{n+1}+T_n)/2}\right]^{1/3}. \tag{3.6}$$

Note that $T_* \approx \frac{T_n+T_{n+1}}{2}$ for small time step so it is expected that the Wollaber-Larsen Temperature Predictor-Corrector (WLTPC) will have similar properties to the TAPC. Using the Wollaber temperature estimation to calculated the opacities during the time step, Fig. 3.9 also shows an $O(\Delta t)$ convergence for IMC and a $O(\Delta t^2)$ convergence for CF.

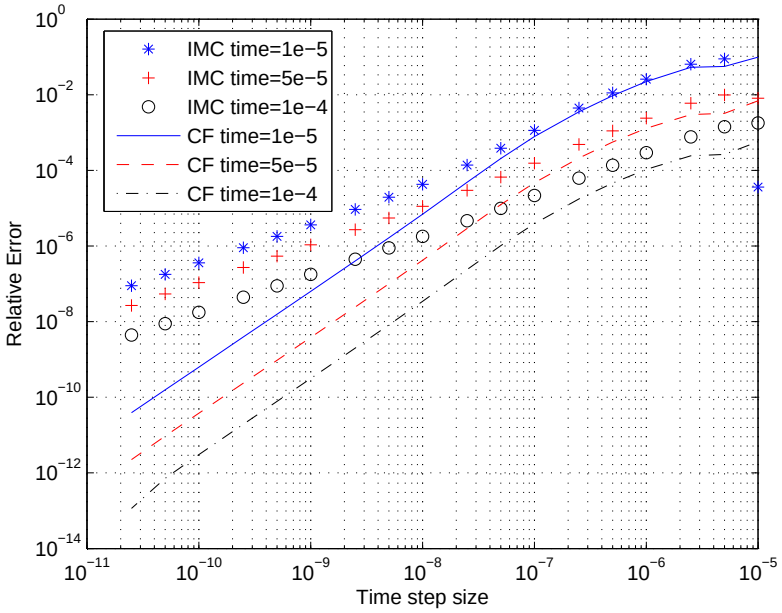

Figure 3.9: Relative error vs. time step size for Wollaber-Larsen Temperature Predictor-Corrector.

The three afore mentioned predictor-corrector methods listed here are not exhaustive, and other viable approaches may exist as long as the estimation of the value of $\sigma(t)$ is $O(\Delta t^2)$ globally. The IMC method can become $O(\Delta t^2)$ globally as well for a nonlinear problem, but then only if $\alpha = 0.5$. When $\alpha = 0.5$, the residual error caused by the IMC approximations becomes $O(\Delta t^2)$ globally. Applying a predictor-corrector to the $\alpha = 0.5$ IMC equations results in a higher order IMC method show in Fig.

3.10. While the IMC method now shows global $O(\Delta t^2)$ convergence (with slightly

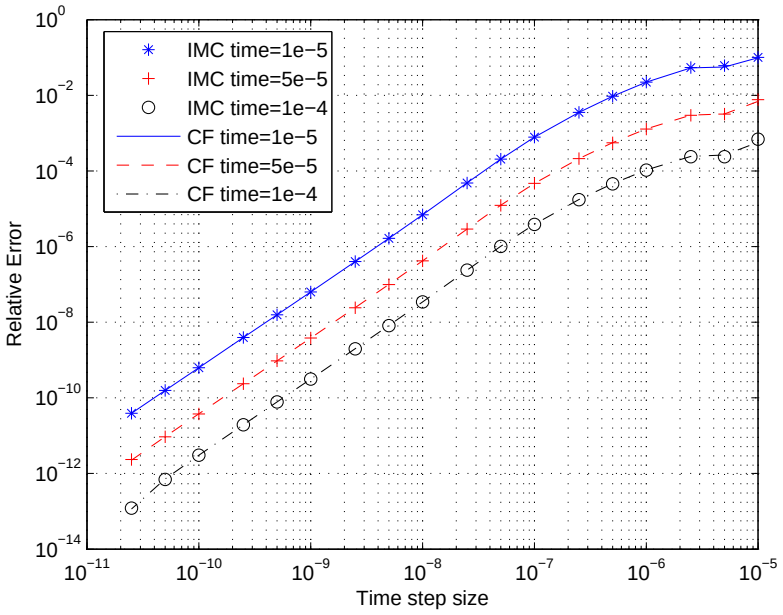

Figure 3.10: Relative error vs. time step size with Wollaber-Larsen Temperature Predictor-Corrector and $\alpha = 0.5$.

different values than the CF method), it is more precarious than the CF method due to stability concerns. Large time steps can produced non physical oscillations in the IMC solution for values of α that are not equal to 1 (15).

In the above warming and cooling problems, the value of $\beta(t)\sigma(t)$ is a constant value. To demonstrate that the approximation to the value of $\sigma(t)$ is the dominant source of truncation error over the approximation to $\beta(t)$, a new nonlinear problem is proposed. Setting $a = c = 1$, the starting material temperature $T = 0.1$, the opacity $\sigma(t) = 2000/T^2$, $\beta(t) = 40/T^3$, and a starting photon intensity of $\phi(0) = 1000cU_r(0)$, a warming problem with a larger nonlinearity in β than σ is explored, henceforth called 0D Problem 2. The TACP method is only applied to the estimation of $\sigma(t)$, however if the predictor-corrector is extended to update the approximation of $\beta(t)$, the solutions only change slightly.

The temperature at different times for Problem 2 can be seen in Fig. 3.11. Figure 3.12 shows the expected result that both the IMC and CF method are $O(\Delta t)$ globally without a predictor-corrector. When the TAPC is applied, Fig. 3.13 shows the CF method again becomes $O(\Delta t^2)$ globally while the IMC method is still $O(\Delta t)$. The CF method does asymptote out at a given relative error due to the resolution of the reference solution. If a more resolved reference solution was used, the CF method

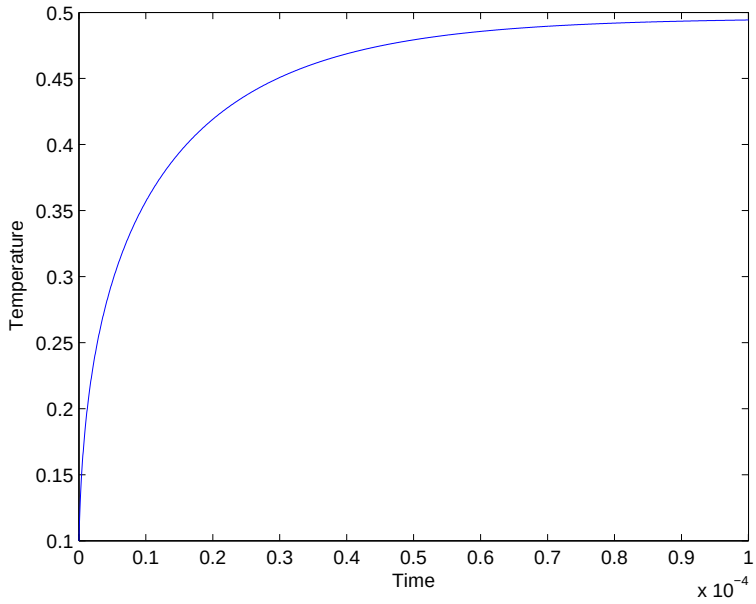

Figure 3.11: Temperature vs. time for 0D Problem 2.

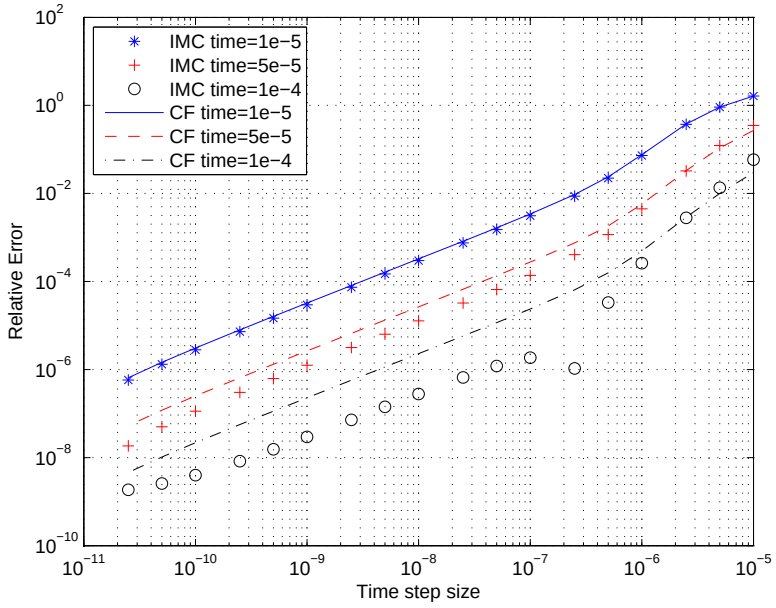

Figure 3.12: Relative error vs. time for 0D Problem 2.

would continue the $O(\Delta t^2)$ convergence.

Even though the IMC method does not benefit as greatly from the predictor-corrector methods as the CF method, there are secondary effects. In particular for large time steps in warming nonlinear problems, a time step can be taken that is far

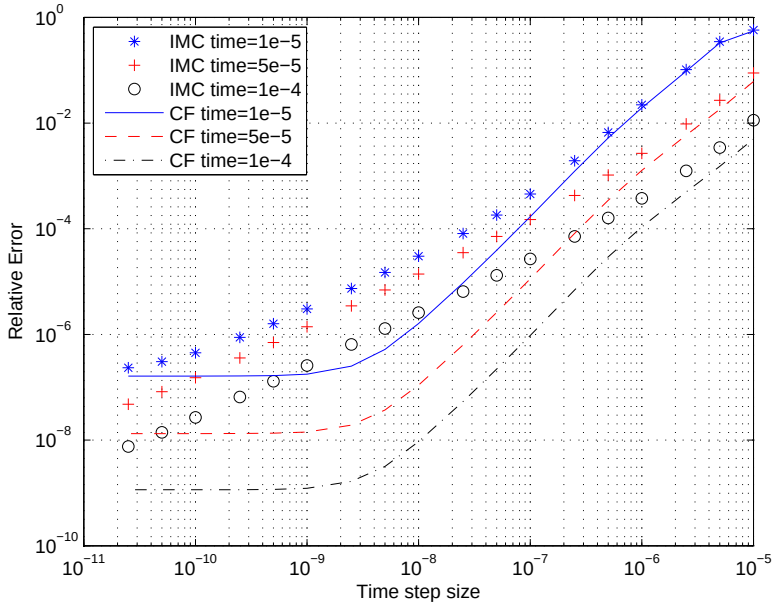

Figure 3.13: Relative error vs time for Temperature Averaged Predictor-Corrector for 0D Problem 2.

too large, keeping the opacities overly opaque for a protracted period of time. In these cases, it is possible to violate the Maximum Principle (9) such that the material temperature becomes warmer than the radiation temperature heating it. This is unphysical. To correct for this problem a smaller time step must be used to update the material temperature more frequently to change the cross-sections.

Predictor-corrector methods have a benefit of minimizing these violations of the maximum principle. Figure 3.14 shows the effect of a predictor-corrector on a time step that is too large for the first warming problem mentioned previously. The typical IMC implementation shows a large unphysical jump in temperature, then an exponential decline in temperature due to material emission and absorption. This unphysical temperature change similar to saying a block of ice is brought into a warm room and instantly turns to steam. The now cold room is warmed back to an equilibrium temperature by the hot steam. With the same large time step the predictor-corrector does not violate the maximum principle, but in this particular case it does not reconstruct the reference solution. Predictor-corrector's will not remove the need to perform accurate transport, however the effect of inaccurate transport seems to be less severe. The improved accuracy with poor transport can be explained since after a single predictor step, the end of time step temperature is nonphysically high. This high temperature is used in part to update the opacity, which in this

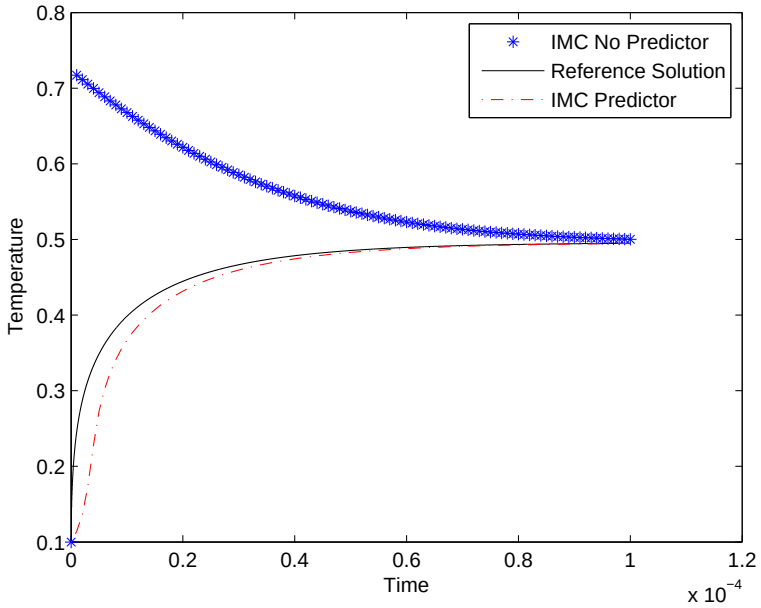

Figure 3.14: Temperature vs. time for the IMC method with $\alpha = 1$.

particular problem would make it lower than physically accurate. Therefore, photons are not correctly absorbed at the rate they are in an accurate solution. So while the predictor-corrector is an improvement with physical material temperature, it is still incorrect during the transient. As the time step size decreases, both the original and the predictor-corrector implementation of IMC will produce more accurate solutions but the predictor-corrector is clearly more robust.

3.3 Monte Carlo Predictor-Corrector Methods

Previously, deterministic methods were used to determine the relative error in the CF and IMC equations. Monte Carlo methods will now be used. Monte Carlo methods introduce another type of error from the stochastic modeling, which will be referred to as noise. While the trends of convergence remain the same, the addition of noise into the TRT equations has meaningful impact on the calculation of the end of time step temperature. Using the warming up problem described previously, 200,000 particles are used to simulate the initial source $\phi(0) = 1000cU_r(0)$. Both the IMC method with $\alpha = 1$ and the CF method can be seen in Fig. 3.15

It is easy to note the difference between the Monte Carlo methods and the deterministic methods in the relative error graphs. There is oscillation in the relative

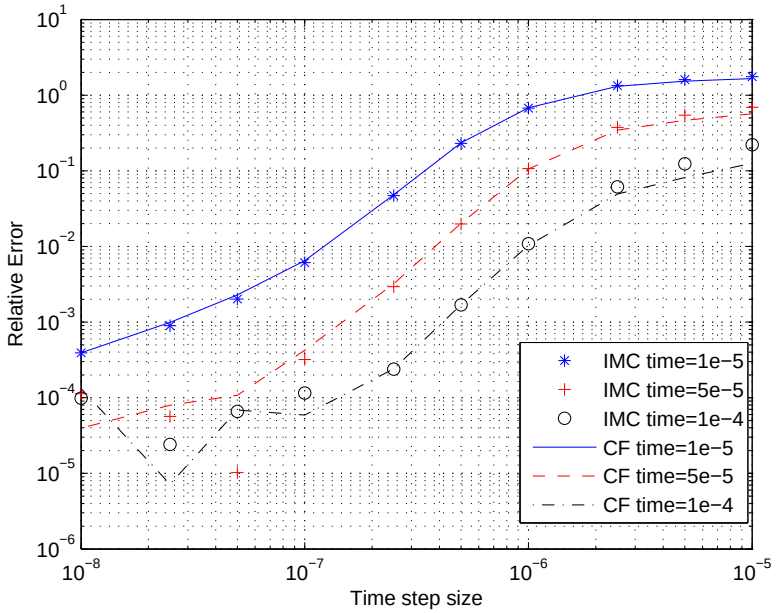

Figure 3.15: Relative error vs. time step size for Monte Carlo Methods.

error graphs when using the Monte Carlo methods, a phenomenon that was not seen in deterministic methods. For this Monte Carlo simulation, the relative error graph asymptotes to the most refined solution it can achieve at around the time step size of $\Delta t = 10^{-8}$ when the error becomes dominated by the stochastic noise. Therefore, there are limitations on how accurate a Monte Carlo solution may be based on the number of particles used in the simulation of the problem. As more and more particles are used, the stochastic noise introduced into a time step by the Monte Carlo simulation should reduce by $1/\sqrt{N_n}$ where N_n is the number of particles used at time step n. Like truncation error, Monte Carlo noise will propagate from one time step to the next. However, even in a noisy problem, improvements can be seen using predictor-correctors.

Figure 3.16 shows the WLTPC used on the warming up problem for both the IMC and CF method. The relative error is smaller in Fig. 3.16 than Fig. 3.15 but there is no apparent $O(\Delta t^2)$ convergence in the CF method. In fact, the predictor-corrector CF method quickly asymptotes off to the accuracy of the stochastic noise. It is worth while to reexamine Fig. 3.9 to note that it is around the time step size of $\Delta t = 10^{-8}$ that the $O(\Delta t^2)$ convergence for the CF method really appears to develop. Unfortunately, too few particles are used in this case to see this trend.

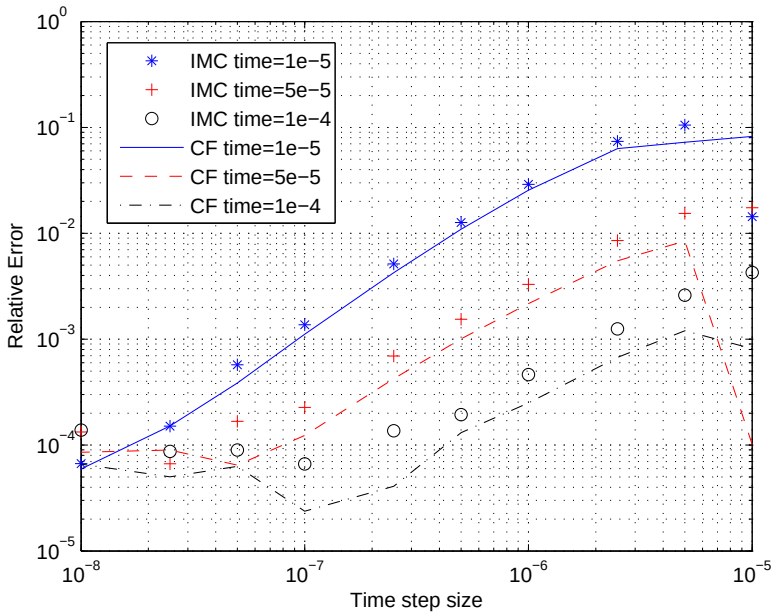

Figure 3.16: Relative error vs. time step size for Monte Carlo WLTPC

3.4 Variable Weight Predictor-Corrector Methods

While significant improvements can be seen by using predictor-corrector methods, they come at the cost of running a simulation twice per time step. For Monte Carlo methods, this cost can be particularly expensive because each photon bundle must be transported and tracked. To gain meaningful results, large numbers of these photon bundles must be modeled, which increases the overall computation time. To reduce the computational cost of a predictor-corrector method in Monte Carlo methods, we have created a variable weight predictor-corrector.

The Variable weight predictor-corrector scheme we created uses a different number of modeled photons in the predictor step than in the corrector step. The predictor particles have a higher energy per particle than the corrector particles to ensure that the total energy transported over a time step is the same. No consideration is made to linearly decrease the number of photon bundles in each cell. Instead a Russian-roulette scheme is employed to determine the location of the predictor photon bundles. Even though the predictor step could run more particles than the corrector step, we observed a significant decrease in accuracy due to a larger statistical uncertainty in the updated temperature to be used in the next time step. This statistical uncertainty always depended on the number of particles simulated in the corrector step. For this reason, we recommend that the corrector step model more particles than the predictor step.

In this thesis, fewer particles (photon bundles) are always used in the predictor step than in the corrector step.

While the predictor step will have a less accurate temperature estimate at the end of the time step, it may be good enough to be used in the corrector step to improve the accuracy of the results. This concept is similar to using a diffusion calculation before a transport calculation with one significant difference, the predictor's accuracy will scale easily with computer technology. As computers get faster, the number of particles simulated in a predictor step can be increased while the diffusion approximation's accuracy will not change.

The costly Monte Carlo predictor step is replaced by a 100 variable weight predictor for demonstration. In this case, the 100 variable predictor step uses $\frac{1}{100}$ the number of particles in the corrector step but each particle has 100 times more energy than in the corrector step. With fewer particles to simulate, the 100 variable weight simulation speed is significantly faster than a traditional predictor-corrector. The use of fewer particles in the predictor step than in the corrector step will be called a Variable Weight Predictor-Corrector (VWPC). After the end of time step values are predicted, the corrector step uses the original particles as if the predictor step had not occurred but with new material properties. Figure 3.17 shows that using a rough estimate of the end of time step temperature in the WLTPC can be sufficient for the predictor-corrector accuracy improvements. There is significantly more variability

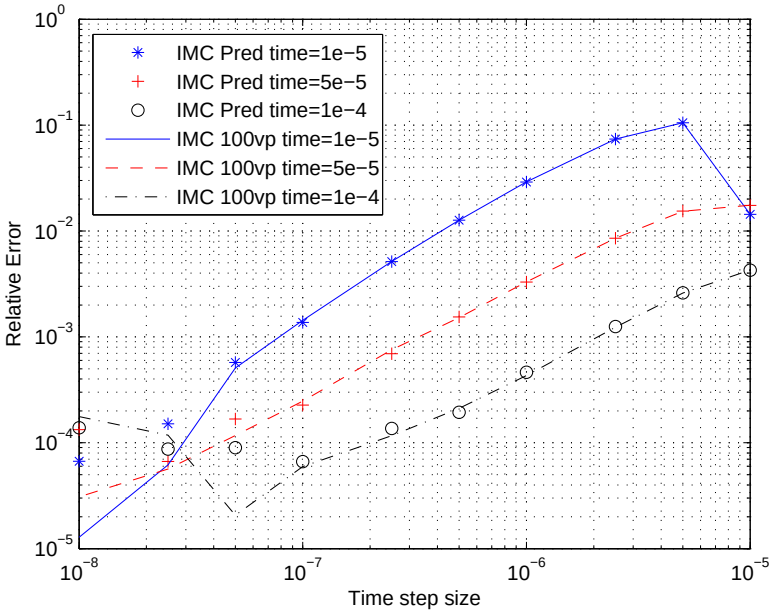

Figure 3.17: Relative error vs. time step size for traditional and 100 Variable Weight Predictor-Corrector Methods.

in the 100 VWPC method than a full predictor-corrector which can give very poor estimations of the end of time step temperature. Some care should be used when deciding how many particles should be used in the predictor step to assure confidence in the result. Selection of a down sampling value for the VWPC will be explored further in Chapter 4. Although not shown here, the CF method yields a similar result as shown in Fig. 3.17.

Chapter 4

1D Radiative Transfer

While the 0D solutions to the Radiative Transfer equations are informative, they lack the complexity of spatial leakage which occurs when spatial information is added to the photon transport. Spatial leakage occurs when photons from one cell "leak" from the cell into a neighboring cell, and this is represented by the gradient term in Eq. (1.5). Cells are created when the spatial domain of the problem is represented as a union of smaller regions. The length of these regions is referred to as the cell width in 1D problems.

4.1 Photon Teleportation

The inclusion of a spatial variable to model a radiation transport problem adds another source of error called "photon teleportation" into the solution of the radiation transport equations. Photon teleportation occurs when "the absorption mean free path is small compared to the size of a zone, and the time step size is also small" (13). As photons stream into a highly opaque cell many mean free paths thick, they preferentially tend to be absorbed at the boundary of the optically thick cell shown graphically in Fig. 4.1. However, these absorption events raise the temperature of the entire cell. When the material emits from the cell during the next time step, the detailed spatial information about photons being absorbed at the boundary has been lost and the photons are emitted uniformly from the region. This unphysical process can even allow the modeled photons to travel faster than the speed of light, an unphysical phenomenon that should be avoided.

While the most obvious solution is to decrease the width of the cells, this comes at a significant computation cost. Instead, the standard solution to this problem is to

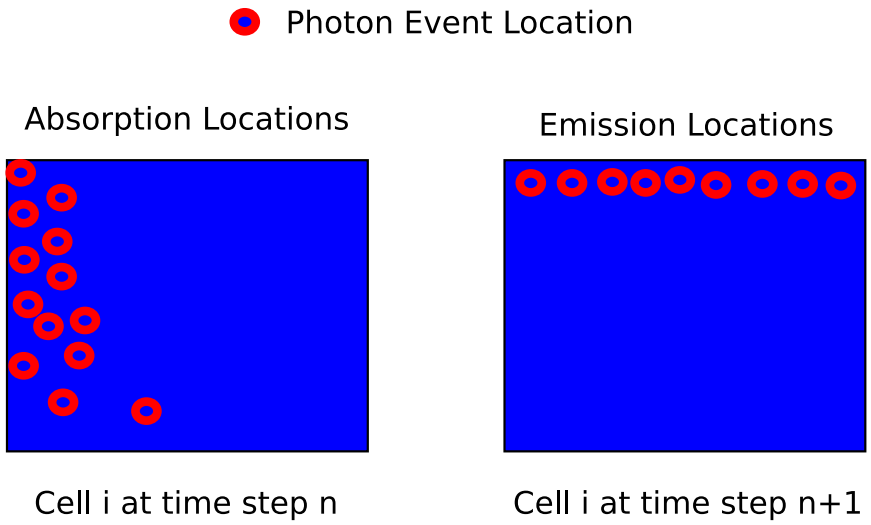

Figure 4.1: Photon absorption and reemission after one time step.

reconstruct some spatial information within each cell. This process is referred to as "source tilting" (12). Source tilting has two different implementations, both shown in Fig. 4.2.

There is one histogram for each cell and the height is a representation of the total amount of energy that the cell will emit during the time step. Lines are drawn from the center point of each histogram to its neighbors and these lines will be used to select the sampling location from within a cell. With the Tilt method, after the lines connecting the histogram center points are drawn, the height of the intercept of each line at the boundary is determined. Then a sloped line is drawn connecting these heights determined by the boundaries of the cell (red line in Fig. 4.2). The resulting area contained between the red line and the cell boundaries of Cell i is used to create a cdf. The resulting cdf is then sampled to determine the spatial location of the emission within the cell, but the number of particles that will be emitted from a cell is not changed.

Alternatively, the Histogram Lines method focuses on the slope of the connecting lines within the bin itself. Like before, the area swept out by the red lines and cell boundaries is used to create two cdfs (left and right). The left or right side of the cell is selected randomly by an area weighted cdf created by area swept out by the red lines and the cell boundaries. After determining if an emission has occurred on the left or right side of a cell, the particle location is sampled from the left or right side cdf. As the spatial cells become optically thicker, the photon teleportation errors becomes more pronounced. Both "source tilting" methods will reduce the severity of

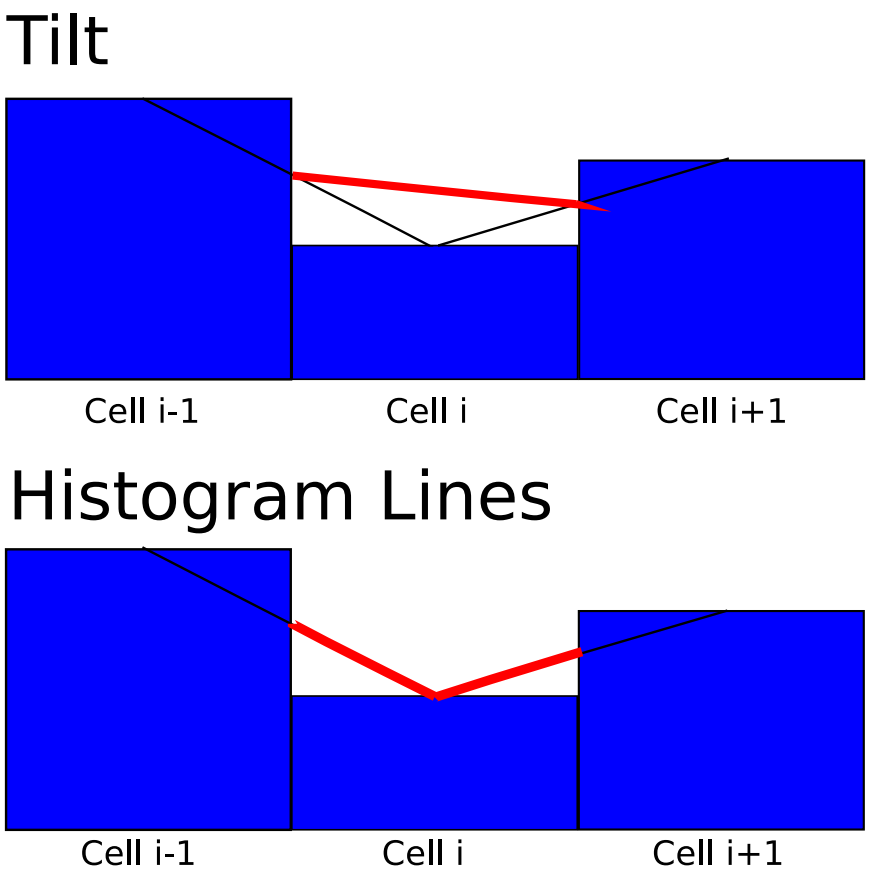

Figure 4.2: Source tilting methods.

photon teleportation, but they will not remove it.

While these "source tilting" methods are an improvement over sampling photon emission locations uniformly over a bin, they may be improved upon. When a photon is absorbed, the detailed information of the position of the absorption is lost within a histogram; this is the start of the fundamental problem of photon teleportation. While it is possible to store the exact location of the absorption and remove the photon teleportation bias (1) (11) it becomes computationally costly to store large numbers of photon absorption sites. Instead, we propose a Functional Expansion Tally (FET) as a compromise between the current source tilting methods and the very costly Arhens-Larsen method.

4.1.1 Functional Expansion Tallies (FET)

A function $p(x)$ can be approximated as

$$p(x) = \sum_{i=1}^{N} c_i B_i(x) \tag{4.1}$$

where $B_i(x)$ represents a set of basis functions and c_i are expansion coefficients. The approximation of a function in this manner is fairly common. While the basis functions are known, the coefficients multiplying them are not. To determine the coefficients, several integrals must be computed. Specifically,

$$I_k = \int_a^b D_k(x) p(x) dx \tag{4.2}$$

where $D_k(x)$ is a weighting function that may or may not be of the same type as the basis function. The I_k coefficients are the result of integrating the function of interest against a weighting function. Monte Carlo methods inherently solve problems by integration, making the calculation of I_k trivial. Every time a particle is tracked, the function $p(x)$ is being sampled. Tallying the events of interest against a weighting function will yield the I_k values without a need to alter the underlying Monte Carlo simulation.

To relate the expansion coefficients c_i and the integral coefficients I_k, Eq. (4.1) is substituted into (4.2) to yield

$$\begin{aligned} I_k &= \int_a^b D_k(x) \sum_{i=1}^{N} c_i B_i(x) dx \\ &= \sum_{i=1}^{N} c_i \int_a^b D_k(x) B_i(x) dx \end{aligned} \tag{4.3}$$

where $k = 1, 2, 3, \cdots$. This provides a set of equations to solve for the coefficients c_i. The choice of weighting and basis functions will determine the relationship between the c_i and I_k coefficients.

The basis used in this dissertation will be the Legendre polynomials, which are used as both a weighting and basis set. Because of their orthogonal nature, the Legendre polynomials have favorable features to simplify the relationship between the c_i and I_k

coefficients. Legendre polynomials are defined recursively as

$$\begin{aligned} L_0(x) &= 1 \\ L_1(x) &= x \\ L_2(x) &= \frac{1}{2}(3x^2 - 1) \\ L_{n+1}(x) &= \frac{(2n+1)xL_n(x) - nL_{n-1}(x)}{n+1}. \end{aligned} \tag{4.4}$$

These polynomials are orthogonal to each other such that

$$\int_{-1}^{1} L_i(x)L_k(x) = \frac{2}{2i+1}\delta_{ik}. \tag{4.5}$$

Since Legendre polynomials are orthogonal over the -1 to 1 domain, the values being tallied (such as absorption and emission within a cell) are simply shifted for each region defined as $a \leq x \leq b$. That is,

$$\int_{a}^{b} L_i(x_{trans})L_k(x_{trans}) = \kappa_i\delta_{ik} \tag{4.6}$$

where

$$x_{trans} = 2\frac{x-a}{b-a} - 1 \tag{4.7}$$

and

$$\kappa_i = \frac{b-a}{2i+1}. \tag{4.8}$$

Therefore, the value of x_{trans} resides between the values of -1 to 1 regardless of the value of x in an arbitrary domain from a to b.

Using the first two legendre moments for the basis functions and the weighting functions in Eq. 4.3 yields the system of equations

$$\begin{bmatrix} \int_a^b D_0(x)B_0(x)dx & \int_a^b D_0(x)B_1(x)dx \\ \int_a^b D_1(x)B_0(x)dx & \int_a^b D_1(x)B_1(x)dx \end{bmatrix} \begin{bmatrix} c_0 \\ c_1 \end{bmatrix} = \begin{bmatrix} I_0 \\ I_1 \end{bmatrix}. \tag{4.9}$$

Using the orthogonal properties shown in Eq. (4.6), Eq. (4.9) can be solved for the coefficients c_i as

$$\begin{bmatrix} c_0 \\ c_1 \end{bmatrix} = \frac{1}{\kappa_0\kappa_1} \begin{bmatrix} \kappa_1 & 0 \\ 0 & \kappa_0 \end{bmatrix} \begin{bmatrix} I_0 \\ I_1 \end{bmatrix}. \tag{4.10}$$

When plotting the basis functions modified by the coefficients c_i, a shifted x_{trans} value

must be used to interpret the Legendre expansions outside of the -1 to 1 domain. The reconstructed line from the Legendre FET is normalized to be a pdf then used to sample the emission location of particles.

Unlike the traditional "source tilting" methods, the Legendre FET's do not require information from outside of the cell. However, Legendre FET's may become negative over a cell (an unphysical solution to the emission and absorption function). To avoid this problem, another FET based on Maximum Entropy (7) is used to ensure positivity. Maximum entropy is a method that determines the distribution with the largest entropy value, typically based on Shannon Entropy (7).

Shannon Entropy is used in Information Theory as a metric for uncertainty associated with a distribution. The more uncertainty in the distribution, the larger the Shannon Entropy of the system. With the Maximum Entropy FET, a distribution is sought that has the largest uncertainty based on given constraints. While maximizing uncertainty is counter intuitive when seeking an accurate solution, fundamentally the Maximum Entropy method ensures that no other assumptions other than the constraints are used to determine the final distribution reconstruction. Only the given constraints for the optimization are used to solve for the functional form of the FET.

The value of the Shannon Entropy for a distribution $\phi(x)$ is defined as

$$E_{\text{shannon}} = -\int_X \phi(x)\ln(\phi(x)). \tag{4.11}$$

where X is the domain of $\phi(x)$. Constraining the entropy with a basis set $B_i(x)$ as

$$\int_X B_0(x)\phi(x)dx = \phi_0 \tag{4.12}$$

$$\int_X B_1(x)x\phi(x)dx = \phi_1, \tag{4.13}$$

Lagrange multipliers are used to define an augmented entropy

$$\begin{aligned}\Lambda(\phi,\lambda_0,\lambda_1) = &-\int_X \phi(x)\ln(\phi(x))dx + \lambda_0\left(\phi_0 - \int_X B_0(x)\phi(x)dx\right) \\ &+ \lambda_1\left(\phi_1 - \int_X B_1(x)\phi(x)dx\right)\end{aligned} \tag{4.14}$$

and a maximum point of $\Lambda(\phi,\lambda_0,\lambda_1)$ is sought. To find the stationary points in this equation, the value of $\phi(x)$ is perturbed as $\phi(x)+\epsilon Q$ where ϵ is the magnitude of the arbitrary noise Q. Taking the difference of the perturbation and the original function

over ϵ and suppressing the nonessential notation yields

$$\frac{\Lambda(\phi+\epsilon Q)-\Lambda(\phi)}{\epsilon} = \frac{1}{\epsilon}\Bigg[-\int_X (\phi+\epsilon Q)\ln(\phi+\epsilon Q)dx + \lambda_0(\phi_0 - \int_X B_0[\phi+\epsilon Q]dx) \tag{4.15}$$
$$+ \lambda_1(\phi_1 - \int_X B_1[\phi+\epsilon Q]dx) + \int_X \phi\ln(\phi)dx - \lambda_0(\phi_0 - \int_X B_0\phi dx)$$
$$- \lambda_1(\phi_1 - \int_X B_1\phi dx)\Bigg].$$

Canceling terms, (4.15) can be simplified to be

$$\frac{\Lambda(\phi+\epsilon Q)-\Lambda(\phi)}{\epsilon} = \frac{1}{\epsilon}\Bigg[-\int_X (\phi+\epsilon Q)\ln(\phi+\epsilon Q)dx \tag{4.16}$$
$$- \lambda_0\int_X B_0\epsilon Q dx - \lambda_1\int_X B_1\epsilon Q dx + \int_X \phi\ln(\phi)dx\Bigg].$$

Taylor expanding around $\epsilon = 0$ the expression

$$\ln(\phi+\epsilon Q) = \ln(\phi) + \frac{\epsilon Q}{\phi} + O(\epsilon^2) \tag{4.17}$$

can be used in Eq. (4.16) to cancel another term and yield the expression

$$\frac{\Lambda(\phi+\epsilon Q)-\Lambda(\phi)}{\epsilon} = \frac{1}{\epsilon}\int_X Q\Bigg[-\epsilon - \epsilon\ln(\phi) - \lambda_0 B_0\epsilon - \lambda_1 B_1\epsilon + O(\epsilon^2)\Bigg]dx. \tag{4.18}$$

Taking the limit $\epsilon \to 0$, Eq. (4.18) is rewritten as

$$\frac{d\Lambda(\phi)}{d\epsilon} = \int_X -Q\Bigg[1 + \ln(\phi) + \lambda_0 B_0 + \lambda_1 B_1\Bigg]dx. \tag{4.19}$$

To find the maximum, the derivative of Eq. (4.19) is set to 0 for every arbitrary perturbation Q, implying that the integrand must be equal to zero for a maximum or a minimum to exist in the function. Therefore,

$$0 = 1 + \ln(\phi) + \lambda_0 B_0(x) + x\lambda_1 B_1(x). \tag{4.20}$$

Solving for ϕ yields the distribution with the maximum entropy for the given constraints. Using Legendre Polynomials as the basis set $B_i(x)$ the distribution ϕ is

defined as

$$\begin{aligned}\phi(x) &= e^{(-1-\lambda_0 B_0(x)-\lambda_1 B_1(x))} \\ &= \alpha e^{\eta x}\end{aligned} \tag{4.21}$$

where $\alpha = e^{-1-\lambda_0}$ and $\eta = -\lambda_1$. Next, the values of α and η are solved for by using the constraints

$$\begin{aligned}\phi_0 &= \int_X \alpha e^{\eta x} \\ \phi_1 &= \int_X x\alpha e^{\eta x}.\end{aligned} \tag{4.22}$$

Using shifted Legendre polynomials in domain X defined as $a \leq x \leq b$, these equations become

$$\begin{aligned}\phi_0 &= \int_a^b \alpha \exp\left(\eta\left[2\left(\frac{x-a}{b-a}\right)-1\right]\right) \\ &= \frac{\alpha(b-a)\sinh(\eta)}{\eta}\end{aligned} \tag{4.23}$$

and

$$\begin{aligned}\phi_1 &= \int_a^b \alpha\left[2\left(\frac{x-a}{b-a}\right)-1\right]\exp\left(\eta\left[2\left(\frac{x-a}{b-a}\right)-1\right]\right) \\ &= \frac{\alpha(a-b)(-\eta\cosh(\eta)+\sinh(\eta))}{\eta^2}.\end{aligned} \tag{4.24}$$

Knowing the values of both ϕ_0 and ϕ_1, Eqs. (4.23) and (4.24) can be divided to cancel the value of α and give the transcendental function

$$\frac{\phi_0}{\phi_1} = \frac{\eta\sinh(\eta)}{\eta\cosh(\eta)-\sinh(\eta)} \tag{4.25}$$

which can be root solved for the value of η. The value of α is simply solved for using the first constraint rearranged to show

$$\alpha = \frac{\phi_0\eta}{(b-a)\sinh(\eta)}. \tag{4.26}$$

The procedure to solve α and η must be done once per time step per cell. Using a simple bisection root solver, there appears to be negligible computation cost for

the method. It is also worth mentioning that there is no value of η in Eq. (4.26) that can make the parameter $\alpha < 0$. Since α is always positive, the Maximium Entropy distribution $\phi(x)$ in Eq. (4.21) is always positive when using the first two Legendre polynomial constraints. Therefore, the Legendre Polynomial Maximum Entropy (Legendre-ME, or Legendre) FET does not require any positivity checks or corrections before being sampled for emission locations.

To sample the Legendre-ME FET, a pdf must first be created by normalizing the reconstructed distribution. Integrating over the cell bounds, the normalization value Ξ can be determined as

$$\begin{aligned} \Xi &= \int_a^b (\alpha \exp[\beta(2\frac{x-a}{b-a} - 1)])dx \\ &= \frac{(b-a)\alpha \sinh(\beta)}{\beta}. \end{aligned} \tag{4.27}$$

Next, the pdf to be inverted is defined as

$$p(x) = \frac{\alpha \exp[\beta(2\frac{x-a}{b-a} - 1)]}{\Xi}. \tag{4.28}$$

Integrating the pdf from a to x

$$\begin{aligned} \xi &= \frac{\int_a^x \alpha \exp[\beta(2\frac{x-a}{b-a} - 1)]dx}{\Xi} \\ &= \frac{-1 + \exp[\frac{-2(x-a)\beta}{b-a}]}{-1 + \exp[2\beta]} \end{aligned} \tag{4.29}$$

which forms the cdf that is inverted to yield

$$x = a + \frac{(b-a)\log[1 - (1 - e^{2\beta})\xi]}{2\beta}. \tag{4.30}$$

Therefore, there is no need to calculate the value of α to sample the location of an emission.

In practice, the values for ϕ_0 and ϕ_1 are calculated by tallying the photon energy from emissions and absorptions against the basis function. The convention is absorptions have a positive contribution to the tally and emissions have a negative contribution to the tally. Also the tallies are not reset from time step to time step, so the values used for ϕ_0 and ϕ_1 at time step n contain tallied information for absorption and emission of the last $n-1$ time steps. The persistance of information from one time step to the next has only one drawback to note: there can exist values of $\frac{\phi_0}{\phi_1} < 1$

which implies that there is no solution for η. While these situations are rare, they do occur and in these cases the value of η is chosen as 0, causing the Legendre-ME FET to produce a constant distribution in space.

4.1.2 The Su-Olsen Problem

To determine the effect of traditional "source tilting" compared to the FET approach, a non-physical 1D problem with analytical solutions proposed by Su and Olson (19) is used. In the Su-Olsen problem, the radiation constant $a = 1$, the opacity $\sigma(T) = 1$, and $\beta(T) = 1$; a reflective left boundary condition is imposed and a time dependent isotropic 1 keV source that emits uniformly temporally between $0 \leq t \leq 10$ and spatially between $0 \leq x \leq 0.5$. The 1 keV photon source is no longer active after time $t = 10$. Fig. 4.3 shows the analytic solution for the Su-Olsen problem at different times.

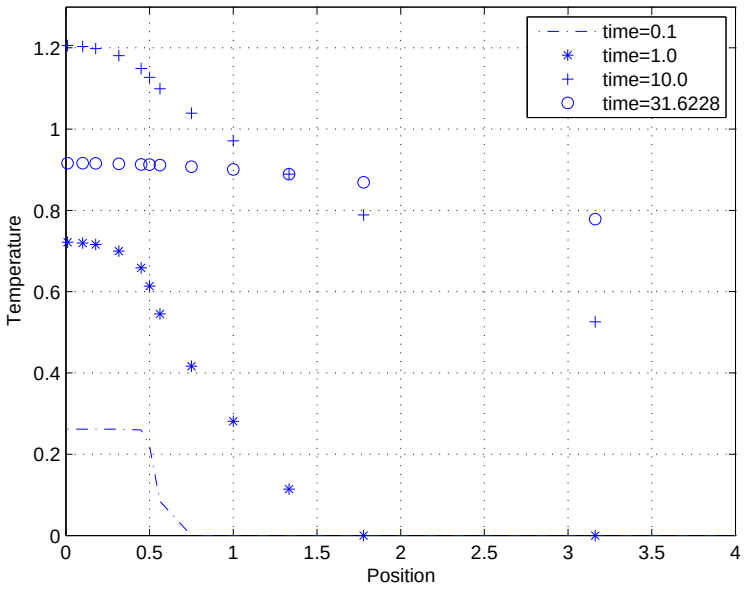

Figure 4.3: Reference solutions for the Su-Olsen Problem.

Until $t = 10$ the total energy in the problem is increasing, causing a rise in temperature near the left boundary at the source location. As the problem continues in time, the photons begin streaming out of the source region and continue into the non-source region, creating a wave effect that has an exponentially decaying wave front. After $t = 10$, the source cuts off and the source region begins to cool as the radiation continues to transport away from the source region.

When a large time step is taken, $\Delta t = 1$, then the IMC bias can be seen in 1D solutions compared to the reference solution in Fig. 4.4, while the Carter-Forrest method is still accurate. Fundamentally, the IMC bias will put an upper limit on an accurate time step size. The Carter-Forrest method does not have the same time step limit as the IMC method on this linear problem. However, both the IMC and CF method will have photon teleportation errors. To determine the effect of "source

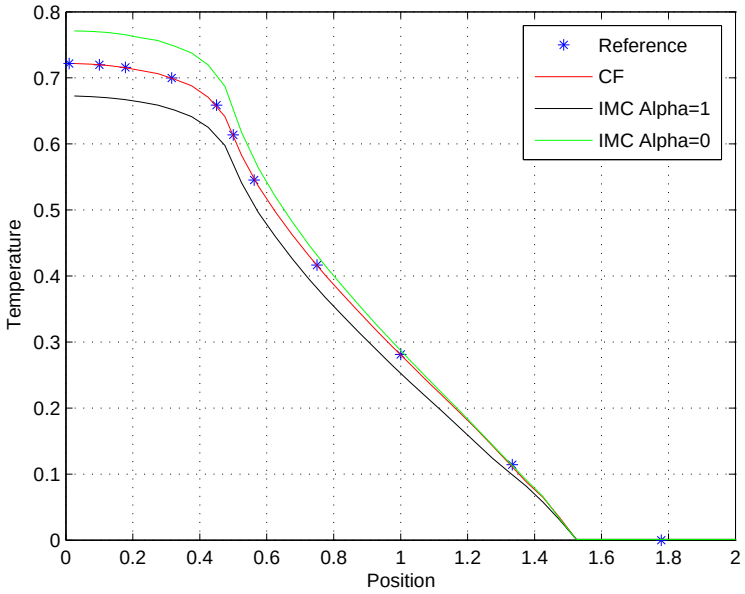

Figure 4.4: One-D bias of the IMC equations on the Su-Olsen Problem at time $t = 1$.

tilting", a reference solution is created using a well converged Monte Carlo solution that agrees with the analytic solution. This is then compared to different tilting methods to determine their effectiveness in correcting photon teleportation.

Using Legendre Polynomial Maximum Entropy (Legendre-ME or Legendre) FET's, Tilt, Histogram Lines and histograms at different spatial widths and a fixed time step size of 0.005, the error of each method is examined at time $t = 5$. Using the spatial widths 0.5, 0.25, 0.1, 0.05, and 0.025 the temperature of each spatial cell is determined. To compare the solutions from different spatial widths, the cell temperatures are combined to form a larger bin size of 0.5. The larger averaged bin size will be used to achieve a meaningful comparison of the different methods at differing spatial widths. Since the material energy density U_m is a nonlinear function of temperature, averaging the temperature of the small bins to form a larger one will be explained in more depth. The procedure of compressing bins to a width of 0.5 is as follows:

1. Determine the number of smaller cells, N, that are required to span the total

spatial width of 0.5

2. Average the material energy densities, U_m, of the N equally sized cells
3. Calculate the temperature of the larger combined cell of width 0.5 using

$$T = (\frac{4\sum_N U_{m,n}}{C_v})^{\frac{1}{4}}$$

The resulting temperatures for the different compressed spatial widths are compared against a refined IMC reference solution ($\Delta t = 0.0025$ and $\Delta x = 0.01$) that was compressed and used the Tilt method for source tilting. The relative error for the first and second bin (from $x = 0.0$ to $x = 0.5$ and $x = 0.5$ to $x = 1.0$ respectively) for each of the methods is shown in Figs. 4.5a and 4.5b.

In both figures, as expected, the traditional source tilting methods Tilt and Histogram Lines perform better than the histogram approach. For this particular problem, the Legendre-ME FET's is competitive with traditional source tilting methods. To better illustrate this point, in Fig. 4.6 the first six compressed bins are added together ($x = 0.0$ to $x = 3.0$) to show the combined effect on the progression of the photon wave. In this particular problem, the Legendre-ME FET's appear to give an overall competitive solution for the bin widths used in this problem.

Figure 4.6 also shows that the overall relative error for the Legendre-ME FET's is not significantly different from the other source tilting methods. However, the bin widths used to explore the Su-Olsen problem are at largest, 0.5 mean free paths. To determine the effect of FET's and source tilting with optically thick cells, a new linear problem is proposed.

4.1.3 High Opacity Linear Problem

A new problem is proposed where the material opacities are kept constant at $\sigma = 100$, using the constants $c = a = 1$, the heat capacity varies with temperature as $C_v = 4T^3$ which gives a constant value of $\beta = 1$, and a left boundary isotropic 1 keV source heats the problem with with vacuum boundary conditions. Since the problem is linear, the temperature rise in the material will have an exponential decay tail away from the source region as in the Su-Olsen problem. Examining the temperature solution at time $t = 10$, the effect of photon teleportation can be seen. Figures 4.7 and 4.8 show both the reference solution ($dx = 0.01$ $dt = 0.05$) and the effect of using larger cell widths while using the source tilting methods. As the spatial width increases, the front location shifts away from the reference solution. Photon teleportation is allowing the photon wave front to penetrate further into the slab than should be physically

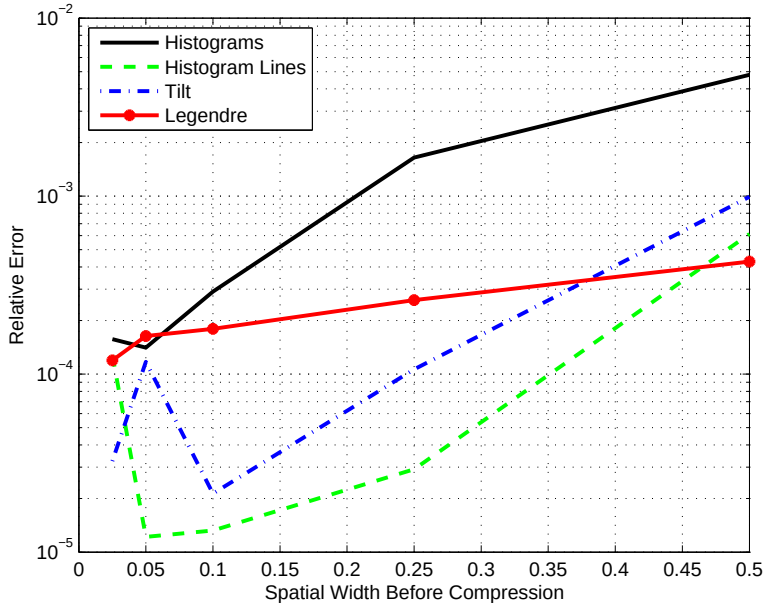

(a) Relative error of the first bin $0 \leq x \leq 0.5$.

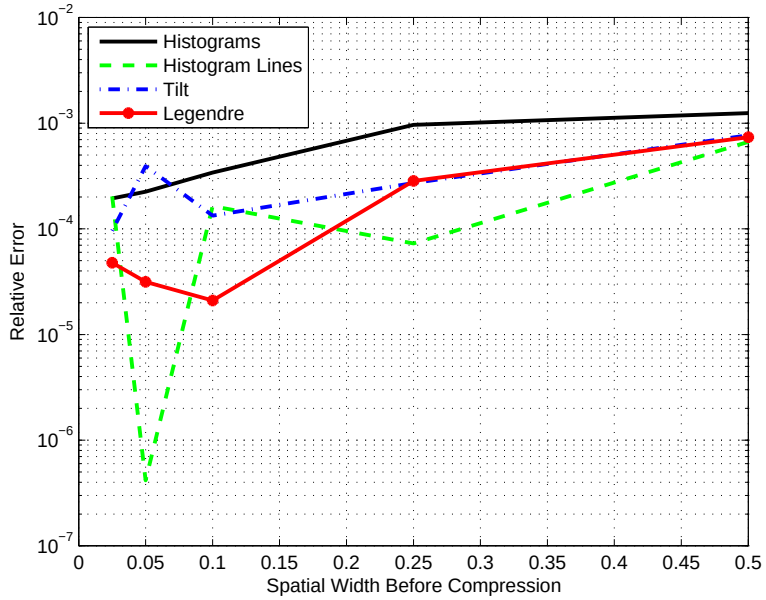

(b) Relative error of the second bin $0.5 \leq x \leq 1$.

Figure 4.5: Relative error of different compressed bin widths in the Su-Olsen problem.

possible.

Using a 1 mean free path width cell ($dx = 0.01$) changing the time step size by an order of magnitude does not significantly change the wave front. However, when the thickness of the cell becomes 5 mean free paths ($dx = 0.05$), photon teleportation

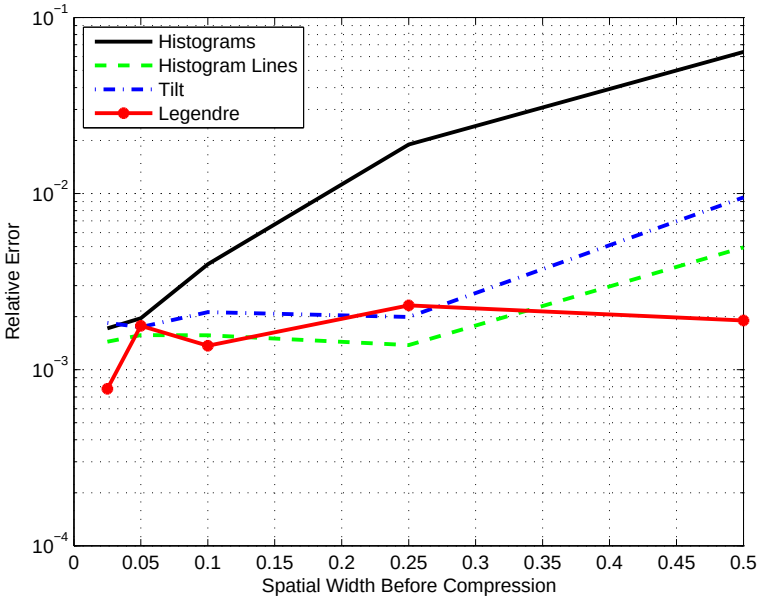

Figure 4.6: Sum of the relative error for different compressed bin widths $0 \leq x \leq 3$. in the Su-Olsen problem

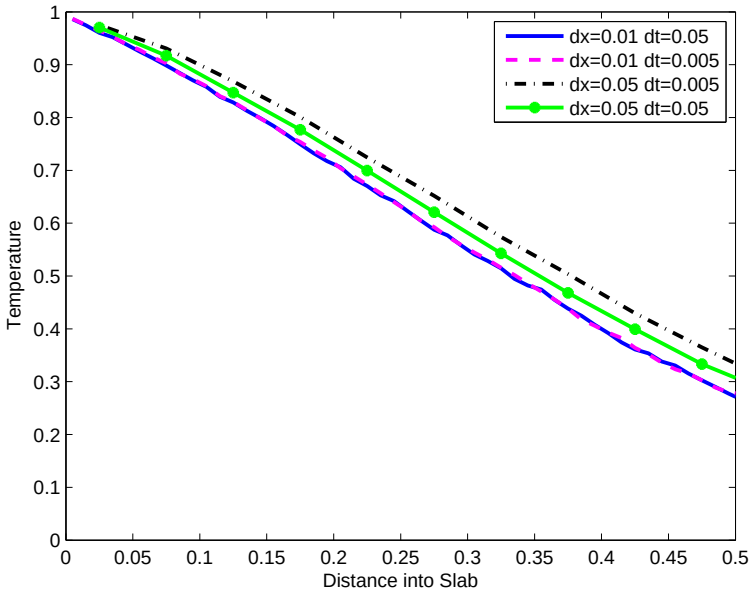

Figure 4.7: Photon teleportation in the High Opacity Linear Problem using Tilt.

can be seen. As was previously warned, a smaller time step size actually exacerbates the problem making photon teleportation much more pronounced. Therefore, a small spatial width must be used to counter act this unphysical phenomenon, adding to the

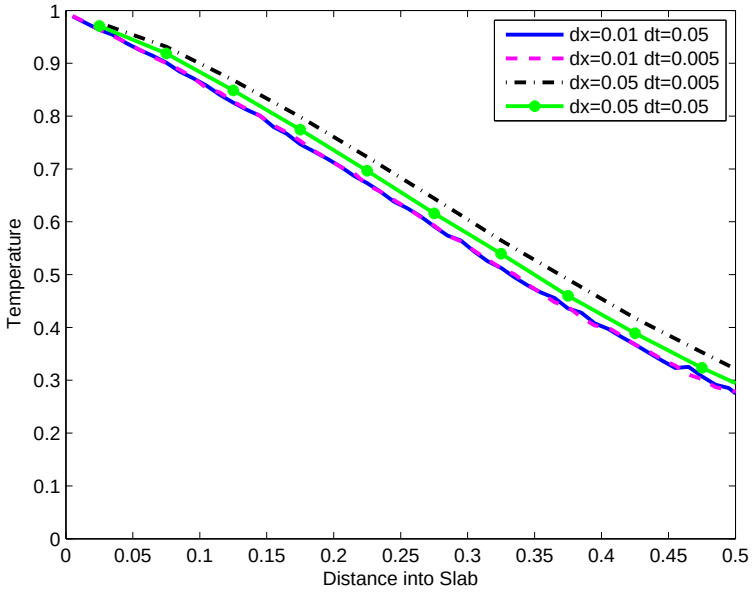

Figure 4.8: Photon teleportation in the High Opacity Linear Problem using Histogram Lines.

computational cost of the problem.

However, using the Legendre-ME corrected FET's show a significantly different story. Shown in Fig. 4.9, the 5 mean free path, small time step run is indistinguishable from the reference solution in the region in question. These results are replicated with even larger spatial widths demonstrating that the Legendre-ME corrected FET's can be used to significantly reduce photon teleportation in optically thick cells compared to the traditional source tilting techniques that are currently employed. While these results are informative, they come from a non-physical problem where the opacities remain constant during temperature changes. To better explore the potential of FET's a nonlinear 1D problem is needed.

4.1.4 Nonlinear 1D Problem

A more realistic photon transport problem has been proposed (20) with a unit isotropic source located on the left boundary, which is a vacuum boundary. The right boundary has a reflective boundary condition. The physical parameters are set as the radiation constant $a = 1$, speed of light $c = 1$, a constant heat capacity $C_v = 1/0.14$, with temperature dependent opacity $\sigma(T) = 1/T^3$, and $\beta(T) = 0.56T^3$. The starting material temperature of the slab is $T = 0.1$keV. In these problems, time is given

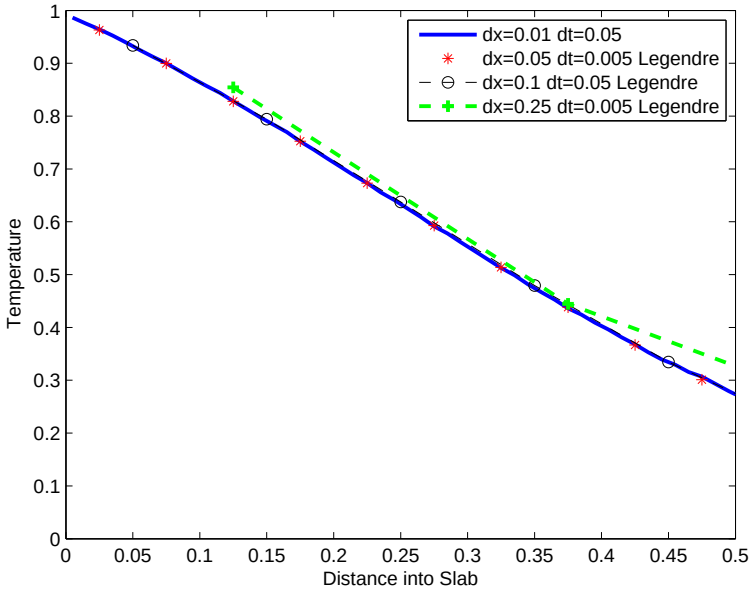

Figure 4.9: Reference solution and Legendre-ME FET solution in the High Opacity Linear Problem.

using the scaled variable τ where $\tau = C_v t$. Figure 4.10 shows the propagation of the rise in temperature of the material due to photon energy deposition. Unlike the Su-Olsen problem there is no exponential tail in this nonlinear problem due to the exceptionally high opacities at the front of the wave. As the material warms up, the material opacities decrease allowing the radiation to transport farther into the slab. These nonlinear temperature/photon waves are called "Marshak waves".

To demonstrate photon teleportation, Fig. 4 shows the location of the Marshak wave fronts using a time step of $\Delta\tau = 0.01$ and different spatial widths at $\tau = 10$ with the IMC method. For the same time step size, it is clear that the larger the spatial width is, the farther the Marshak wave propagates into the problem. To have a Marshak wave heat more material, it requires more energy. In Fig. 4 it is clear that the extra energy to raise the total energy of the slab comes from a decrease in spatial leakage from the left vacuum boundary condition.

This problem highlights the challenges in resolving an accurate solution when using increasingly thick spatial cells in a nonlinear problem. As the cells become thicker, photon teleportation plays a larger role in the transport of photons and the Marshak wave penetrates further into the slab than a more refined spatial width would show. To combat this effect, smaller and smaller spatial widths must be used to alleviate this problem.

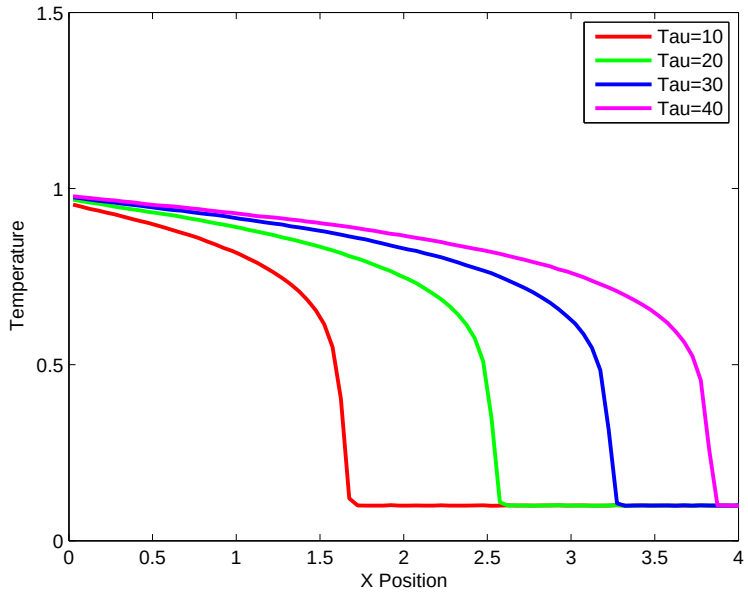

Figure 4.10: Marshak wave propogration for $\Delta\tau = 0.1$ and $\Delta x = 0.05$ at different times in the Nonlinear Problem.

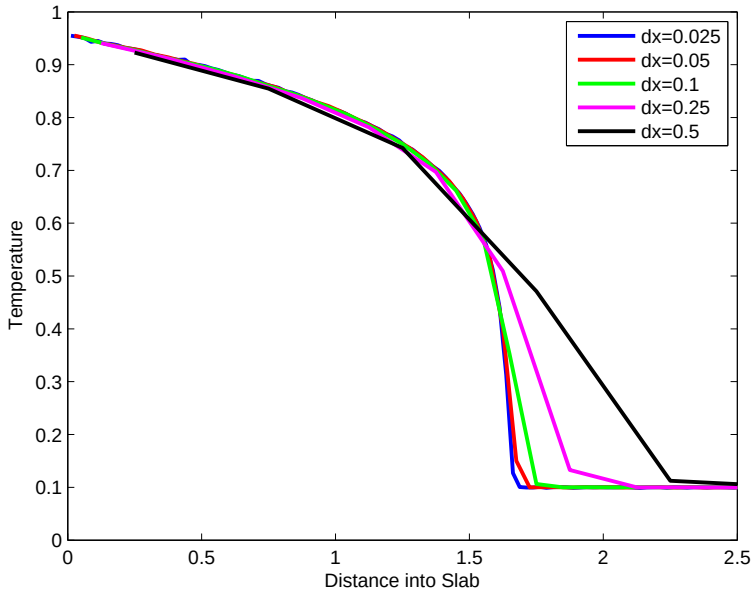

Figure 4.11: Marshak wave fronts with different for different spatial widths in the Nonlinear Problem.

A comparison of source tilting techniques is now applied to the nonlinear problem to determine the effectiveness of each method. As before in the Su-Olsen problem, different cell widths are appropriately combined to compare temperatures at spatial

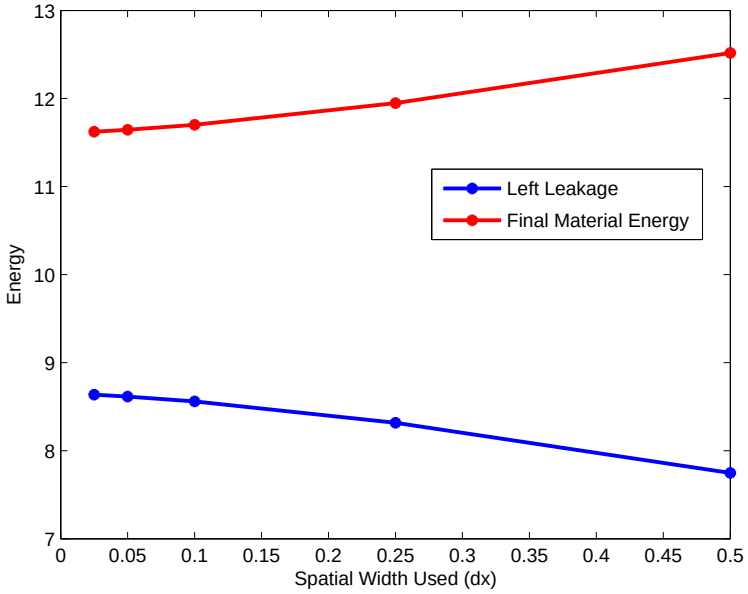

Figure 4.12: Energy tallies for leakage and material for different spatial widths.

widths of 0.5. Using spatial widths of 0.025, 0.05, 0.1, 0.25, and 0.5, the IMC method is used with a time step size of $\Delta t = 0.01$. The relative error of the combined temperature cells is examined at time $\tau = 10$. As in the Su-Olsen problem, Figs. 4.13 and 4.14 show the Tilt and Histogram Lines method of source tilting to be an improvement on the histogram approach. However, the Legendre-ME FET's appear to give a significant improvement of accuracy at large spatial widths and a result that is competitive or better at smaller widths.

The relative error of the first four bins are plotted together in Fig. 4.15 which shows that overall the Legendre-ME FET yields a significant improvement over traditional source tilting methods. For large spatial widths, the Legendre-ME FET's are an order of magnitude more accurate than the traditional source tilting implementations. As seen in Fig. 4.16, it is clear that the Legendre-ME results are much better at resolving the Marshak wave fronts for large spatial widths.

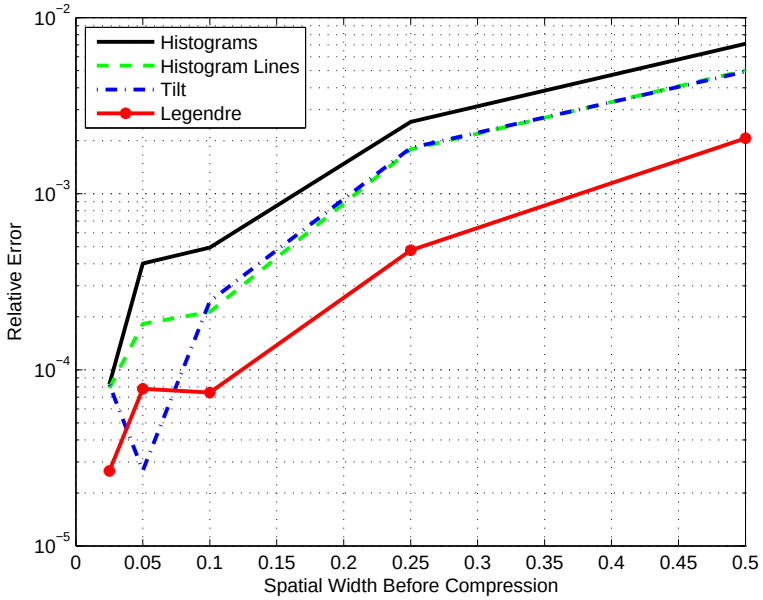

Figure 4.13: Relative error of the first compressed bin $0 \leq x \leq 0.5$ for the Nonlinear Problem.

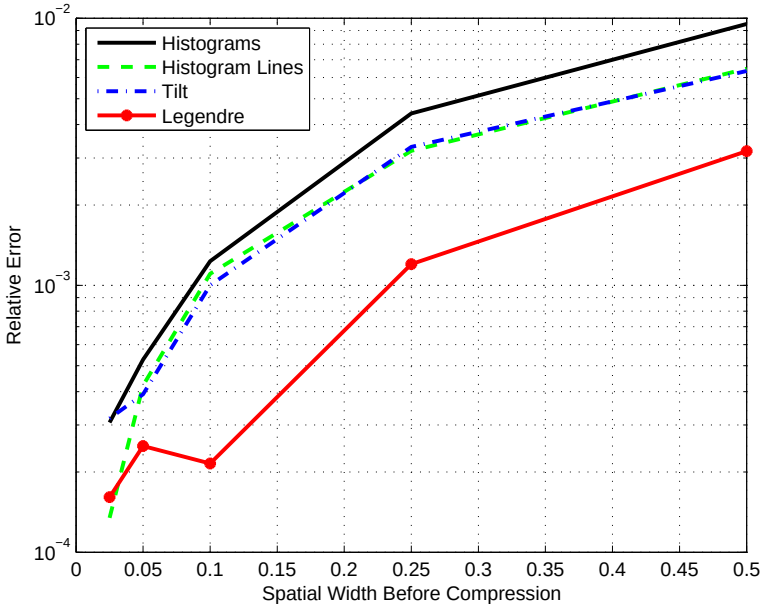

Figure 4.14: Relative error of the second compressed bin $0.5 \leq x \leq 1$ for the Nonlinear Problem.

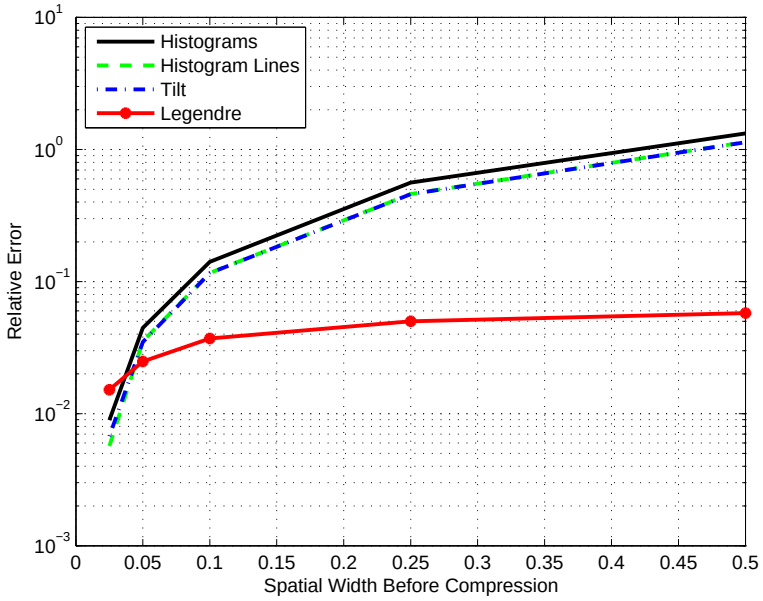

Figure 4.15: Sum of the relative error for the first four compressed bins $0 \leq x \leq 2.0$ in the Nonlinear Problem.

While the Legendre-ME FET's more closely resemble the reference solution than the current source tilting methods, the Legendre-ME method does not eliminate photon teleportation. Like traditional source tilting methods, the photon teleportation is minimized but not eliminated. However, the Legendre-ME FET's demonstrate a significant improvement in photon teleportation reduction over the current techniques.

4.2 1D Predictor-Corrector Methods

The IMC and CF methods differ on how much energy they keep in the material and in the photon field as shown previously. These differences can have unintuitive effects on accuracy as seen in Fig. 3.3a. While the IMC method bias improves the accuracy of the solution in this specific 0-D problem, in general the bias will not offset other errors in the simulation. This is more clearly seen in problems that contain a spatial dependency. In 1-D simulations predicting the effect of the bias is more challenging. Since the temperature of the material changes its' opacity, this effects the ability of radiation to stream through the region and therefore the ability to leak into a neighboring region. By modifying the leakage from one cell to another, the Marshak wave speed can be altered from the correct solution, making the IMC bias a much more complicated phenomenon.

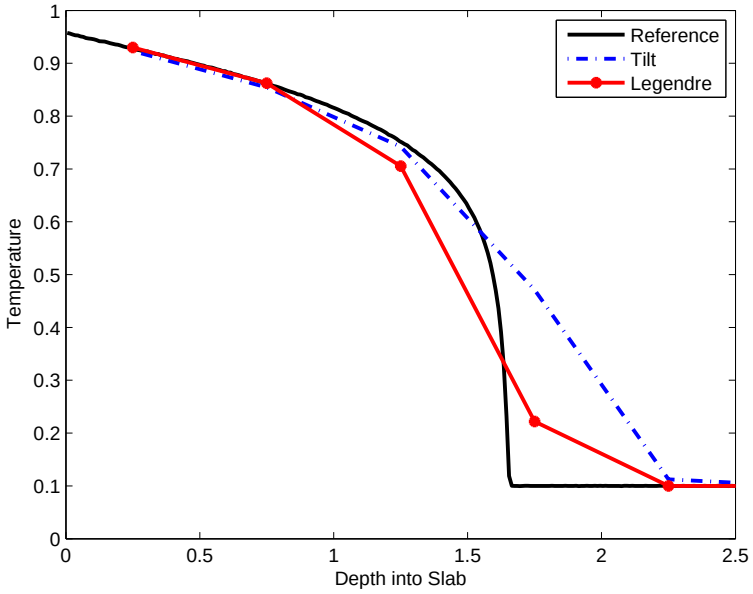

Figure 4.16: Wave front location with $\Delta x = 0.5$ at time $\tau = 10$ in the Nonlinear Problem.

To see the differences between the IMC and CF method, the 1D nonlinear problem is modeled with a spatial width of $\Delta x = 0.05$, $\alpha = 1$, and time step size $\Delta\tau = 0.1$ out to time $\tau = 20$. All of the following simulations will be using the traditional source tilting technique "Tilt". Figure 4.17a shows that the IMC method and the CF method are numerically similar away from the Marshak Wave Front. However, zooming in on the Wave Front in Fig. 4.17b shows that the IMC method has a lower temperature than the CF method which changes the exact wave front location.

At the Marshak wave front, there is a large difference between the equilibrium energy density U_r and the photon flux ϕ. Therefore, it is expected that the Marshak wave front should manifest the region with the largest IMC bias. As the size of the time step decreases, both the IMC and CF solution approach the same result, though the CF solution changes less than the IMC solution. With each smaller time step the Marshak wave front moves slightly forward and changes the simulated wave front location. This is an expected result since as the time step size becomes smaller, the material opacities are more accurately represented, allowing more radiation to stream through a cell instead of being absorbed by incorrect, large opacities.

The approximation of the opacities as constant over a time step has a significant side effect if the opacity is too large for too long for a given radiation density. The material cell may absorb far too much energy to the point that the results no longer

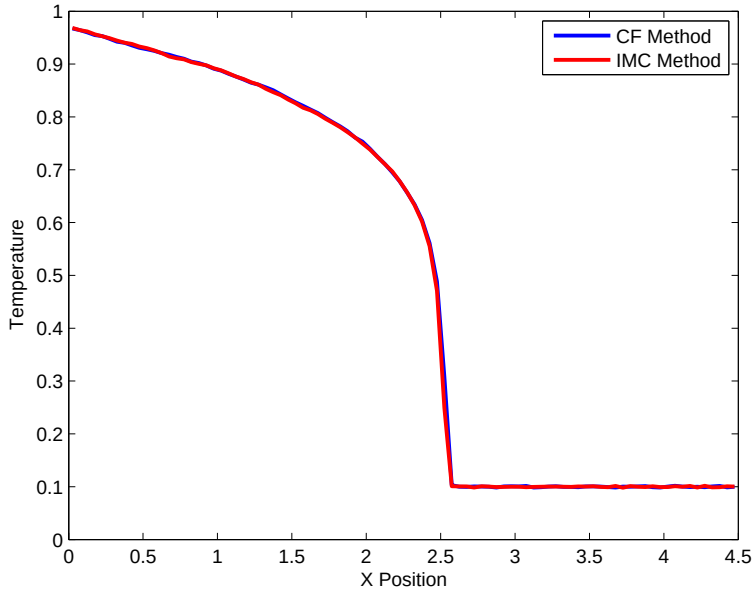

(a) Full marshak wave.

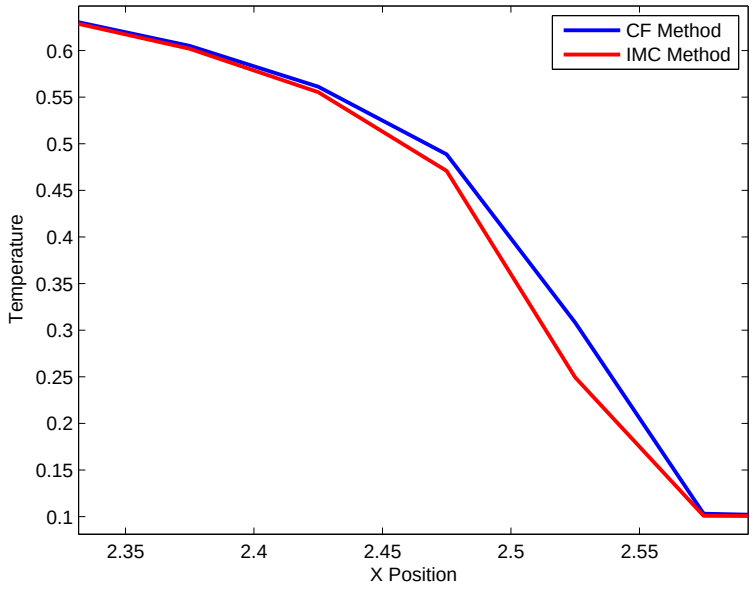

(b) Marshak wave front.

Figure 4.17: Marshak wave differences with IMC and CF method in the Nonlinear Problem.

become physical. Unphysical results in this context are results where the Maximum Principle (9) is violated. A Maximum Principle violation occurs when the temperature of the material exceeds the boundary temperature conditions, effectively making the temperature of the material hotter than the source of radiation heating it. The magnitude of the violations are dependent on the size of the spatial cell, the time step size and the total energy absorbed by that cell for a given time step. Figure 4.18 shows the nonlinear problem run with a large time step that yields unphysical results.

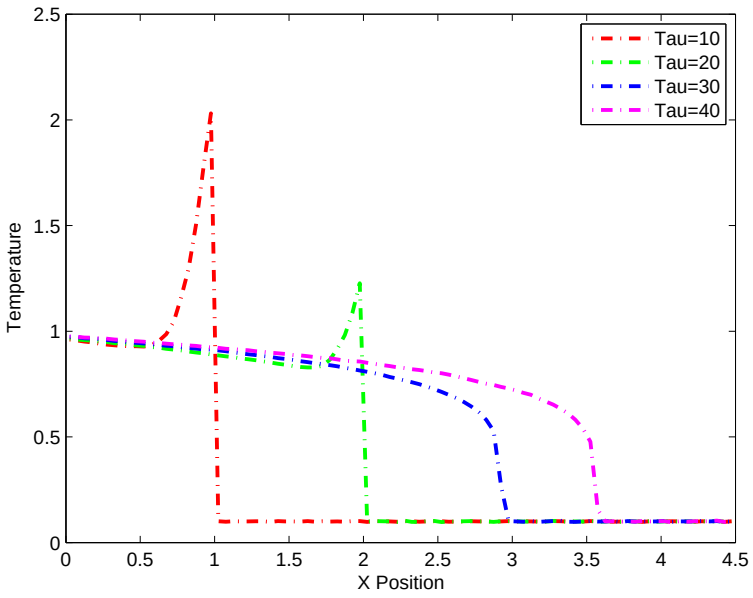

Figure 4.18: Violations of the Maximum Principle with $\Delta\tau = 0.5$ and $\Delta x = 0.05$ using IMC in the Nonlinear Problem.

In this simulation the material temperature exceeds the 1 keV temperature of the source which violates the maximum principle. Because the time step is so large, the opacity of the material is not updated during the time that the Marshak wave would naturally pass through the cell. Since the material is so opaque to begin with, the cell remains optically thick during the simulated time step; absorbing more photons than physically possible. These excessive absorptions cause the material temperature of the cell to spike and the cell becomes optically thin during the next time step. Then, the cool, opaque neighboring cell repeats the same process. This numerical artifact then propagates through the problem similar to a Marshak wave, decreasing the size of it's violation of the maximum principle as it progresses. The decrease in the violation magnitude occurs since the Marshak wave is slowing down, meaning less energy will

be absorbed by each successive cold cell. Applying the Wollaber-Larsen Temperature Predictor-Corrector (WLTPC), Fig. 4.19 shows that there is a significant improvement in the solution.

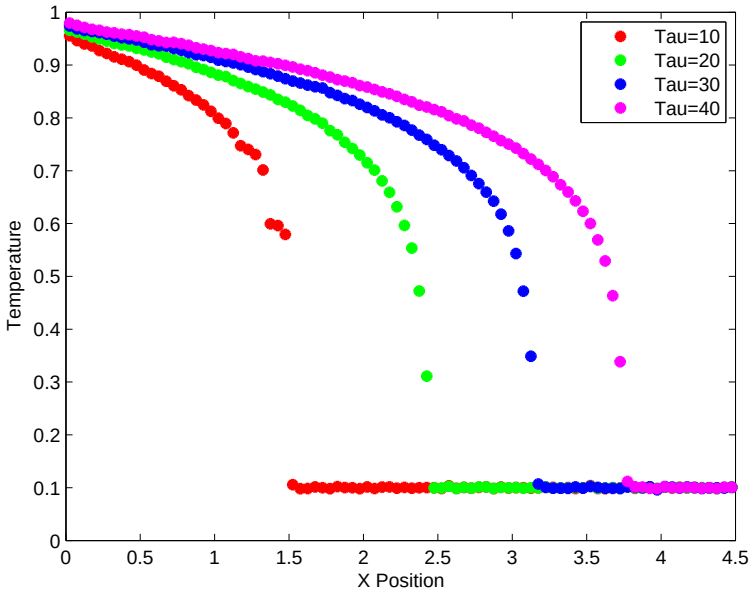

Figure 4.19: Violations of the Maximum Principle with $\Delta\tau = 0.5$ and $\Delta x = 0.05$ using IMC WLTPC in the Nonlinear Problem.

The WLTPC approach does not show the same violations of the maximum principle that are seen at $\tau = 10$ and $\tau = 20$ in the tradiational approach. However, at $\tau = 10$ the WLTPC shows a Marshak wave front that is not smooth. This is the only indication in the plot that a violation of the maximum principle has occurred. Since the time step sizes are so large for the given spatial width, the predictor step still violates the maximum principle at the beginning of the simulation. Since the predictor method violates the maximum principle, and therefore has a large temperature estimate / low opacity estimate, the corrector step allows for more radiation streaming through the once optically thick cells. This reduces the amount of photon energy that would be unnaturally absorbed in a single cell; reducing and dispersing the violation of the maximum principle over more cells. This process allows the simulated Marshak wave with large time steps to better approximate the actual Marshak wave speed. As in the 0D methods however, the predictor-corrector methods do not perfectly reconstruct the reference solution as shown in Fig. 4.20.

Figure 4.20 also shows that both the traditional approach and the WLTPC methods do not yield the reference solution even after the violations of the maximum principle

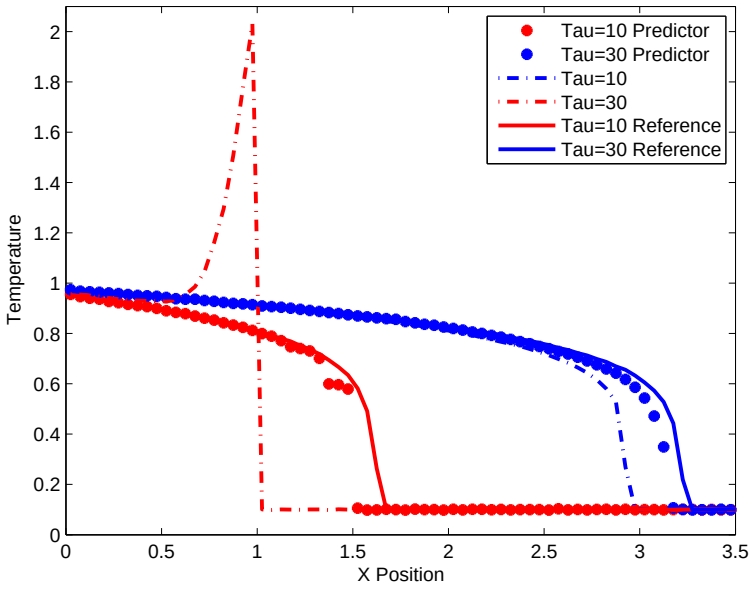

Figure 4.20: Comparison of the violations of the maximum principle compared to a reference solution in the Nonlinear Problem.

have been resolved. While the predictor-corrector solution is more accurate, it did not solve the problem that the time step size used was simply to large to resolve the nonlinearities within the problem. To better understand the differences between the two large time step approaches, the Marshak wave front velocity is plotted in Fig. 4.21.

The reference solution wave front slows down as it moves farther and farther away from the boundary source. The decrease in the speed is due to the dissipation of the strength of the source the farther into the slab that the front of the Marshak wave penetrates. Since each collision changes the direction of the particle isotropically and the left boundary has a vacuum condition, the aggregate effect is that the energy diffuses more slowly away from the source. The predictor-corrector wave speed using large time steps generally follows the reference solution yielding a much more accurate solution over the developement of the transient. However, both the traditional approach and the predictor-corrector do a poor job at resolving the beginning of simulation Marshak wave velocity. The traditional solution in fact maintains a constant velocity for the majority of the simulation time modeled here.

The violation of the maximum principle in the traditional approach travels at a constant rate since photons can not travel through a single artificially thick cell in one time step. Therefore, the violation of the maximum principle Marshak wave can

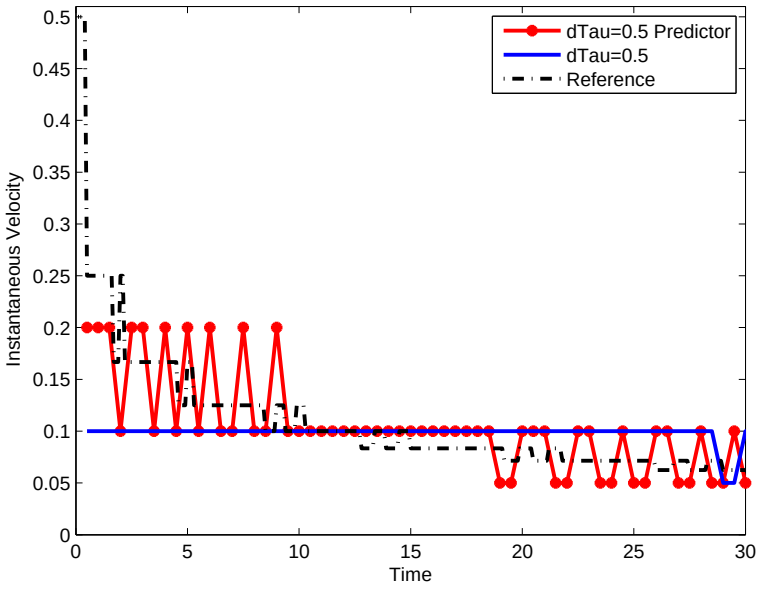

Figure 4.21: Instantaneous velocity of the Marshak wave front vs. time for $\Delta x = 0.05$ and $\Delta t = 0.5$ in the Nonlinear Problem.

only travel at the rate of $\frac{\Delta x}{\Delta t} = \frac{0.05}{0.5} = 0.1$ in this particular problem. The predicted Marshak wave velocity can be seen in Fig. 4.21. Even though the Marshak wave that violates the maximum principle travels slower than the reference solution at the beginning of the simulation, the reference solution slows down dramatically allowing the unphysical Marshak wave to close the distance. In this problem, Marshak waves that violate the maximum principle eventually disipate, making them look like normal Marshak waves at a later time. Therefore, great care must be made to ensure that the problem develops physically over the course of the simulation for both the traditional approach and with predictor-correctors to accurately resolve the Marshak wave at a later time.

To compare the accuracy of the Carter-Forrest and Implicit Monte Carlo method, different values of time step sizes and spatial discritization widths are compared on the same problem. A reference solution for the given spatial discritization width is used at time $\tau = 20$ to compare the different methods. Eighty million source particles are used to model the 1D nonlinear problem and the time steps are chosen such that the largest time step size will violate the maximum principle and the smallest time step size has the solution start to be dominated by Monte Carlo noise. Tables 4.1 and 4.2 contain the averaged relative errors of the difference between the simulation and reference solutions for each given spatial width. The averaged relative error is defined

as

$$R_{avg}(t) = \frac{1}{N}\sum_{i}^{N} \frac{\mid T_r^i(t) - T_c^i(t) \mid}{T_r^i(t)} \tag{4.31}$$

where $T_r^i(t)$ represents the reference solution at time t in cell i, $T_c^i(t)$ represents the simulated solution of interested at time t in cell i and N is the number of cells examined in the marhsak wave. For each given time step and spatial width combination, the

Table 4.1: Traditional IMC averaged relative error in temperature from reference solution for each spatial width.

$\Delta\tau\backslash\Delta x$	0.025	0.05	0.1
0.01	0.00161	0.00196	0.00171
0.02	0.00327	0.00375	0.00360
0.04	0.00623	0.00721	0.00679
0.05	0.00730	0.00852	0.00841
0.08	0.01162	0.01269	0.01265
0.1	0.01507	0.01495	0.01527

Table 4.2: Traditional CF averaged relative error in temperature from reference solution for each spatial width.

$\Delta\tau\backslash\Delta x$	0.025	0.05	0.1
0.01	0.00081	0.00094	0.00082
0.02	0.00205	0.00218	0.00194
0.04	0.00377	0.00422	0.00386
0.05	0.00460	0.00530	0.00489
0.08	0.00707	0.00796	0.00738
0.1	0.01026	0.00937	0.00905

CF method is more accurate than the IMC method for the same reference solution. Because of the IMC bias, the CF method more accurately models the transients that occur at the Marshak wave front even though both methods are $O(\Delta t)$. As the time step size is decreased for both methods, their solutions at a given time converge to the same answer.

Predictor-corrector methods with IMC and CF are now explored using the same time step size and spatial widths, in Tables 4.3 and 4.4. As expected, the predictor-

Table 4.3: IMC WLTPC averaged relative error in temperature from reference solution for each spatial width.

$\Delta\tau\backslash\Delta x$	0.025	0.05	0.1
0.01	0.00097	0.00169	0.00169
0.02	0.00226	0.00328	0.00299
0.04	0.00481	0.00568	0.00587
0.05	0.00583	0.00693	0.00729
0.08	0.00892	0.01047	0.01122
0.1	0.01093	0.01257	0.01353

Table 4.4: CF WLTPC averaged relative error in temperature from reference solution for each spatial width

$\Delta\tau\backslash\Delta x$	0.025	0.05	0.1
0.01	0.00039	0.00058	0.00053
0.02	0.00107	0.00127	0.00144
0.04	0.00227	0.00276	0.00296
0.05	0.00280	0.00366	0.00366
0.08	0.00437	0.00507	0.00583
0.1	0.00556	0.00651	0.00692

corrector methods give a more accurate solution in all cases. This increase in accuracy comes from resolving the nonlinearities in $\sigma(t)$ in a more accurate manner. However, this improved estimate of the value of $\sigma(t)$ during a time step comes at the cost of running a time step twice; a costly proposal. To reduce the overall computation

cost, the Variable Weight Predictor-Corrector (VWPC) scheme introduced in Chapter 3 is used. The predictor method uses fewer particle packets to model the photon transport in the problem to get a less accurate look at the end-of-time-step value of the temperatures. This estimate of the temperature field will then be used in the corrector step to modify the opacities during the corrector time step.

To determine the best down sampling value for the VWPC, a parameter study is conducted on the nonlinear problem using $\Delta\tau = 0.01$, $\Delta\tau = 0.02$, $\Delta\tau = 0.04$, $\Delta\tau = 0.05$, $\Delta\tau = 0.08$, and $\Delta\tau = 0.1$ with $\Delta x = 0.025$ and 80 million source particles. The relative error of the temperature is compared at time $\tau = 20$ for different down sampling values for the WLTPC method to determine the fastest and most accurate solution. Figure 4.22 shows that there is a surprising amount of flexibility in the choice of a down sampling value. The down sampled values from 10 to 10000

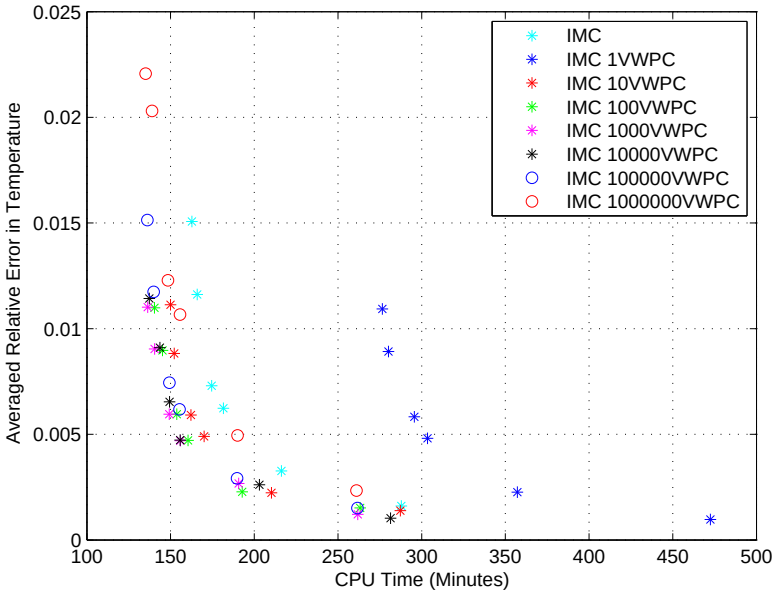

Figure 4.22: Relative error vs. computation time for different down sampled VWPC's using WLTPC in the Nonlinear Problem. For each color / symbol combination plot, the highest relative error and lowest CPU time point represents $\Delta\tau = 0.1$ and the smallest relative error and highest CPU time point represents $\Delta\tau = 0.01$.

require about the same computation time to yield a similarly accurate result using the WLTPC. When the down sample value reaches $100,000$, there is the first clear indication that the accuracy of the VWPC method is breaking down. When using the 100000VWPC WLTPC, the accuracy of the predictor-corrector scheme is comperable to the traditional implementation of the IMC method. Finally, at a down sample value of $1,000,000$ the VWPC approach has less accurate results than the tradiational

IMC approach. Due to this information, the down sample value of 100 has been chosen since it is competative in both accuracy and computation time with the other VWPC down sample values. Also, it represents that the predictor step will use 1% of the particles that would be simulated in the corrector step. While using 1% of the corrector particles in the predictor step may not be ideal for all problems, it will be used as the standard choice for the down sampling value for the remainder of this thesis.

Tables 4.5 and 4.6 show the results from using a 100 Variable Weight Predictor-Corrector (100VWPC) with the WLPC. While the VWPC are not as accurate as

Table 4.5: IMC with 100VWPC averaged relative error in temperature from reference solution for each spatial width.

$\Delta\tau\backslash\Delta x$	0.025	0.05	0.1
0.01	0.00152	0.00183	0.00152
0.02	0.00228	0.00299	0.00319
0.04	0.00471	0.00584	0.00603
0.05	0.00595	0.00710	0.00746
0.08	0.00897	0.01050	0.01117
0.1	0.01099	0.01255	0.01353

Table 4.6: CF with 100VWPC averaged relative error in temperature from reference solution for each spatial width.

$\Delta\tau\backslash\Delta x$	0.025	0.05	0.1
0.01	0.00048	0.00060	0.00056
0.02	0.00097	0.00122	0.00148
0.04	0.00213	0.00307	0.00279
0.05	0.00282	0.00343	0.00353
0.08	0.00440	0.00515	0.00581
0.1	0.00581	0.00622	0.00689

running the predictor-corrector without down sampling particles, they are much faster. Also, the VWPC are significantly more accurate than the traditional IMC and CF methods. To determine the cost / gain of these methods, the averaged relative error is plotted against the cpu time used to calculated the solutions for the spatial width $dx = 0.025$ in Figs. 4.23a and 4.23b.

The largest relative error point in each line in each graph represents the largest time step size used. The most accurate solutions that take longer to run represent the smallest time step used to resolve the solution. In both the IMC and CF method the predictor-corrector methods shows an improvement in the accuracy of the solution at the cost of a longer run time. However, the VWPC methods show competitive run times with the traditional methods while still showing a meaningful decrease in error. In the case of the IMC implementation the 100 VWPC runs more accurately and in a shorter time than the traditional implementation. This result is unexpected and is not anticipated to be repeated in other problems.

It is worthwhile to mention that the research code used for these timing tests is not a industry quality code, and lacks a large number of tallies and other functionality that may in fact dominate the run times of these solutions. So while these timing results

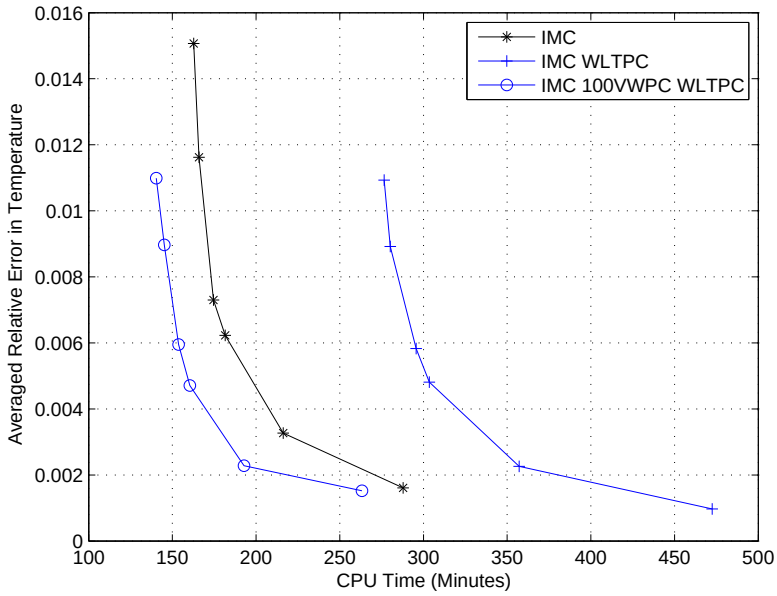

(a) IMC relative error vs. time.

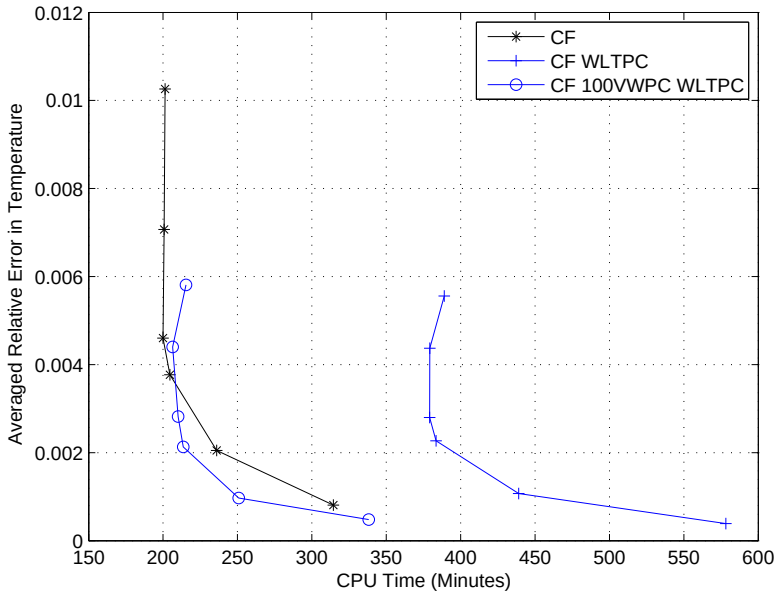

(b) CF relative error vs. time.

Figure 4.23: Relative error vs. time for the spatial width $dx = 0.025$ for the IMC and CF method using the data from Tables 4.1 to 4.6. For each color / symbol combination plot, the highest relative error and lowest CPU time point represents $\Delta\tau = 0.1$ and the smallest relative error and highest CPU time point represents $\Delta\tau = 0.01$.

are interesting, they are by no means reliable to project the effects on computation time in other radiation transport codes.

Next, the Opacity Averaged Predictor-Corrector (OAPC) is implemented to compare to the WLTPC. Surprisingly, the OAPC did not prove to be an improvement in the 1D results as they did in the 0D results. Figures 4.24a and 4.24b both show that for large time step sizes the relative error for the OAPC is surprisingly large. In fact, it it sufficiently worse than the traditional implementation of the IMC and CF approximations. As the time step size decreases, the OAPC approaches the same accuracy as the traditional implementation. The significant differences between the 0D and 1D OAPC results is due to leakage. In the 0D results, radiation could not leak out of a cell and eventually would come to an equilibrium but with a different transient as seen using the WLTPC in Fig. 3.14.

With the 1D problems, spatial leakage starts to play a significant role in the accuracy of the solution. In the OAPC, the values of the opacity during the corrector step end up higher than the opacities using the WLTPC. For example, if the temperature starts at $T_n = 0.1$ and ends at $T_{n+1} = 0.9$ than the Wollaber temperature estimate would give the answer that $T_{n+\frac{1}{2}} = 0.253$ and would give an opacity of $\sigma_{n+\frac{1}{2}} = 61.75$. In contrast the opacity averaging would give an opacity of $\sigma_{n+\frac{1}{2}} = 500.69$. The two predictor-corrector methods give very different estimates of the opacity to be used during the corrector step. For particularly large time steps, this means that the OAPC will maintain a larger opacity for longer than the WLTPC. The larger opacity can cause spikes in the temperature distribution similar to violations of the maximum principle as seen in Fig. 4.25. The Marshak wave progresses more slowly when large time steps are used since the overall opacity is much larger. Therefore, the OAPC does not demonstrate itself to be a robust scheme. However, other predictor-corrector methods can be used besides the WLTPC and OAPC. In the following section, a predictor-corrector scheme will be examined that allows for the change of the opacities during a time step.

4.2.1 Time Dependent Opacity Estimations During a Time Step

Instead of using a predictor-corrector method to find a new constant value of the opacity for the corrector step, a time dependent opacity can be formulated for the corrector step. By knowing the end of time step value of the opacities, a linear interpolation of the beginning and end of time step values of the opacities can be used to change

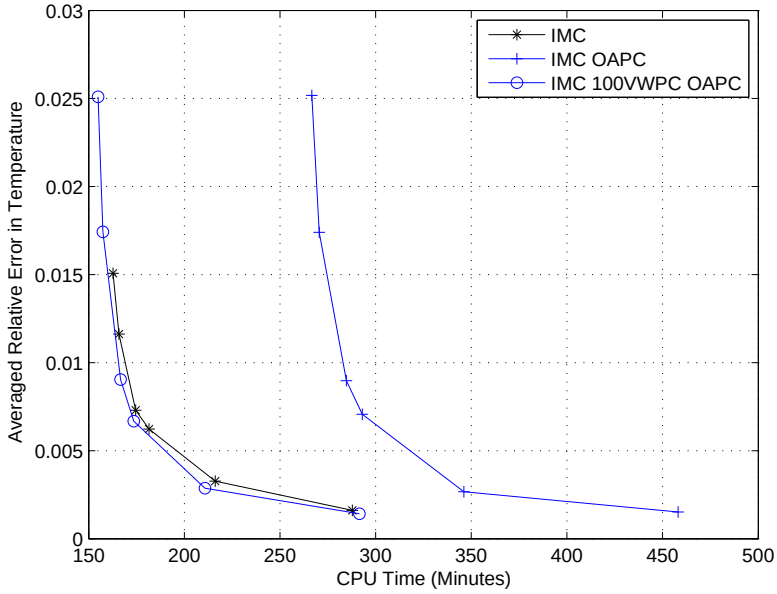

(a) IMC relative error vs. time.

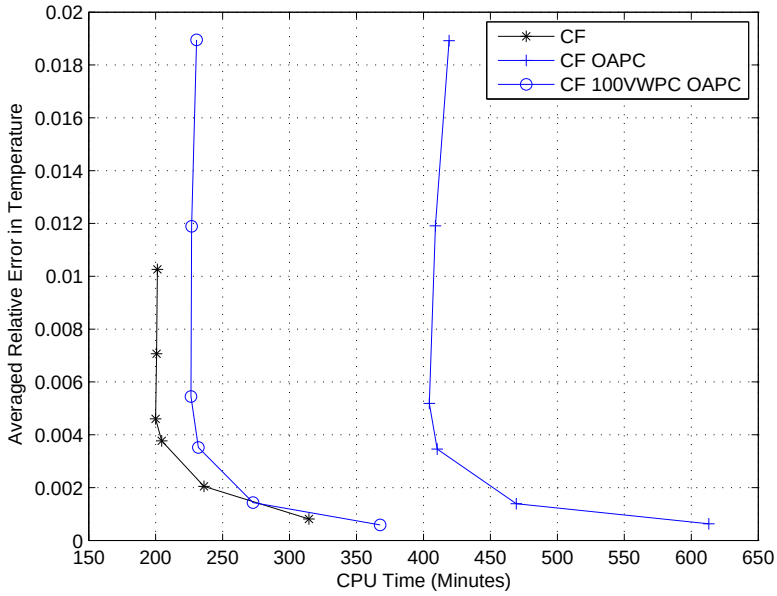

(b) CF relative error vs. time.

Figure 4.24: Relative error vs. time for the spatial width $dx = 0.025$ for the IMC and CF method with averaged opacity predictor-corrector. For each color / symbol combination plot, the highest relative error and lowest CPU time point represents $\Delta\tau = 0.1$ and the smallest relative error and highest CPU time point represents $\Delta\tau = 0.01$.

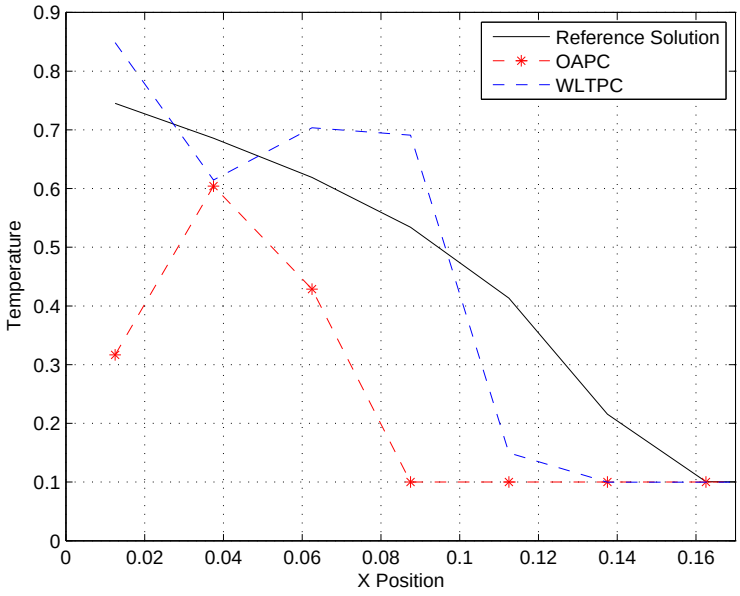

Figure 4.25: Marshak wave front at time $\tau = 0.3$ using $\Delta\tau = 0.1$ with a $\Delta x = 0.025$.

the opacities of a material cell during a time step. A couple of different methods have been proposed to solve for the transport distance in a media with continuously varying cross-sections including substepping and delta-tracking. While delta-tracking is efficient when the cross-section change is small, it becomes increasingly less efficient with rapid changes of the cross-section within a region. Instead of using a rejection method to determine particle transport distance, a direct sampling method has been proposed by Brown and Martin (2; 3). The direct sampling technique will be used since it is more efficient in regions with large changes in opacity than the delta tracking method.

To sample the photon transport distance from a region with continuously changing opacities, it is necessary to first determine the way that the opacities change during a time step. For this thesis, it is assumed that the change of opacities can be described as linear function between the start of time step opacities and end of time step opacities estimated by a predictor step. The current opacity at any given time t is therefore defined as

$$\sigma_c = \frac{\sigma_{n+1} - \sigma_n}{\Delta t} t_c + \sigma_n. \tag{4.32}$$

Using the current opacity $\sigma_c(t_c)$ at the starting time t_c of particle and the predicted opacity σ_{n+1}, a linear interpolation is used to construct the time dependent opacity in

a time step as

$$\sigma(t) = \left[\frac{\sigma_{n+1} - \sigma_c}{\Delta t - t_c}\right] t + \sigma_c \tag{4.33}$$

where t is bounded as $0 \leq t \leq \Delta t - t_c$. The $\Delta t - t_c$ term represents the time left before the end of time step census. The time dependent opacity is converted to a spatially dependent opacity by rearranging the equations as

$$\sigma(x) = \frac{\sigma_{n+1} - \sigma_c}{x_{max}} x + \sigma_c \tag{4.34}$$

where $x_{max} = c(\Delta t - t_c)$, $0 \leq x \leq x_{max}$ and $x = ct$. Effectively, the photon is exposed to a spatially changing media during an arbitrary flight path. While this process is straight forward in an analog Monte Caro simulation, it becomes more challenging in a non-analog simulation.

To determine the flight distance of a photon in a spatially changing media with non-analog transport, the probability of interaction must first be determined. The probability that a photon has a collision in $[0, x_{max}]$ is defined as

$$P_c = \int_0^{x_{max}} \sigma_s(x) e^{-\int_0^x \sigma_s(x')dx'} dx. \tag{4.35}$$

To solve Eq. (4.35) in a general way, the integral is rewritten using a change of variables. Substituting the transformation

$$y(x) = \int_0^x \sigma(x')dx', \tag{4.36}$$

which gives the relationship

$$dy(x) = \sigma(x)dx, \tag{4.37}$$

into Eq. (4.35) yields the general solution

$$\begin{aligned} \int_0^x \sigma_s(x) e^{-\int_0^x \sigma_s(x')dx'} dx &= \int_0^{y(x)} e^{-y(x)} dy \\ &= 1 - e^{-y(x)}. \end{aligned} \tag{4.38}$$

Therefore any arbitrary spatially dependent opacity can be used in this format to determine the interaction probability. The interaction probability P_c can now be defined using (4.38) as

$$P_c = 1 - e^{-y(x_{max})} \tag{4.39}$$

where

$$y(x_{max}) = \int_0^{x_{max}} \sigma_s(x)dx. \tag{4.40}$$

Now that that total probability of collision within a given domain is determined, the probability distribution function (pdf) for flight distances can be examined. The pdf of the flight distance of a particle that has collided within $0 \leq x \leq x_{max}$ is defined as

$$f(x) = \frac{1}{P_c}\sigma_s(x)e^{-\int_0^x \sigma_s(x')dx'}dx. \tag{4.41}$$

Integrating (4.41) over the domain will give the cumulative distribution function (cdf)

$$\xi = F(x) = \frac{1}{P_c}\int_0^x \sigma_x(x')e^{-\int_0^{x'} \sigma_s(x'')dx''}dx' \tag{4.42}$$

where ξ is a uniform random deviate and the value of x that satisfies the integral is the distance traveled by the particle. Using Eq. (4.38) and rearranging the cdf, the general sampling form of the cdf is given as

$$y(x) = -\ln(1 - \xi P_c). \tag{4.43}$$

In summary, the distance sampling procedure is implemented as:

1. If: $\xi_1 \leq P_c$,
   Sample $y(x) = -\ln(1 - \xi_2 P_c)$
   Solve the equation for the value of x
2. Else: the photon did not collide and it reaches census.

After the particle distance traveled has been established, either through distance to census or distance to collision before the census, the photons energy (E) is attenuated in the medium as

$$E' = E\exp\left[-\int_0^s [\sigma_t(x) - \sigma_s(x)]\right] \tag{4.44}$$

so the particle has an energy E' after traveling and deposits $E - E'$ energy into the cell.

To solve for a transcendental function of $y(x)$ in terms of x, a root solving technique must be used. In general, a Newton iteration scheme was seen to converge within 10^{-6} of the solution within $1 - 3$ iterations (3). By using a direct sampling technique, Brown and Martin's work resulted in a good implementation of the non-analog CF method. Their work will now be extended to incorporate a new time dependency in the opacities for the CF method and to introduce a time dependency in the opacities for the IMC method.

4.2.2 IMC Time Dependent Opacity Predictor-Correctors

The effective scattering cross-section for the IMC method is defined as

$$\sigma_s(t) = (1 - f)\sigma_t(t) \tag{4.45}$$

where f is the Fleck factor, $\sigma_t(t)$ is the total cross-section and the value of t is considered constant for a cell during a time step. Since the opacities remain constant during a time step, the analog implementation is very straight forward. However, the non-analog approach is desired since it is an accepted variance reduction technique that is standard in Monte Carlo TRT codes. The traditional non-analog IMC implementation is also fairly straight forward. Since there is no time dependency in non-analog IMC opacities, the distance the particle would travel in an infinite medium can be used, or $P_c = 1$. The distance the particle actually travels however can be truncated by the distance to census or distance to another cell boundary. This implementation does not introduce errors, and the distance traveled is then sampled as

$$s = -\ln(\xi)/\sigma_s \tag{4.46}$$

and the particle energy is attenuated by

$$E^{'} = E(1 - e^{-f\sigma s}). \tag{4.47}$$

Implementing a linearly time dependent opacity created by the predictor step adds a significant level of complexity to the non-analog IMC sampling routine. Rewriting Eq. (4.34) and the Fleck factor in a more condensed form gives

$$\sigma(x) = ax + b \tag{4.48}$$

and

$$f(x) = 1/(1 + M\sigma(x)) \tag{4.49}$$

where $a = \frac{\sigma_{n+1}-\sigma_c}{x_{max}}$, $b = \sigma_c$, and $M = \alpha\beta_n c\Delta t$. Now, compute the function $y(x)$ as

$$\begin{aligned} y(x) &= \int_0^x \sigma_s(x^{'})dx^{'} \\ &= \int_0^x [\sigma(x^{'})(1-f(x^{'}))]dx^{'} \\ &= bx + \frac{ax^2}{2} + \frac{-aMx - \log[1+bM] + \log[1+bM+aMx]}{aM^2}. \end{aligned} \tag{4.50}$$

While the value of P_c can now be directly calculated using Eq. (4.39), the pdf created for the sampling of the flight distance is now a transcendental function of x. To solve for x, a root finding method must be employed. For this case, a Newton iteration is a robust scheme to solve for the transport distance as was the case with the non-analog CF method discussed earlier.

Using the accuracy versus timing tests used previously in Tables 4.1 to 4.6, the IMC Time Dependent Opacity Predictor-Corrector (TDOPC), with and without a VWPC, can be examined at the time step sizes of 0.1, 0.08, 0.05, 0.04, 0.02, and 0.01 at the time $\tau = 20$. Figure 4.26 shows that for large time steps the TDOPC are more accurate

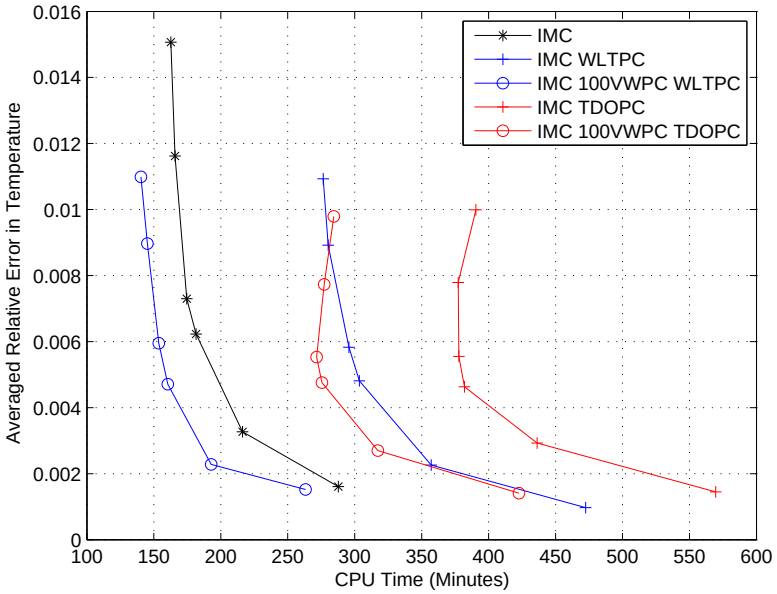

Figure 4.26: IMC relative error vs. time for different predictors in the Nonlinear Problem. For each color / symbol combination plot, the highest relative error and lowest CPU time point represents $\Delta\tau = 0.1$ and the smallest relative error and highest CPU time point represents $\Delta\tau = 0.01$.

than the WLTPC. However, this accuracy comes at an increased computational cost

making this predictor-corrector much more costly. Even when using the 100 VWPC, the run times are nearly double the traditional IMC run times for the same accuracy. To decrease the computational cost of the TDOPC, a simplification is made to remove the root solving procedure needed to sample the flight distance.

Instead of assuming that the opacities change during a photons flight path, they are fixed at a given time similar to the traditional lagging used to linearize the TRT equations. The key difference is that whenever the particle must sample the distance to the next collision, the current opacity $\sigma_c(t)$ is used. Therefore, a particle will be transported in a non-analog manner starting at time $t^{'}$ with an opacity $\sigma_c(t^{'})$ and interact at time $t^{''}$. Then the particle will travel starting at time $t^{''}$ with an opacity $\sigma_c(t^{''})$ where $t_n \leq t^{'} \leq t^{''} \leq t_{n+1}$ By keeping the opacity constant during a single flight distance and updating the opacity for the next flight distance within a step, the root solving algorithm is no longer required. Figure 4.27 shows that the Constant Emission

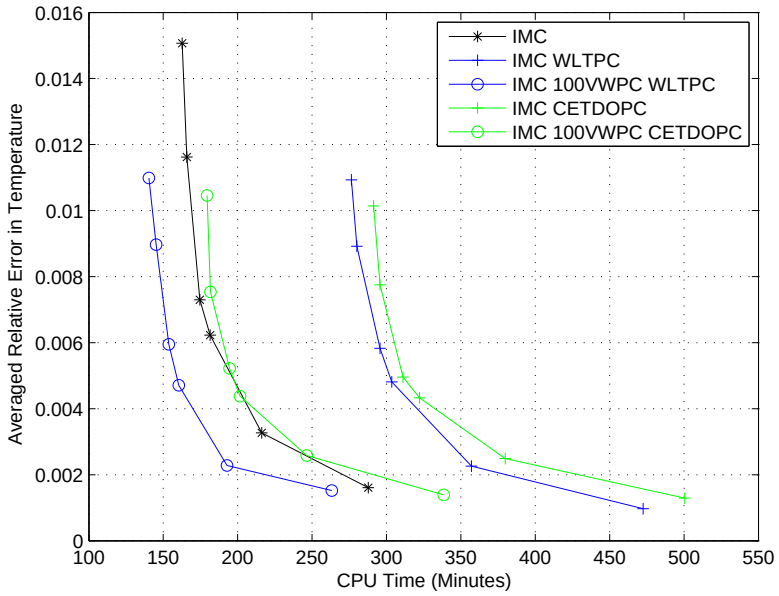

Figure 4.27: IMC relative error vs. Constant Emission Time Dependent Opacities in the Nonlinear Problem. For each color / symbol combination plot, the highest relative error and lowest CPU time point represents $\Delta\tau = 0.1$ and the smallest relative error and highest CPU time point represents $\Delta\tau = 0.01$.

Time Dependent Opacity Predictor-Corrector (CETDOPC) is significantly faster than the TDOPC. Also, compared to the standard IMC implementation the CETDOPC is more accurate for each corresponding time step size. When using the 100 VWPC CETDOPC there is not a significant increase in computation time for a more accurate solution.

Figure 4.28 shows the comparison between the two different time dependent opacity predictor-correctors. Surprisingly, the CETDOPC does not lose accuracy for the gains

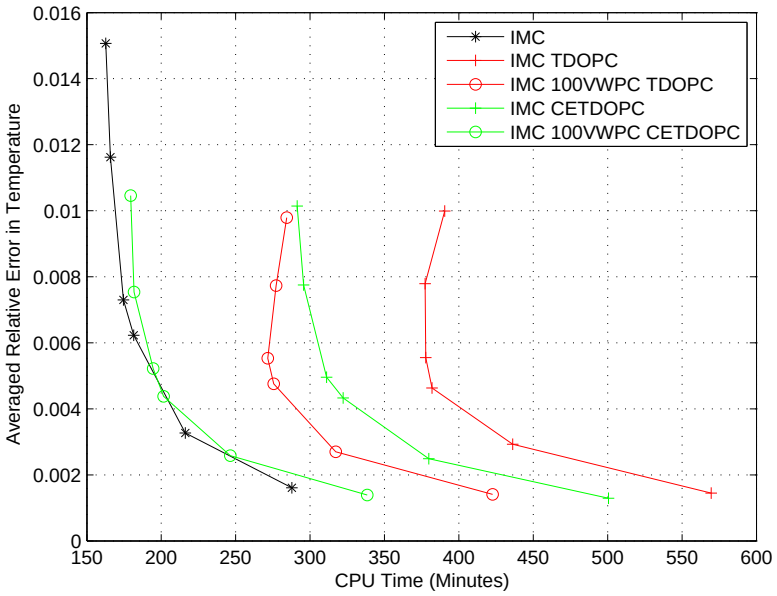

Figure 4.28: IMC relative error vs. CETDOPC and TDOPC in the Nonlinear Problem. For each color / symbol combination plot, the highest relative error and lowest CPU time point represents $\Delta\tau = 0.1$ and the smallest relative error and highest CPU time point represents $\Delta\tau = 0.01$.

in speed over the TDOPC; making it an attractive method. Also, there is no a priori knowledge of the underlying opacity temperature dependency as is required in the WLTPC, allowing the method to be more generally applicable to a host of arbitrary opacity models.

4.2.3 CF Time Dependent Opacity Predictor-Correctors

Non-analog transport with the CF method requires a root solving algorithm for the flight distance of a particle. Using more exponentials and logarithms than the non-analog IMC method, the non-analog CF method is computationally more intensive. However, the increased cost is partially offset by the improvements in the accuracy of the solution by the removal of bias that has been seen in the IMC method.

The effective scattering for the CF method is given as

$$\sigma_s(t) = \sigma(t)\left[1 - e^{-\beta c\sigma(t_{n+1}-t)}\right]. \tag{4.51}$$

Changing the effective scattering opacity from a function of time to a function of position yields

$$\sigma_s(x) = \sigma\left[1 - \gamma e^{px}\right] \tag{4.52}$$

where $\gamma = e^{-ph}$, $p = \beta\sigma$, $h = c(t_{n+1} - t^{'})$, $t^{'}$ is the current time, and $0 \leq x \leq h$. Following the previous procedure, the function $y(x)$ can now be defined as

$$\begin{aligned} y(x) &= \int_0^x \sigma_s(x^{'})dx^{'} \\ &= \int_0^x \sigma[1 - \gamma e^{px}]dx^{'} \\ &= \sigma x + \frac{\sigma\gamma}{p}(e^{px} - 1). \end{aligned} \tag{4.53}$$

After sampling the flight distance via a root finding method for this transcendental function of x, the photon energy is reduced after traveling a distance s by

$$\begin{aligned} E^{'} &= Eexp\left[-\int_0^s [\sigma - \sigma_s(x)]dx\right] \\ &= E\exp\left[-\gamma(e^{ps} - 1)/\beta\right]. \end{aligned} \tag{4.54}$$

Therefore, $E - E^{'}$ energy is deposited into the material where the track length occurred (3).

To create a CF Time Dependent Opacity Predictor-Corrector, the opacities must now change with regard to time in the effective scattering term. Using the simplified form of a linearly changing opacity shown in Eq. (4.48), Eq. (4.52) is rewritten as

$$\begin{aligned} \sigma_s(x,t) &= [ax + b]\left[1 - e^{-c\beta(t_{n+1} - t)[ax+b]}\right] \\ &= [ax + b]\left[1 - e^{-c\beta(t_{n+1} - t^{'} - t + t^{'})[ax+b]}\right] \\ \sigma_s(x) &= [ax + b]\left[1 - e^{-\beta(x_{max} - x)[ax+b]}\right] \end{aligned} \tag{4.55}$$

where $x_{max} = c(t_{n+1} - t^{'})$, $x = c(t - t^{'})$, $t^{'}$ represents the starting time of the particle and t represents the time the particle finished traveling to the next interaction. Now that $\sigma_s(x)$ has been determined, the function $y(x)$ can be determined as

$$
\begin{aligned}
y(x) &= \int_0^x \sigma_s(x^{'})dx^{'} \qquad (4.56)\\
&= [ax+b]\left[1-e^{-\beta(x_{max}-x)[ax+b]}\right]\\
&= \frac{1}{4}\Bigg[\frac{2(e^{-b\beta x_{max}}-e^{-\beta(x_{max}-x)(b+ax)})}{\beta}+2x(2b+ax)\\
&+\frac{(b+ax_{max})\exp[\frac{-\beta(b+ax_{max})^2}{4a}]\sqrt{\pi}\left(\mathrm{Erfi}[\frac{\sqrt{\beta}(b-ax_{max})}{2\sqrt{a}}]-\mathrm{Erfi}[\frac{\sqrt{\beta}(b-ax_{max}+2ax)}{2\sqrt{a}}]\right)}{\sqrt{a}\sqrt{\beta}}\Bigg].
\end{aligned}
$$

A new function Erfi is introduced in Eq. (4.56) and is defined as

$$
\mathrm{Erfi}(z) = \frac{\mathrm{Erf}(iz)}{i} \qquad (4.57)
$$

where $i = \sqrt{-1}$ and Erf is the error function.

The inclusion of the Erfi function dramatically complicates the root finding process and significantly increasing computation time to assure necessary precision in the solution to the function. For this reason, the TDOPC method will not be examined with the CF method. Instead, the CETDOPC will be implemented with the expectation that the CETDOPC and the TDOPC approaches will be as similar in the CF approach as they were in the IMC approach.

Figure 4.29 shows the CF CETDOPC approach compared to the traditional and CF WLTPC implementation. Unlike the results shown when using the IMC method in Fig. 4.27, the CETDOPC approach shows a point for point higher relative error than the WLTPC. However, the CF CETDOPC approach is still more accurate than the traditional CF approach and more accurate than either of the IMC predictor-corrector schemes.

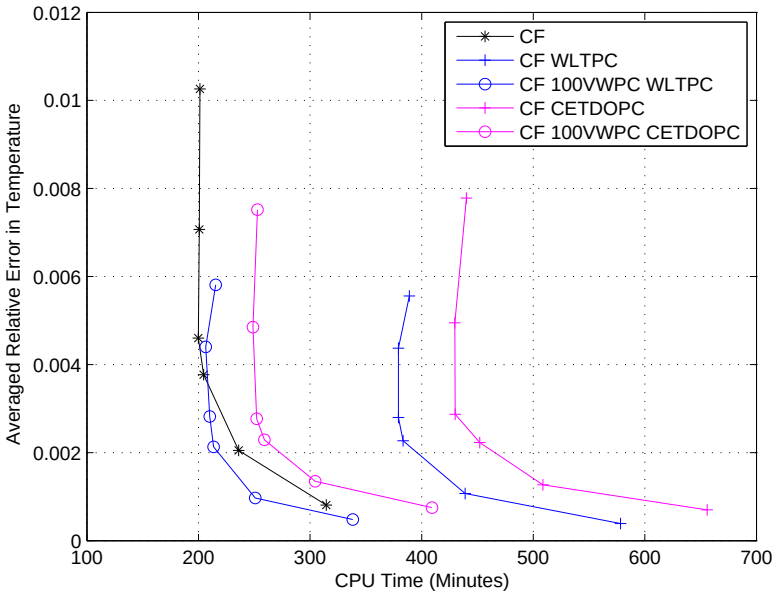

Figure 4.29: CF relative error vs. Constant Time Dependent Opacities in the Nonlinear Problem. For each color / symbol combination plot, the highest relative error and lowest CPU time point represents $\Delta\tau = 0.1$ and the smallest relative error and highest CPU time point represents $\Delta\tau = 0.01$.

Chapter 5

Time Step Controllers

Resolving the nonlinearity in $\sigma(t)$ is a significant factor affecting the accuracy of both the IMC and CF methods in a nonlinear problem. For that reason, great care must be taken to ensure that a time step size used in the calculation is small enough to yield a good estimate of the opacities to perform accurate transport. On the flip side, the smaller the time step used, the more costly the simulation required to solve for a solution at some time τ. To resolve these discrepancies, time step controllers are used to change the size of the time step from one transport cycle to the next to achieve the largest time step possible while maintaining accurate transport. Time step controllers achieve this goal by using constraints that will determine the size of the next time step.

5.1 General Description of Time Step Controller Algorithm

A flow chart detailing the time step controller algorithm can be seen in Fig. 5.1. The first step is to run a time step to get the end of time step values for the simulation. These end of time step values are examined using the time step controller constraint(s). These constraints can be a number of different heuristics, but in this thesis the constraints will be limited to the relative changes of a given parameter like temperature or opacity. If the time step controller constraints are met in every cell within the problem, then the results of that time step are recorded and a new time step size is selected. However, if the violations of the time step controller constraints are considered too large, the time step might be rerun using a smaller Δt for time step n. The decision to rerun a time step should not be made lightly, but for severe

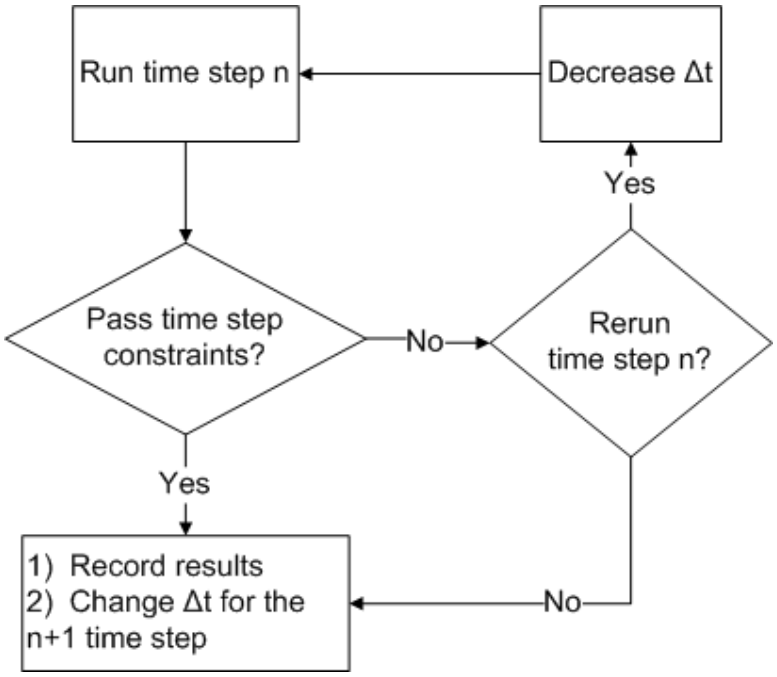

Figure 5.1: Time step controller generalized algorithm.

violations of the time step controller constraint rerunning a time step at time t_n may be the only way to have confidence in the solution.

The constraints in a time step controller represents the mechanism by which we try to determine and control the propagation of error. Whether the constraint was violated and how large the violation was will determine how the next time step size is selected. If the constraint is violated and the problem is not rerun, a smaller Δt will be chosen for the $n+1$ time step. Conversely, if the constraint is not violated, the size of Δt may be increased for the $n+1$ time step. In this way the value of Δt will change throughout a simulation. The methods by which we constrain the time step controller and how we change the time step size due to this information are the implementation details of a time step controller. Care must be taken when making the implementation decisions since any time step controller with an arbitrary constraint and slowly varying Δt selection might have the appearance of merit while still being far from the most optimal solution.

5.2 Photon Energy Density and Opacity Time Step Controllers in Zero-D

For a deterministic radiative transfer code, the maximum relative change of the energy in the photon field has been used as a heuristic for the time step controller constraint (8; 18). By restricting the change of the photon energy density, the change of the material energy density within a time step is also controlled. Therefore, if the photon field is correctly modeled, then effects like the warming at the Marshak wave front could be accurately resolved from one time step to another. Knoll's time step controller constraint for the change of the photon energy density is given as

$$\frac{\Delta E}{E} = \max_i \left[\frac{\mid E_i^{n+1} - E_i^n \mid}{E_i^{n+1} + E_{floor}} \right] = \eta^n \tag{5.1}$$

where i refers to the cell index, and n refers to the time step. E_{floor} is a "prescribed constant usually set equal to a multiple of the lower bound for the energy in a given problem". A new time step size is then calculated as

$$\Delta t_{new} = \Delta t_{old} \left(\frac{\eta_{target}}{\eta^n} \right)^{0.5} \tag{5.2}$$

where η_{target} is a user defined parameter for acceptable relative change usually chosen between 0.05 and 0.20. If the value of η is larger than η_{target}, then the size of the time step is decreased. Conversely if the value of η is less than η_{target} then the time step size is increased. The square root of the ratio of the target and actual values of η is used to smooth the change in the size of the time step. By throttling the relative change of energy in the photon field, the user will be able to control the rate at which the radiation field cools or heats to ensure proper transport. By controlling the rate at which energy from the photon field is absorbed or leaked by the material field, the rate of heating or cooling of the material can be controlled. Though not discussed by Knoll or Rider, the photon energy density controller is not general since the heat capacity of the material will directly effect the temperature change of the material for a given energy deposition. This temperature change will in turn effect the change of the opacity during a time step. However, the photon energy density controller has a very circuitous route of controlling the change in the opacity or temperature since the heat capacity can be different for different materials in the problem.

While examining the relative change of energy in the photon field with a tight constraint will resolve the nonlinearities in $\sigma(t)$, it does not directly focus on the

change in $\sigma(t)$ during a time step. This may seem to be a small point but it has fairly significant implications. The relative change in photon energy does not have significant importance in a Su-Olsen problem, but it does have a profound effect in a problem with an opacity with a $1/T$ dependency or even more, a $1/T^3$ dependency. The value of η_{target} may be set to a smaller value to better capture these nonlinearities, but this is an indirect approach to the issue. Putting a constraint on the relative change of photon energy says nothing about the relative change of the opacities. In fact, in order to perform accurate transport during a time step, the relative change of the opacity can not be too large. Also, the detailed truncation analysis in Chapter 2 demonstrated that the change of opacity was a leading source of error. Since $\sigma(t)$ is held constant over a time step, large changes in the opacity during a given time step implies that the assumption is being violated. However, since the photon energy density is a dependent variable, there is no a priori reason to assume that it should not change drastically. Therefore, by building a time step controller based off the change of opacity it maybe possible to directly control the size of the truncation error per time step.

To this end, we propose a time step controller constraint based on the relative change in the opacities during a time step as

$$\max_i \left[\frac{\mid \sigma_i^{n+1} - \sigma_i^n \mid}{\sigma_i^n} \right] \leq \eta_{target}. \tag{5.3}$$

In Eq. 5.3, η_{target} is a user defined relative change that should not be violated. Depending on how close the time step controller is to violating the controlling condition, the time step size can be increased or decreased for the next time step. If the constraint is violated, the controller must determine if the time step must be rerun (which can be infeasible in Monte Carlo simulations due to memory constraints (21)) or alternatively, accept the violation of the controller and significantly reduce the time step size for the next time step.

To explore the effect of both the relative-change-of-photon-energy and relative-change-of-opacity time step controllers, a set of 0D problems is proposed that will examine the effectiveness of both controllers. The problems covered will vary in the functional dependency of σ on temperature at different values of constant heat capacity C_v. The different heat capacity values will affect the end of time step temperature. A smaller heat capacity causes a larger change in temperature than a larger heat capacity for the same amount of energy deposited. Changing the functional form of the opacities will also change the way that the material will emit and absorb energy

during the time step, which will affect the simulation accuracy.

To fully determine the effectiveness of each time step controller, the largest time step that can be taken while not violating the controller is chosen. This time step size is determined by choosing a large Δt as the initial guess for a time step at time t_n. If the controller constraint is violated, then the results are discarded and a slightly smaller time step size is used at time t_n. Successively smaller time steps are used at time t_n until the time step controller constraint is not violated. After the time step controller constraints are met, the problem progresses one time step to $t_{n+1} = t_n + \Delta t$ and then chooses another excessively large time step size for the initial guess for the next time step. The selection of Δt for the next time step is *not* based on the proposed selection outlined in Eq. 5.2. While this time step size section procedure is not typical, we use it in this section (only) because it helps us examine the largest predicted safe time step that can be taken. By focusing on the maximum time step allowed by the time step controller constraints, we can directly compare each controller's ability to constrain truncation error.

In the following figures, three different constant heat capacities are used per opacity model for both time step controllers. Therefore each graph has three different problems solutions due to the change in the heat capacity. The opacity of the system will start out at $\sigma(t_o) = 50$ and have a material temperature of $T(t_o) = 0.1$ for each problem. This means that the value of γ in $\sigma(T) = \gamma/T^n$ will vary to maintain a beginning of simulation opacity of 50.0. In other words, the values of γ will be 5.0, 0.5, 0.05 and 0.005 for the opacity models $1/T$, $1/T^2$, $1/T^3$, and $1/T^4$ respectively. The relative error in material temperature will be examined at the time $t = 0.01$ for each problem against a reference solution to temperature that was created using a time step size of 10^{-7} for each problem. A time step size of 1.0 is used as the initial guess to violate the time step controller constraints. This large time step will cause the time step controllers to optimize to the largest time step size that is acceptable for their constraints.

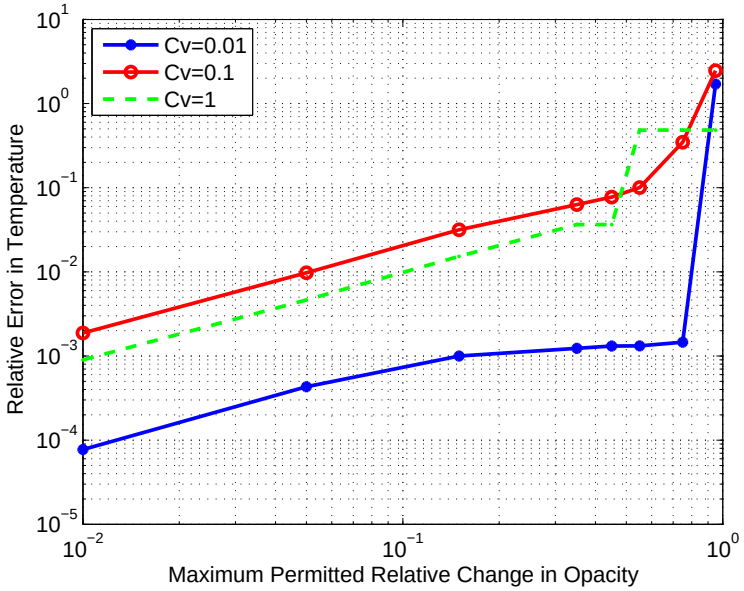

(a) Relative error for a change of opacity.

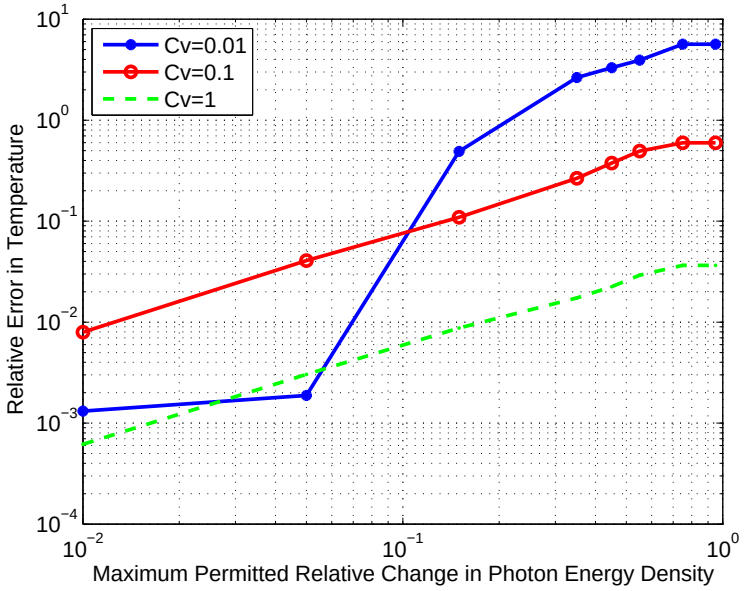

(b) Relative error for a change in photon energy density.

Figure 5.2: Relative error in material temperature for different constant heat capacity values and different changes in the time step controller constraints for a $\sigma = \gamma_1/T^1$ opacity. The maximum change of the abscissa is forced for every time step in the simulation.

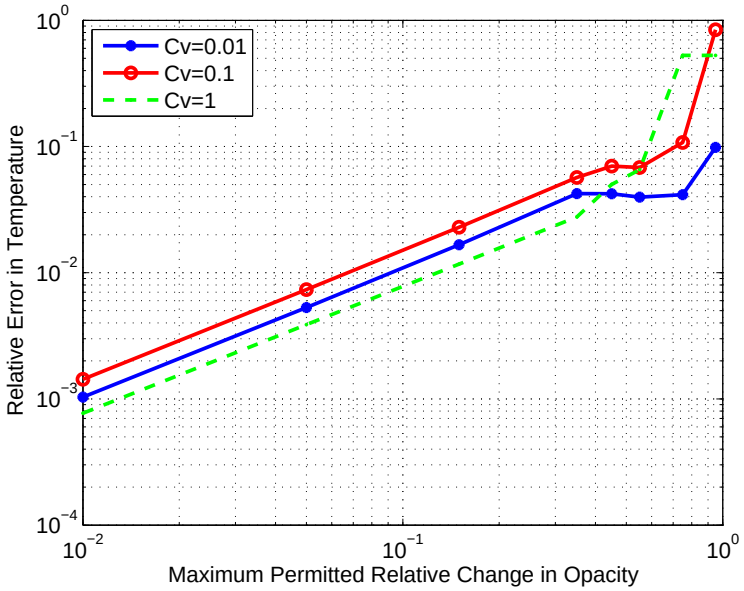

(a) Relative error for a change of opacity.

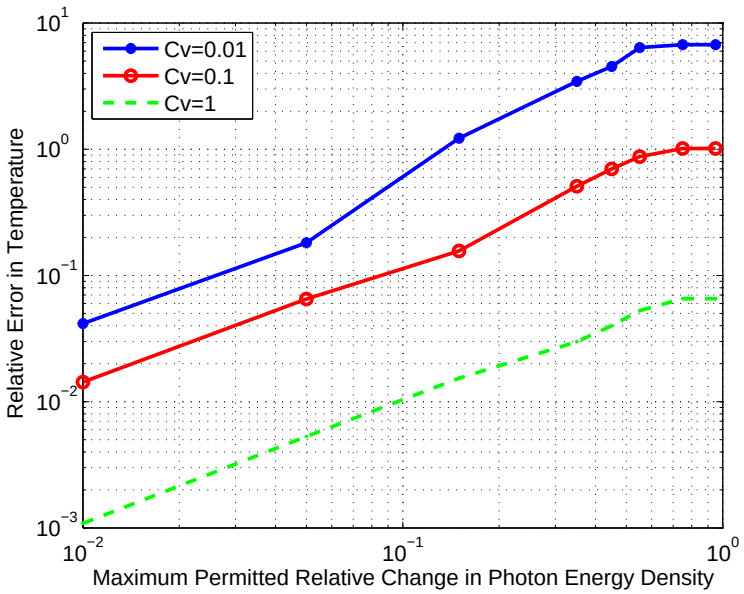

(b) Relative error for a change in photon energy density.

Figure 5.3: Relative error in material temperature for different constant heat capacity values and different changes in the time step controller constraints for a $\sigma = \gamma_2/T^2$ opacity. The maximum change of the abscissa is forced for every time step in the simulation.

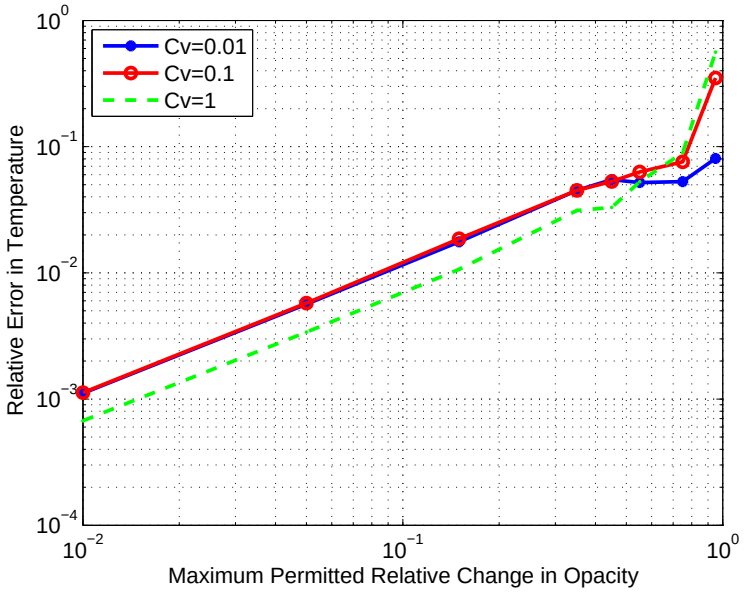

(a) Relative error for a change of opacity.

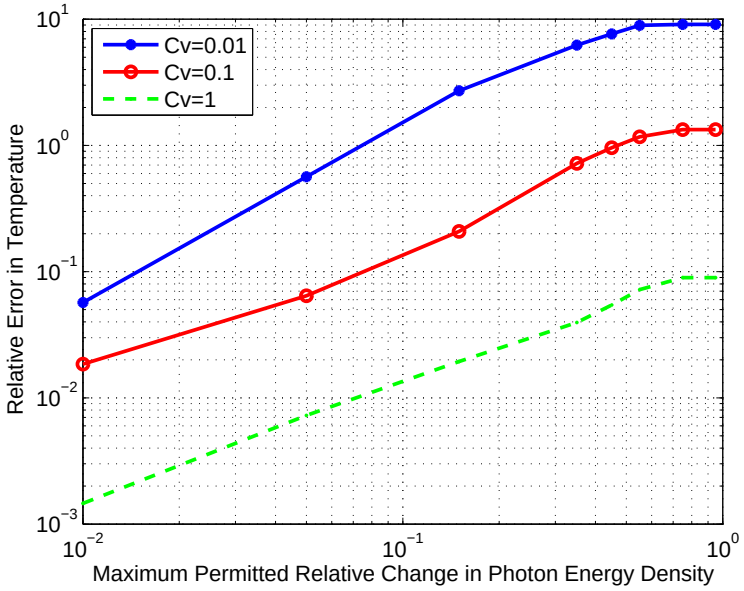

(b) Relative error for a change in photon energy density.

Figure 5.4: Relative error in material temperature for different constant heat capacity values and different changes in the time step controller constraints for a $\sigma = \gamma_3/T^3$ opacity. The maximum change of the abscissa is forced for every time step in the simulation.

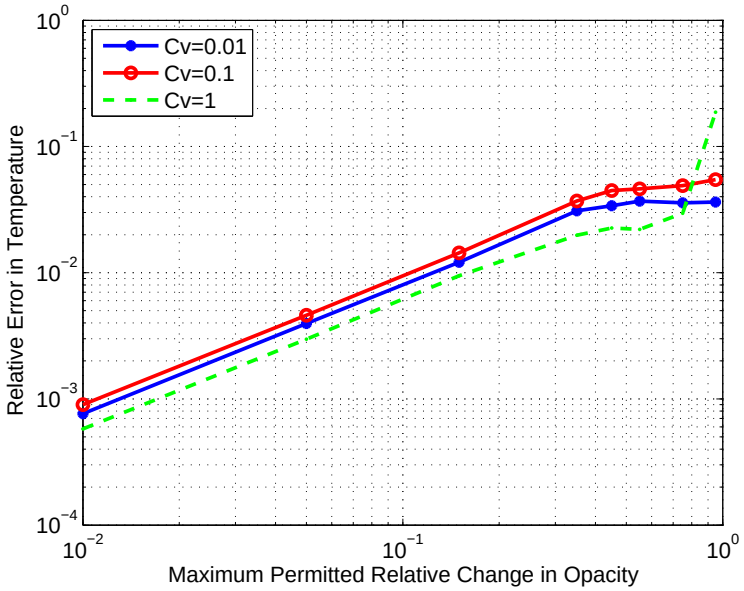

(a) Relative error for a change of opacity.

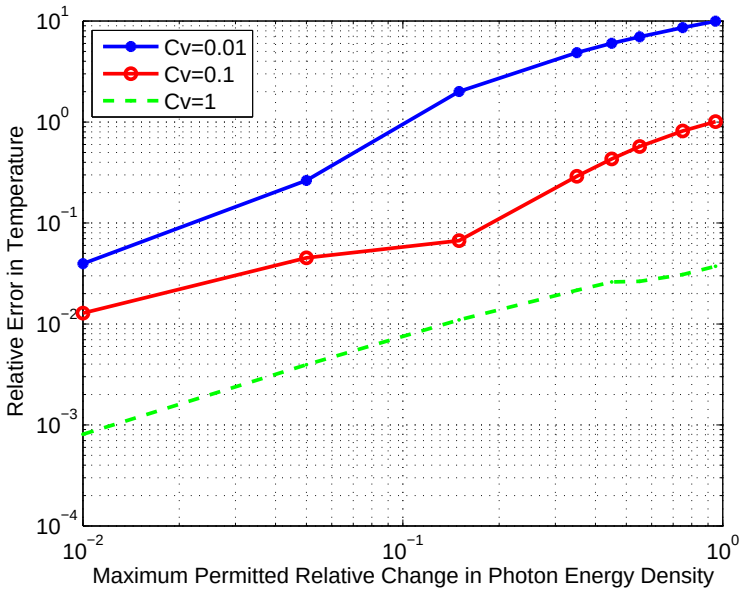

(b) Relative error for a change in photon energy density.

Figure 5.5: Relative error in material temperature for different constant heat capacity values and different changes in the time step controller constraints for a $\sigma = \gamma_4/T^4$ opacity. The maximum change of the abscissa is forced for every time step in the simulation.

Figures 5.2a to 5.5b show a significant difference between the two time step controllers. For large relative changes of opacity or photon energy density, both methods perform poorly and sometimes violate the maximum principle but this is where the

similarities end. The time step controller based on the change in energy density of photons has varied results. The change of the heat capacity has a dramatic effect in the accuracy of the solution for the same relative change of the photon energy. The relative error of the photon energy time step controller changes by orders of magnitude depending on the heat capacity for a given opacity model. As the inverse power of the temperature increases, so does the magnitude of the relative error and the differences between the relative error for each heat capacity. In short, the user will need an intuitive feel for each problem to know how to set the constraint for the change in photon energy density.

However, the time step controller based on the change in the opacity tells a different story. With the exception of the γ_1/T^1 opacity model shown in Fig. 5.2a, the relative error in temperature of the opacity time step controller is remarkably similar even with different heat capacities. By decreasing the allowed relative change of opacity by the time step controller constraint, the γ_2/T^2, γ_3/T^3, and γ_4/T^4 opacity models linearly tend to a relative error in material temperature of 10^{-3} for a relative change of opacity of 10^{-2}. This trend can also be seen in the γ_1/T^1 model except when $C_v = 0.01$ which yields an even lower relative error in temperature of 10^{-4} for an opacity change of 10^{-2}. Generally speaking, the opacity model and heat capacity of the material appear to have negligible effects on the accuracy of the solution when using the opacity time step controller. For these 0D models, the time step controller with the constraint based on the change of opacity does not require any user intuition about the material properties of the problem, making it a much more robust controller. The photon energy time step controller can yield the same numerical results as the opacity time step controller in these simplified problems, but the user must know how to specify the correct constraint for the specific problem that is being run. If material discontinuities exist in the problem, the task of choosing a proper constraint becomes challenging for the photon energy controller due to the its heat capacity sensitivity, but remains trivial for the opacity time step controller.

Another obvious choice for a time step controller constraint is to limit the relative change of material temperature from one time step to the next. Similar to the relative change in opacity constraint, the temperature constraint for the controller is given as

$$\max_i \left[\frac{\mid T_i^{n+1} - T_i^n \mid}{T_i^n}. \right] \leq \eta_{target} \tag{5.4}$$

While we could not find publications on this controller constraint, it is currently used in practice (4). In the 0D homogeneous test problems there is no practical difference

between the opacity constraint and the temperature constraint. However the opacity constraint will prove to be more robust when spatial details are included in a problem. The temperature constraint will be discussed in greater detail later in this chapter.

5.3 Timing Tests for Rerunning Time Steps with a Time Step Controller in 1D

A time step size is chosen at the beginning of the problem simulation and then increased or decreased by a time step controller. If the next time step size needs to be decreased, the previous Δt size selection violated the constraints of the time step controller during the time step. When the time step controller constraint is violated, a decision must be made to either rerun that time step or to accept the results and decrease the time step size for the next time step. The computationally easier approach is to not rerun the time step, which works well assuming that the violations of the time step controller are not severe. Alternatively, a time step could be run again to ensure that the time step controller is not violated. While the cost of rerunning a problem is high, this may still prove to be beneficial if any violation of the time step controller is anticipated to have severe consequences.

Determining the correct size change in a time step after a successful time step or after a violation of the time step controller is a bit of an art. A simple approach to modify the time step size is to decrease it after a violation as

$$\Delta t_{n+1} = \Delta t_n / D \tag{5.5}$$

or to increase the time step size as

$$\Delta t_{n+1} = \Delta t_n M. \tag{5.6}$$

The user defined values of $D > 1$ and $M > 1$ are constants used to divide or multiply the previous time step size to determine the next time step size. This process will be referred to as a DM controller. A timing test is conducted on the nonlinear problem with 32 million source particles, $\Delta x = 0.025$, a maximum $\Delta\tau = 0.5$ and a total simulation time of $\tau = 40$ using the criterion $\sigma_{max} \leq 0.15$. An exceptionally large time step size is initially used to ensure that the maximum principle would be violated so as to test the effectiveness of this time step controller approach. Using the DM controller, each individual time step is rerun until the constraint $\eta_{target} = 0.15$ is met.

Once the constraint is met, the time step size is increased and the next time step follows the same procedure. The effect of different values for the D and M constants are shown in Table 5.1 for the IMC and CF methods.

Table 5.1: IMC and CF opacity time step controller run time (minutes) using DM controller.

IMC Time Step Controller					
$D\backslash M$	2.0	1.75	1.25	1.01	1.005
2.0	14.31	11.96	7.85	6.16	6.11
1.75	15.30	13.73	8.60	5.93	5.84
1.5	18.71	15.57	8.93	5.94	5.84
1.25	27.11	21.40	11.23	5.52	5.84
CF Time Step Controller					
$D\backslash M$	2.0	1.75	1.25	1.01	1.005
2.0	14.88	12.55	8.27	6.14	6.20
1.75	15.90	22.23	17.06	10.41	11.24
1.5	24.33	15.49	9.25	5.93	5.98
1.25	26.72	22.15	11.62	5.65	5.85

As expected, the CF method took slightly longer than the IMC method to run in each case. When comparing the divide by and multiply by values, a general rule of thumb is the D value must be larger than the M value for more optimal results. This is fairly intuitive if the simulation is on the verge of breaking the time step criterion, using a large multiply value will overshoot the correct time step size causing multiple runs of a smaller divide by value to reduce the time step size back down.

A variable weight scheme was added to the DM opacity controller to create a new controller called Variable Weight Divide Multiply Controller (VWDM). The VWDM controller was created to determine if a predictor step (with no corrector) with fewer particles with higher energy could determine if the time step controller would be violated while taking less computational effort. The predictor step is rerun with successively smaller time step sizes until the time step size no longer violates the time step controller constraints. Next, the time step is run one more time using the original photons that should have been transported during that time step. This predictor scheme is not intended to and will not change the order error of the problem. All that the VWDM scheme is attempting to do is determine if the time step size used for the standard implementation of the CF and IMC methods would violate a controller constraint and therefore need to be reduced in size. The timing test results for the VWPC Opacity DM controller are shown in Table 5.2.

Table 5.2: IMC and CF opacity time step controller run time (minutes) using 100VW DM controller.

IMC Time Step Controller with 100 vw Predictor					
$D\backslash M$	2.0	1.75	1.25	1.01	1.005
2.0	10.16	9.75	9.36	13.59	15.27
1.75	10.01	9.57	9.00	13.55	15.55
1.5	10.70	9.74	8.91	12.32	14.37
1.25	12.75	10.98	8.68	11.02	12.46
CF Time Step Controller with 100 vw Predictor					
$D\backslash M$	2.0	1.75	1.25	1.01	1.005
2.0	10.64	10.16	9.64	14.92	16.63
1.75	10.51	10.22	9.39	13.87	16.40
1.5	11.09	10.84	9.09	12.34	13.66
1.25	13.31	11.78	9.22	11.16	11.97

Like before, the CF method is computationally more costly than the IMC approach. While the VWDM Opacity controller shows some speed improvements over the DM Opacity controller in the $M = 2$ column, the VWDM Opacity controller is not competitive with the fastest DM Opacity controller runs for either method. Therefore, a quick predictor step in the VWDM controller does not appear to add significant improvement in computation time compared to the fastest DM controller runs.

As a comparision to the DM Opacity controller, to keep the relative change of the opacities below 0.15 for the entire problem using only a constant time step size, then $\Delta\tau = 6.08 \times 10^{-4}$. This small time step requires 65790 time steps to reach $\tau = 40$. Therefore it is clear that a time step controller that can control the error in the problem will significantly decrease the number of time steps required to yield an accurate solution.

5.4 Implementation of Time Step Controllers Without Reruns in a Homogeneous 1D Slab

The relative change of the opacities of the 1D reference solution for the nonlinear problem with a time step size $\Delta\tau = 0.005$ and $\Delta x = 0.01$ can be seen in Figs. 5.6a and 5.6b. This relative change of the value of σ from time step to time step starts off at a large value due to effectively an instantaneous source starting at time $\tau = 0$ at

the left boundary. As the problem progresses in terms of cycles, the relative change in σ decreases as the Marshak wave moves further from the source driving it. Zooming in

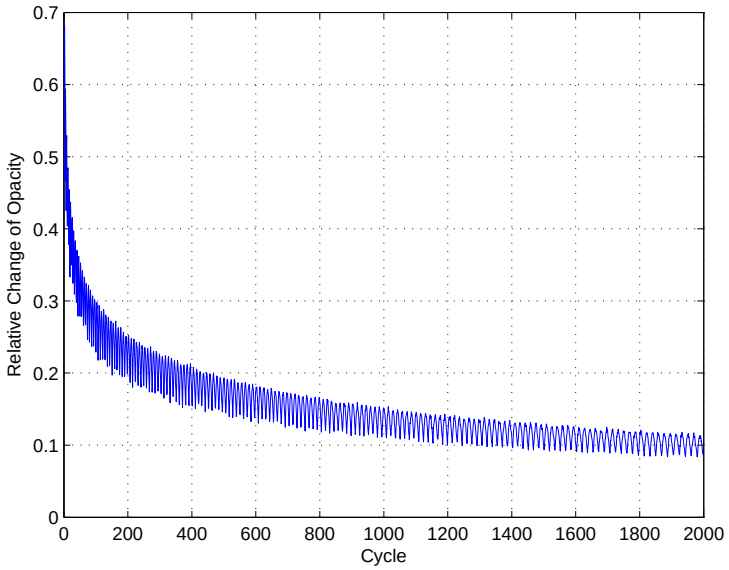

(a) Trend of the largest relative change of opacity for each time step.

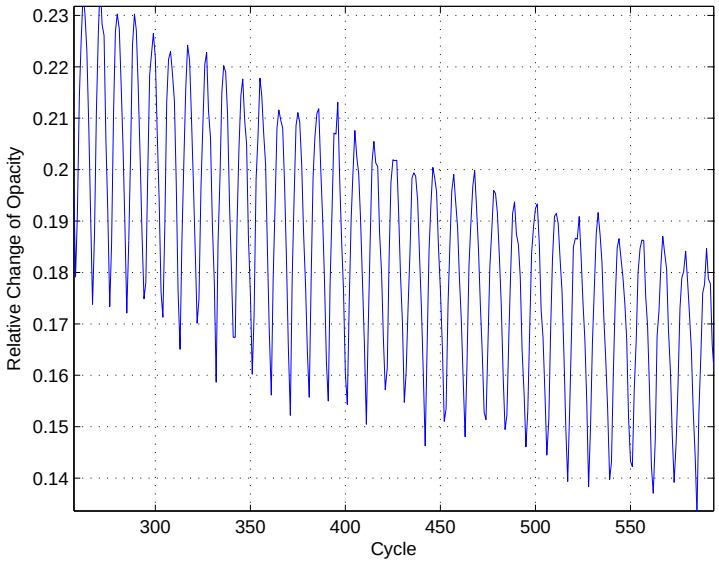

(b) Oscillations in the largest relative change of opacity for each time step.

Figure 5.6: Relative change of $\sigma(t)$ from the previous cycle in a refined IMC solution for the Nonlinear Problem.

on the relative change of σ, oscillations can be seen. These are due to the progression of the Marshak wave from one cell to the next. The trough occurs at the time just

before the Marshak wave enters a new cell and the crest represents when the wave is about half way through the cell.

By constraining the problem so the opacities can not change more than a given amount, the cumulative effects of inaccurate transport may be examined. Using different values for η_{target} for the relative change of opacity, the Marshak wave front is examined at time $\tau = 20$ and spatial width $\Delta x = 0.025$. The time step size is chosen during run time to meet the constraint on the change of the opacities. In these runs if the time step controller constraint is exceeded, the time step is rerun using a smaller value of Δt. Figure 5.7 shows the effect of the time step controller on the location of the wave front. Although none of these results violate the maximum principle, the

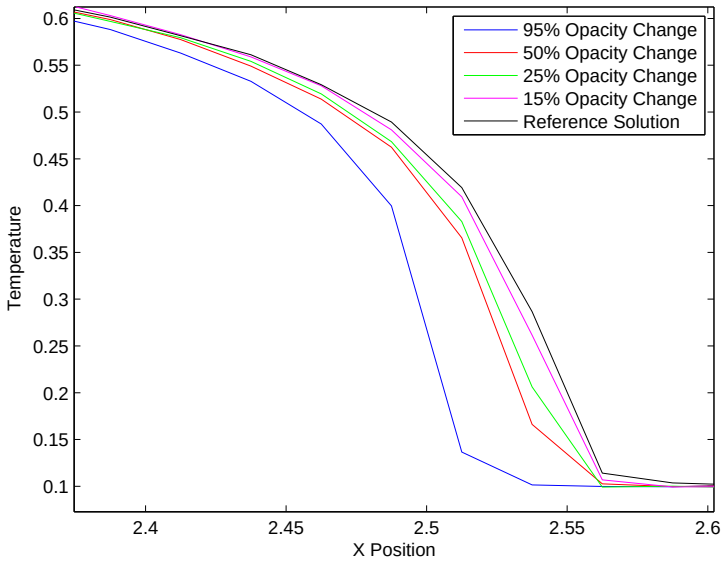

Figure 5.7: Wave front location for different η_{target} values in the Nonlinear Problem.

wave fronts are in distinctly different locations. By keeping larger opacities for an extended period of time, the wave front is slowed as it tries to transport through the slab. This slowing process occurs without any indication of error. Effectively, allowing large changes of opacity during a time step is like modeling a different problem than actually intended. For this particular problem, it appears that a $\eta_{target} = 0.15$ is an effective constraint to reconstruct the correct location of the Marshak wave front compared to the reference solution.

There is a difficulty in correctly determining the development of error in time with respect to using Monte Carlo methods. In the regions in front of the Marshak wave, there are few particles that simulate the transfer of energy due to photons, allowing for a noisy solution. Figure 5.8 shows the differences in temperature between the reference

solution and a time step controller run in a region before the Marshak wave. Due

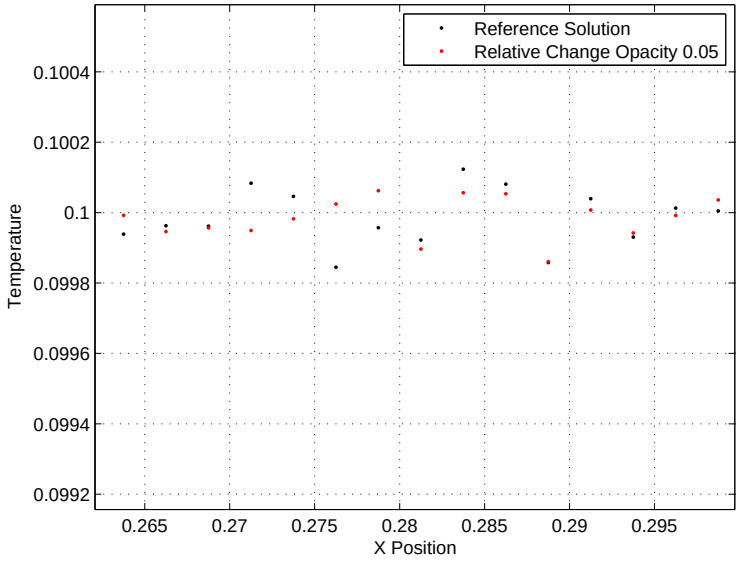

Figure 5.8: Material equilibrium before the Marshak wave front.

to this noisy approximation of temperature in a region of little interest, the relative error in temperature will be examined by only examining regions in the problem that have been exposed to the Marshak wave. The average relative error in temperature is calculated by:

1. Determine the number of cells N that are at a material $T > 1.005$ in time step i
2. Sum the relative error in temperature of the N bins as:

$$R_{\text{error}} = \sum_{N} \frac{\mid T_{i,n} - T_{i,n}^{\text{Ref}} \mid}{T_{i,n}^{\text{Ref}}}$$

3. Average the relative error R_{error} to compare the solutions as:

$$R_{\text{avg}} = R_{\text{error}}/N$$

The average relative error in temperature R_{avg} will be used as the metric to compare the differences in methods for the remainder of this chapter.

To examine the differences between the opacity and photon energy density time step controllers, the 1D nonlinear problem is examined with a small spatial resolution. Using $\Delta x = 0.00025$, an initial time step size $\Delta t = 0.000005$, and a total simulation time of 0.05 was chosen. The two controllers are compared using different values of η and a time step size change dictated by Eq. 5.2 against a reference solution generated

using $10,000$ time steps with a constant Δt. Figures 5.9a and 5.9b show the relative error of the time step controllers during the simulation time.

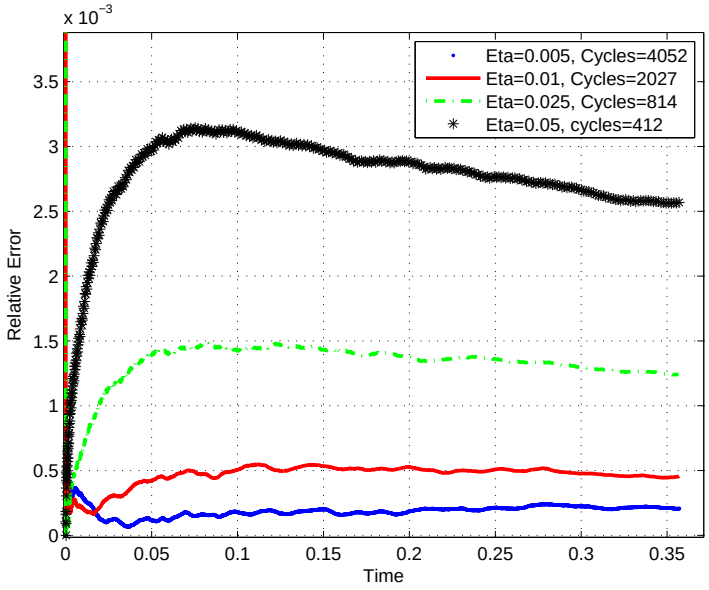

(a) Opacity time step controller.

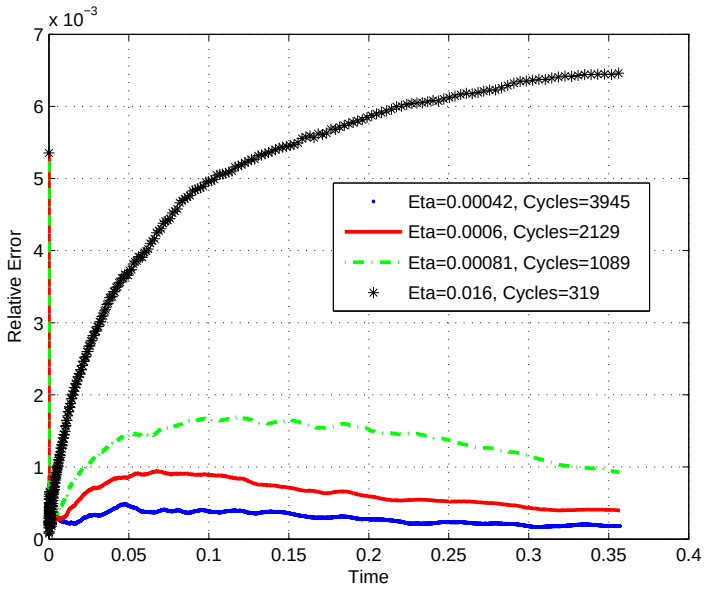

(b) Photon energy density time step controller.

Figure 5.9: Relative error of time step controllers vs. simulation time.

The controller based on an opacity constraint has less relative error for the same number of cycles as the controller based on photon energy density. Furthermore, the opacity controller appears to have a nearly constant relative error for smaller values of η, demonstrating that the error is being controlled. In comparison the photon energy

density controller does not always to constrain the error to a given level. In particular, when $\eta = 0.016$ the relative error increases monotonically with time when using the photon energy density controller.

To better understand the differences between the two controllers, the location of the material cell with the largest change for the controller is determined. Figures 5.10a and 5.10b show the differences between the two time step controller constraints using $\eta = 0.01$ for the opacity constraint and $\eta = 0.0006$ for the photon energy density constraint. The selection of the values of η correspond to roughly 2000 time steps for both implementations. While the opacity controller has a smooth transition from one cell to the next, following the Marshak wave, the energy density controller is working in a nearly random cell from one time step to the next. While the photon energy density is as stable as the temperature in deterministic methods, the same is not true in Monte Carlo methods. The transport of photons in optically thin cells creates a great deal of noise that is not represented in the material temperature or opacity. Therefore, the controller based off photon energy density does not appear to be a valuable heuristic for determining the locations of interest during this Monte Carlo simulated Marshak wave.

Figure 5.11 demonstrates the effect of noise on the two different controllers and their selection of a time step size. While the opacity controller is smoothly transitioning to a larger time step size, the energy density controller appears to struggle to determine an appropriate time step size. This is an anticipated result since it is clear from Fig. 5.10b that the photon energy controller is not choosing the cell location where the physics are changing the fastest. Therefore it is not clear that the time step size selection would ever be relevant to truncation error in a single time step. Because of the poor performance of the photon energy density controller in Monte Carlo methods it will no longer be considered as a viable option. However, the opacity time step controller appears to be a stable choice that appropriately increases the time step size. To gauge the effectiveness of the opacity time step controller, it will now be compared to a controller based on the relative change of temperature (4).

As we mentioned in Section 5.2, the temperature controller gave similar results as the opacity controller in 0D. Both methods take the heat capacity of the material into consideration unlike the photon energy density controller, making them more robust. Furthermore, the relative change of temperature and opacity can be related. Define the relative change of temperature as

$$\Upsilon = \frac{\mid T_{n+1} - T_n \mid}{T_n} \tag{5.7}$$

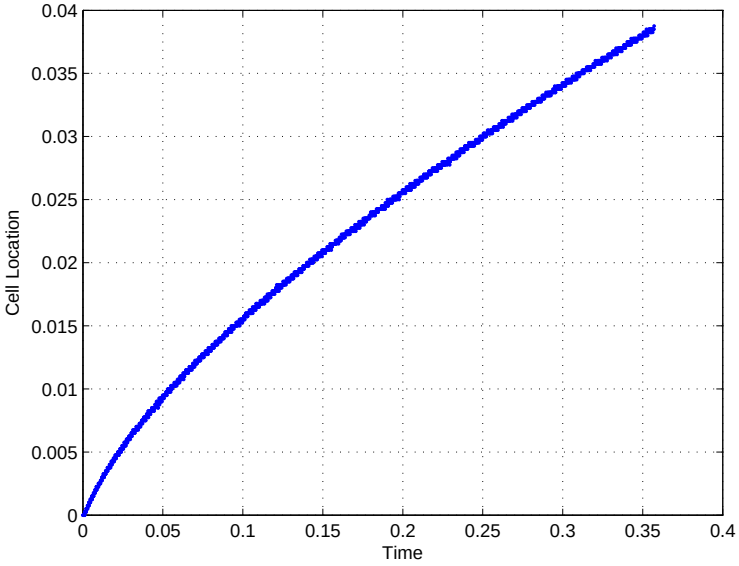

(a) Opacity time step controller.

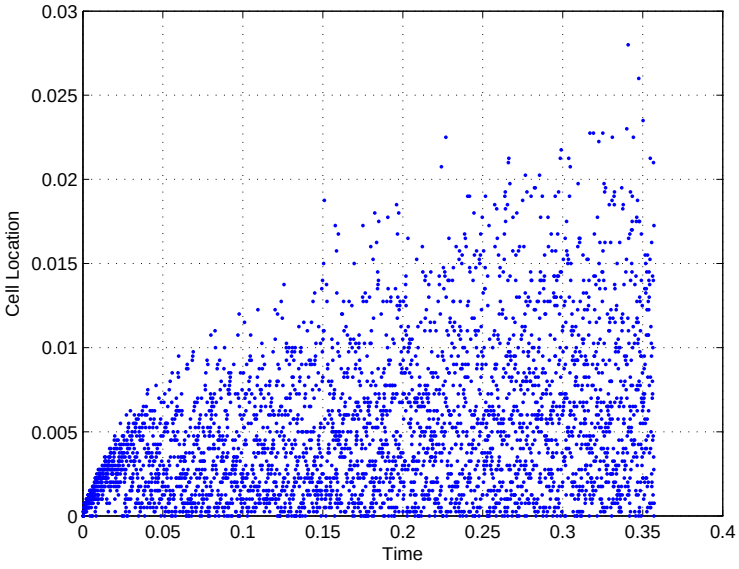

(b) Photon energy density time step controller.

Figure 5.10: Location of maximum change for the controller vs. simulation time.

and the relative change of opacity as

$$R = \frac{\mid \sigma_{n+1} - \sigma_n \mid}{\sigma_n}. \tag{5.8}$$

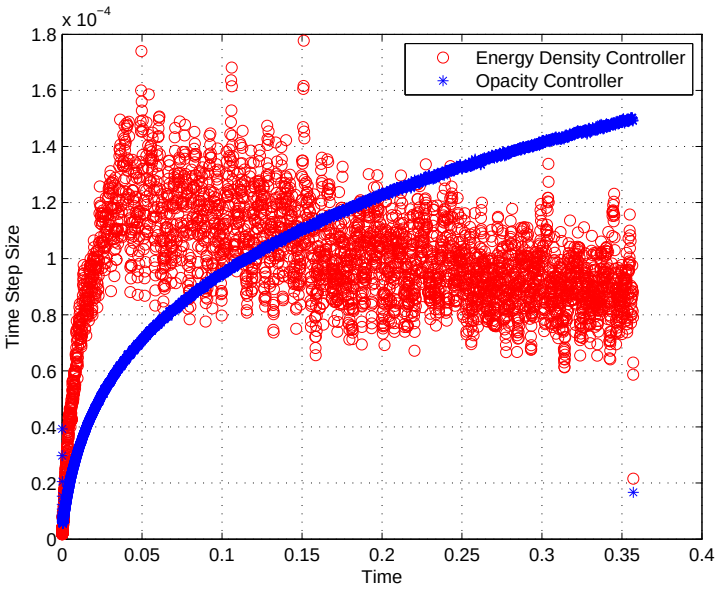

Figure 5.11: Time step size vs. simulation time.

Using a simple model $\sigma = \gamma/T^m$, the relative change in opacity can be stated as

$$R = \frac{\left| \frac{\gamma}{T_{n+1}^m} - \frac{\gamma}{T_n^m} \right|}{\frac{\gamma}{T_n^m}} = \left| \frac{T_n^m}{T_{n+1}^m} - 1 \right|. \tag{5.9}$$

Equation (5.7) is solved for T_{n+1} as

$$T_{n+1} = T_n(1 + \Upsilon) \tag{5.10}$$

and then substituted into Eq. (5.9) to give

$$R = \frac{\left| 1 - (1 + \Upsilon)^m \right|}{(1 + \Upsilon)^m}. \tag{5.11}$$

Examining the temperature range $T_n < T_{n+1} < \infty$, which implies warming of the material, the relative change in temperature is constrained as $0 < \Upsilon < \infty$ allowing Eq. (5.11) to be written as

$$R = \frac{(1 + \Upsilon)^m - 1}{(1 + \Upsilon)^m}. \tag{5.12}$$

Therefore, a constraint on the change of temperature Υ will also constrain the relative change of opacity as $0 < R < 1$ for this warming problem. For a fixed change of

temperature, there will be a fixed change of opacity as shown in Fig. 5.12.

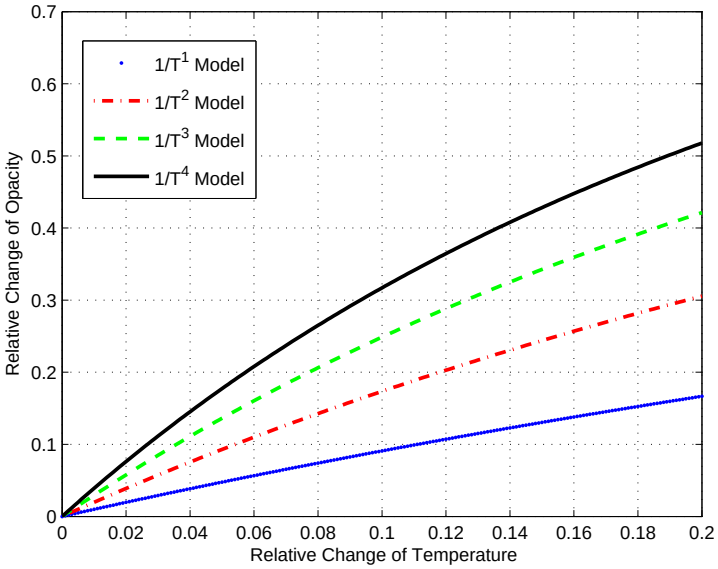

Figure 5.12: Change of opacity due to change of temperature for different opacity models.

The relationship between temperature and opacity is why there was no significant difference between the two controllers in the 0D and homogeneous 1D models. A change of temperature can be chosen that will constrain the change in opacity at a given value. Therefore the two controllers can be made equivalent in these simple problems. However, while these two controllers are clearly tightly coupled together, the opacity controller has more relevance to controlling truncation error as shown in Chapter 2.

To demonstrate this, note from Fig. 5.12 that a relative change of temperature of 0.1 has different changes of opacity from 0.1 to 0.31 for these different simple power models for opacity. Therefore, the temperature controller can have significantly different changes in opacity for a fixed relative change in temperature. A comparison of the two controllers is conducted for the γ_1/T, γ_2/T^2, γ_3/T^3, and γ_4/T^4 opacity models used with a constant heat capacity. The values of γ_m are chosen so that the material has an initial opacity of 1000 for each opacity model. The spatial width is given as $\Delta x = 0.001$, the starting time step size is $\Delta t = 0.0001$, $\beta = 0.56$ and a total simulation time of 0.1. Figures 5.13a to 5.14b show the degradation of the accuracy of the solution when using the relative change of temperature controller compared to the reference solution. As expected from Fig. 5.12, the results for the $1/T$ opacity model are nearly identical for the opacity and temperature TSC's.

Conversely, the $1/T^4$ opacity model shows a significant difference between the two controller constraints at $\eta_{target} = 0.1$. The relative change of opacity controller does a much better job of resolving the reference solution for the different γ_m/T^m opacity models. This improvement can be seen at the Marshak wave front where the opacity controller demonstrates itself to be equal to or better than the temperature controller (both methods using $\eta_{target} = 0.1$).

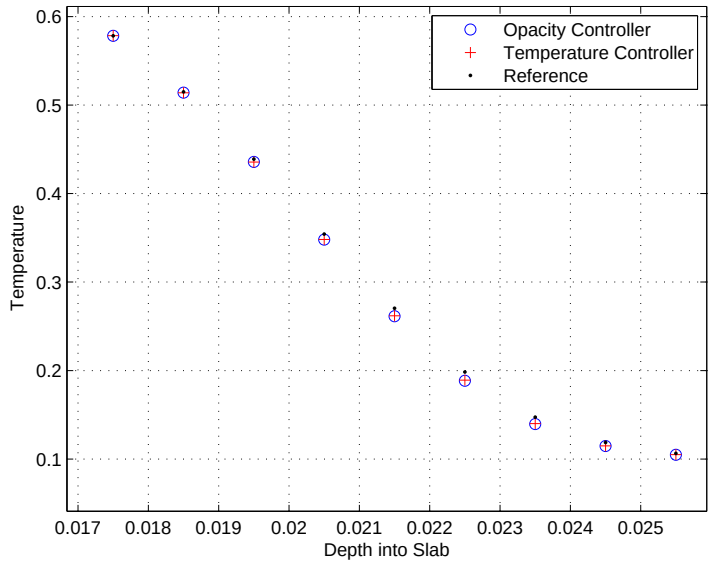

(a) Opacity model γ_1/T.

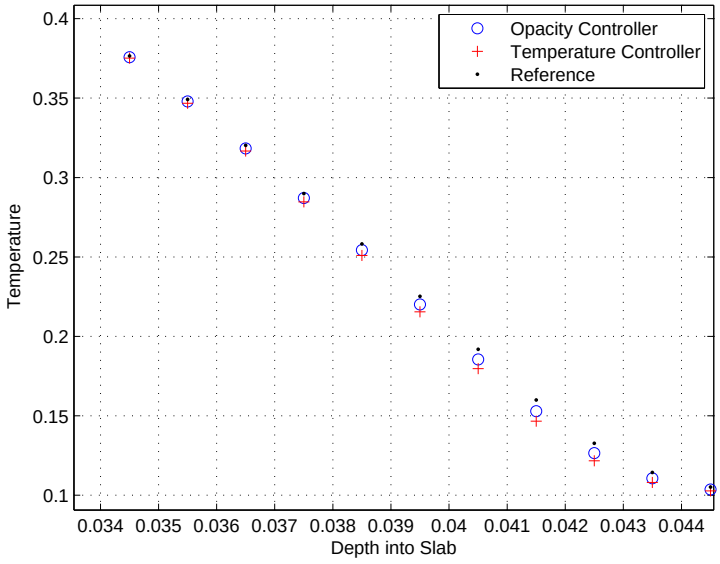

(b) Opacity model γ_2/T^2.

Figure 5.13: Marshak wave front for the different time step controllers with $\eta_{target} = 0.1$.

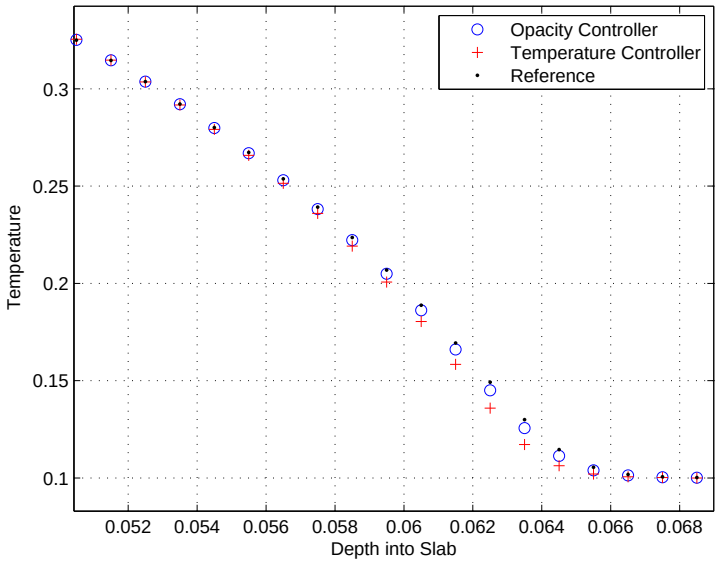

(a) Opacity model γ_3/T^3.

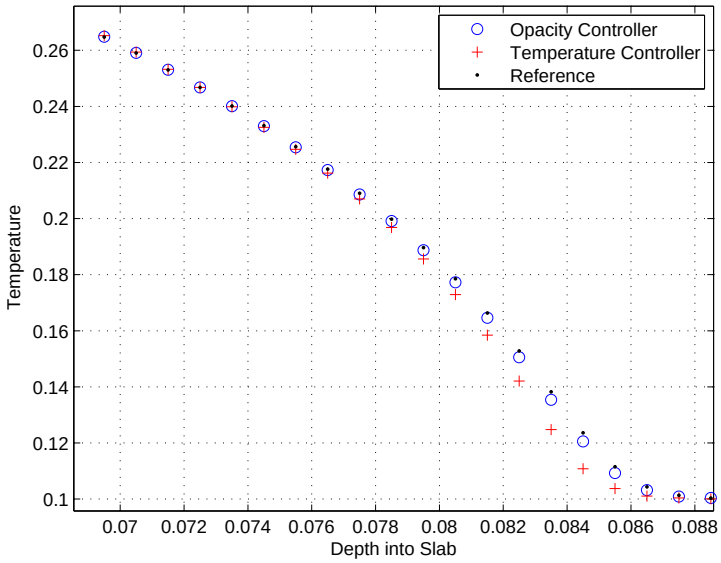

(b) Opacity model γ_4/T^4.

Figure 5.14: Marshak wave front for the different time step controllers with $\eta_{target} = 0.1$.

In Figs. 5.13a to 5.14b, the number of total time steps used to show the Marshak wave at $\tau = 0.1$ was not the same for the two controllers. While the two controllers used a similar number of time steps for the γ_1/T model, the opacity controller used more smaller time steps in the $m > 1$ opacity models. This is an expected result since Fig. 5.12 shows that the relative change of temperature and opacity are nearly the same for the $1/T$ opacity model, but significantly different at the $1/T^4$ opacity

model. Therefore the opacity time step controller constrains the quickly changing opacity and appears to be constraining the error from one time step to the next. However the temperature controller does not seem to adapt to constrain the error for the same value of η_{target} on the changing problems like the opacity controller. The temperature controller appears to successively show a decreasingly accurate depiction of the Marshak wave front.

5.5 Time Step Controllers in a Multi-Material 1D Slab

Since the opacity and temperature controller constraints have a direct relationship in simplified gray homogeneous problems, a multi-material problem is required to separate the characteristics of each approach. Using different temperature dependencies in the opacity model, the time step controllers will no longer be equivalent. In these problems we will be using a DM controller with $D = 1.25$ and $M = 1.05$. During the following TSCPC runs, there will be no time step rerunning. The multi-material problems examined are composed of two materials. The material located from $0 \leq x \leq 0.1$ uses an opacity model of $0.1/T^4$, while the material located from $0.1 < x \leq 0.3$ uses an opacity model of $10/T^2$. Both materials start at an initial temperature $T_0 = 0.1$, implying both materials have a starting material opacity of 1000. Using $c = a = 1$, a constant heat capacity $C_v = 1/.14$, a 1 unit isotropic source on the left boundary with vacuum boundary conditions, an initial time step size $\Delta\tau = 0.005$, and a simulation time out to $\tau = 1$. This problem will hence forth be referred to as Problem 8. The average relative error in temperature is compared for the temperature and opacity controllers in Fig. 5.15.

For large values of η_{target} there is a decrease in the average relative error for the problem as the simulation progresses. For $\eta_{target} = 0.4$ for the opacity controller and $\eta_{target} = 0.2$ for the temperature controller, it is clear that the opacity controller does a better job at the beginning of the simulation. However, as the simulation continues the temperature controller becomes the more accurate estimate of the Marshak wave front. As the value for η_{target} becomes smaller, both controllers appear to be able to maintain a constant average relative error in temperature.

By changing η_{target} by a factor of two, the two controllers have different responses for the number of time steps that are simulated as seen in Table 5.3. The opacity controller almost perfectly doubles the number of time steps required when the relative

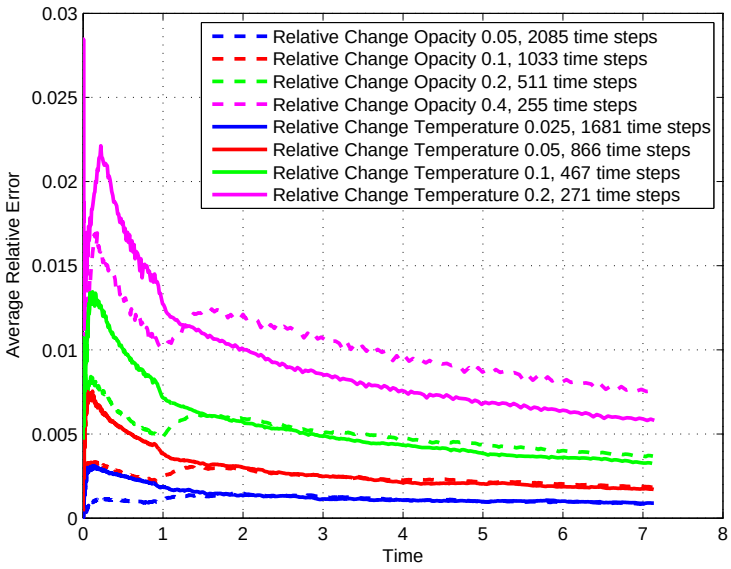

Figure 5.15: Average relative error in temperature vs. simulation time using opacity and temperature TSC's for Problem 8.

Table 5.3: η_{target} values and time steps taken for time step controllers for Problem 8

Opacity time step controller.	
η_{target}	time steps taken
0.4	255
0.2	511
0.1	1033
0.05	2085

Temperature time step controller.	
η_{target}	time steps taken
0.2	271
0.1	467
0.05	866
0.025	1681

change allowed is halved. However, the temperature controller time steps do not follow a predictable pattern. This indicates that the user defined relative change corresponds more directly with time steps required in the opacity controller than in the temperature controller.

Looking how the different controllers evolve the time step in Fig. 5.16, we can see how the two approaches differ. The opacity controller uses a larger number of time steps (with a smaller size) at the beginning of the simulation time and a smaller number of time steps (with larger size) at the end. It can be seen that at a time just before 1, the Marshak wave passes from the $0.1/T^4$ opacity model material to the $10/T^2$ opacity model material causing a pronounced shift in the time step size selection. The change of material also changes the relative rate at which the material

temperature changes and the opacity changes over a time step. This has the effect of making the opacity controller more accurate at the beginning of the simulation time, then often being overtaken by the temperature controller in accuracy at later time steps. The DM controller used for this problem caused the time step to be rerun on

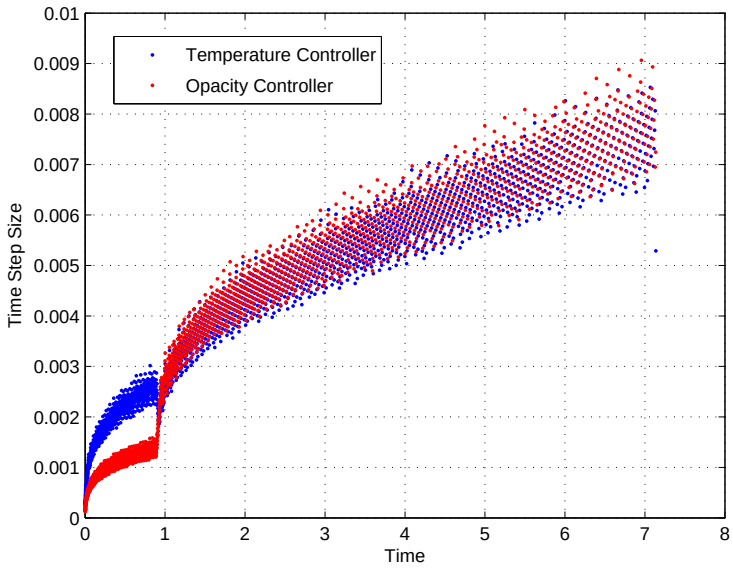

Figure 5.16: Time step size vs. time using a relative change of 0.05 for opacity and 0.025 for temperature.

average about every 4.7 time steps. The number of reruns can be minimized as was previously discussed by changing the D and M parameters.

Our next multi-slab problem is almost identical to Problem 8. The only difference is that the materials are switched in the previous problem such that the material located from $0 \leq x \leq 0.1$ uses an opacity model of $10/T^2$ while the material located from $0.1 < x \leq 0.3$ uses an opacity model of $0.1/T^4$. This material configuration will be referred to as Problem 9. By switching the materials, the less temperature sensitive material is now next to the source, changing the characteristics of the simulation, as shown in Fig. 5.17.

Like before, the opacity controller has a strong relationship between the change of time steps used in a simulation and the change of the relative change parameter shown in Table 5.4. The temperature controller again does not have a linear relationship between the relative change of temperature and the number of time steps used. However, what has changed is the accuracy of each controller over the course of the simulation time. Unlike previously, the opacity controller now takes fewer time steps at the beginning of the simulation as the Marshak wave passes through the $10/T^2$

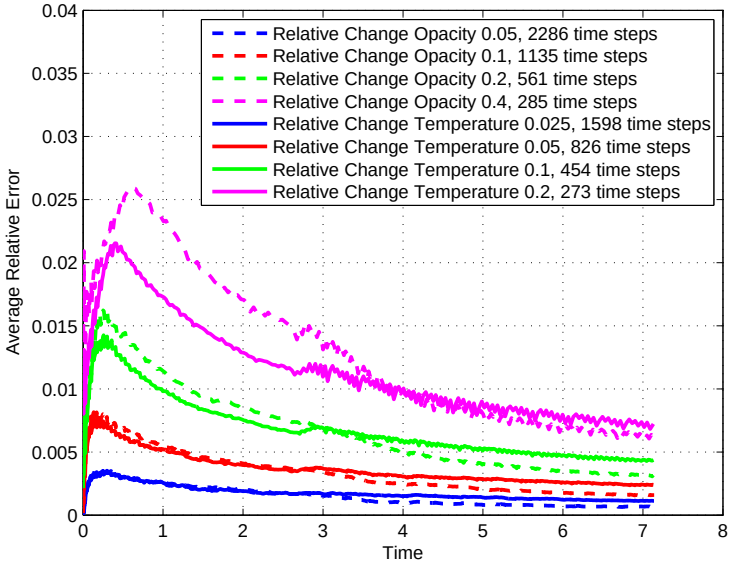

Figure 5.17: Average relative error in temperature vs. time in Problem 9.

material and more time steps near the end of the simulation as the Marshak wave passes through the $0.1/T^4$ material than the temperature controller.

Table 5.4: η_{target} values and time steps taken for time step controllers for Problem 9

Opacity time step controller.	
η_{target}	time steps taken
0.4	285
0.2	561
0.1	1135
0.05	2286

Temperature time step controller.	
η_{target}	time steps taken
0.2	273
0.1	454
0.05	826
0.025	1598

These differences mean that the opacity controller is less accurate at the beginning of the simulation and improves during the course of the simulation compared to the temperature controller. Effectively, the temperature controller or the opacity controller can be shown to be more accurate for a given number of time steps in a given problem. Neither controller will be best for every problem. However, the opacity controller appears to directly constrain the truncation error in a problem as we would expect from the truncation error analysis in Chapter 2. As noted earlier, it is better to constrain the opacity since it is an input variable instead of the photon energy density since there is no a prior knowledge of how quickly that dependent variable should change.

5.6 Time Step Controller with Predictor-Corrector Methods

The methods that have been proposed in this thesis can be combined in beneficial ways that are not initially intuitive. When using a predictor-corrector with a time step controller, the predictor step can be used to adjust the corrector step time step size. Assuming that the opacity changes are linear over a single time step, if a violation of the time step controller occurs in the predictor step a good approximation can be used to determine the time step size for the corrector step. The corrector step is then run using a new time step size determined by the predictor step and time adjusted opacities or temperatures that correspond to the new end of time step values for the predictor step.

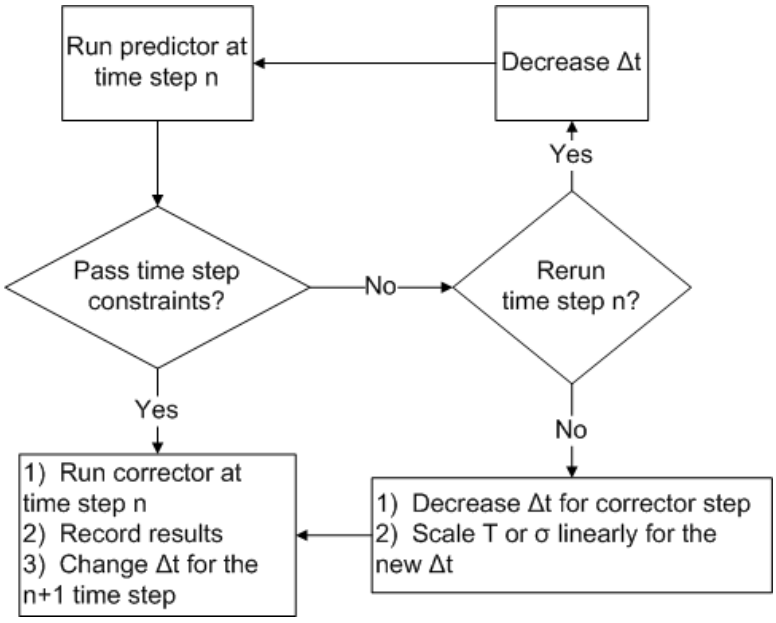

Figure 5.18: Time step controller with predictor-corrector flow chart.

The corrector step then runs a single time step and then determines the maximum change of temperature or opacity that occurred over the problem. This maximum change is then used with the time step controller to determine the next time step size that should be taken in the predictor step. In this particular instance, if the time step controller is violated in the predictor or the corrector calculation, the time step is not rerun. It is assumed that the predictor step will adequately identify the appropriate time step size that should be used. If the time step size for the corrector

step is reduced, the value of σ_{n+1} or T_{n+1} will be scaled linearly as

$$\sigma_{n+1}^{'} = \frac{\sigma_{n+1} - \sigma_n}{\Delta t}\Delta t^{'} + \sigma_n \tag{5.13}$$

and

$$T_{n+1}^{'} = \frac{T_{n+1} - T_n}{\Delta t}\Delta t^{'} + T_n \tag{5.14}$$

where $\Delta t^{'}$ is the new time step size determined by the predictor step. The values of $\sigma_{n+1}^{'}$ and $T_{n+1}^{'}$ will be used as the results of a predictor step of time step size $\Delta t^{'}$ as shown previously in Chapter 4. The predictor step in the following problems will only decrease the time step size and not increase it to be conservative. A flow chart of this procedure can be seen in Fig. 5.18. This method will be referred to as a Time Step Controller with Predictor-Corrector (TSCPC)

The CETDOPC and the WLTPC will be examined using the opacity time step controller on the previously defined Problem 8 using an initial large time step $\Delta t = 0.005$ to a time of $\tau = 1$ with 100 million source particles. Figure 5.19 shows the two predictor-correctors as their error develops over the simulation. It can be clearly seen

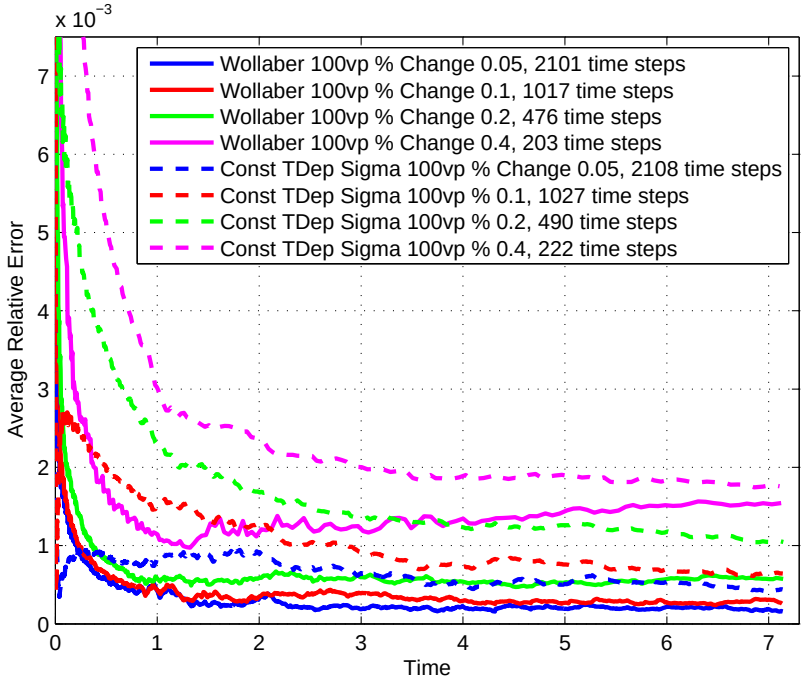

Figure 5.19: Average relative in temperature error of the CETDOPC and the WLTPC using the opacity time step controller on Problem 8.

that the average relative error plots of both methods decrease rapidly at the beginning of the simulation. This is due to the fact that there are no reruns in the TSCPC

method and the simulation is started with a very large initial time step. Without reruns to correct the inaccurate transport, the linear interpolation of opacity is not an accurate prediction of an appropriate time step size to take with these poor initial conditions. However, very quickly a smaller time step size is settled on that brings the error of the simulation down dramatically, and the TSCPC without reruns performs well. Both TSCPC schemes achieve a low error without reruns but the time step controller with the WLTPC yields a lower error result. This result is surprising since there is not a single $1/T^3$ dependency of the opacity in the entire problem.

Comparing the results of the WLTPC to the basic opacity time step controller, you can see a marked improvement in Fig. 5.20. The time step controller with WLTPC is

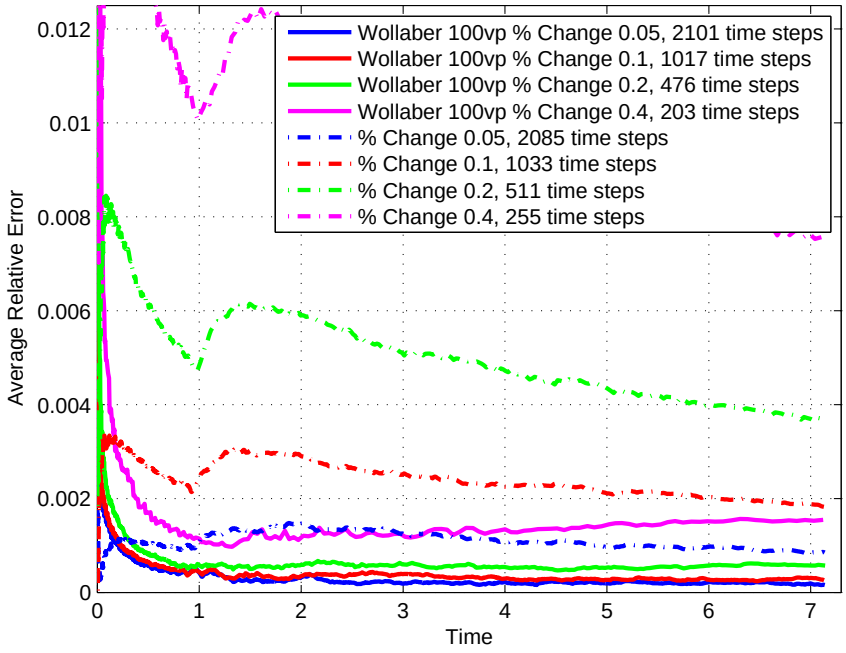

Figure 5.20: Average relative error in temperature of the CETDOPC and WLTPC using the opacity time step controller on Problem 8.

has a low average relative error using 476 time steps compared to the opacity time step controller using 2085 time steps. Even if the predictor-corrector took twice the amount of time per time step as the basic opacity time step controller approach, the time step controller with WLTPC would still be faster and more accurate for the majority of simulation time. To compare all three of the previously mentioned approaches a table is generated to compare the average of the summed average relative error for each method at each % change of opacity for the controller shown in Table 5.5.

It is clear that both TSCPC's yield a more accurate solution than the basic opacity

Table 5.5: Characteristics of the opacity time step controller, the WLTPC and CETDOPC with the opacity time step controller on Problem 8.

Average of the summed average relative error.			
% Change\Method	Opacity TSC	WLTPC	CETDOPC
0.4	0.01138	0.00264	0.00692
0.2	0.00554	0.00118	0.00309
0.1	0.00252	0.00080	0.00149
0.05	0.00108	0.00064	0.00082
Number of time steps used.			
% Change\Method	Opacity TSC	WLTPC	CETDOPC
0.4	255	203	222
0.2	511	476	490
0.1	1033	1017	1027
0.05	2085	2101	2108
Run time (wall time) for simulation in minutes.			
% Change\Method	Opacity TSC	WLTPC	CETDOPC
0.4	143.0	128.3	170.6
0.2	155.9	142.4	185.0
0.1	189.2	185.3	238.9
0.05	260.9	285.8	355.7

time step controller for a similar number of time steps over the development of the entire problem. For this problem, the CETDOPC yields a more accurate solution than the opacity TSC for a given η_{target} but at a significant computational cost. The additional computational cost of the CETDOPC means that it is competitive with the opacity TSC, but not a clear winner. The WLTPC with the opacity time step controller on the other hand, is surprisingly accurate compared with the other approaches. This result is surprising since there is not a γ/T^3 opacity model in Problem 8 which was one of the fundamental assumptions in generating the WLTPC. Examining the run times for the different approaches, the WLTPC is both more accurate and faster than the other approaches until $\eta_{target} = 0.05$.

The accuracy of the WLTPC approach in these problems merits understanding. One of the fundamental approximations made in the WLTPC is that the temperature change over a sufficiently small time step is linear. Because of this assumption, the Wollaber-Larsen temperature estimate will reduce in Eq. 3.6 to a simple linear average of temperature as mentioned in Chapter 3. Therefore, we expect the WLTPC and the Temperature Averaged Predictor-Corrector (TAPC) to have a similar performance for

small time step sizes. A comparison of the two TSCPC can be seen in Fig. 5.21

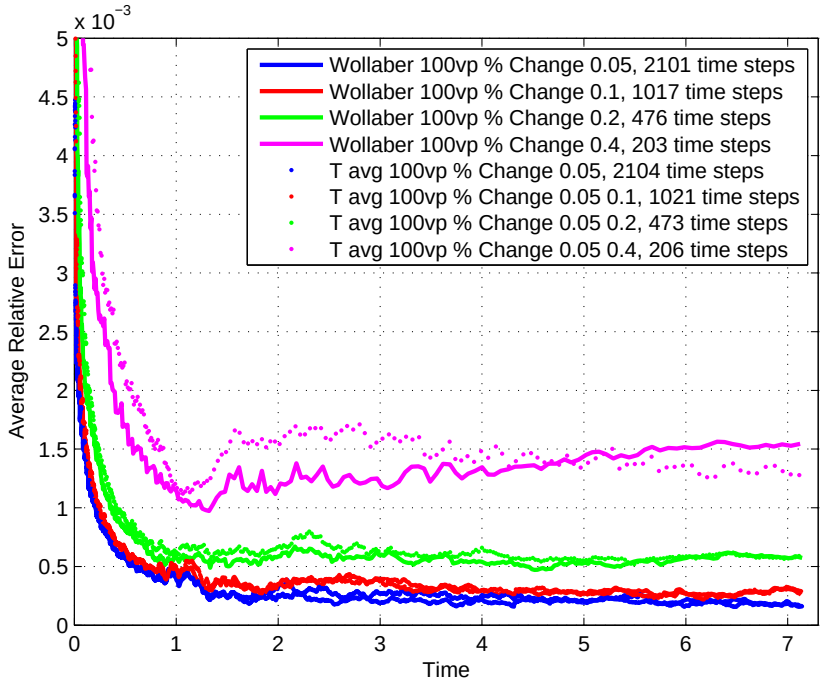

Figure 5.21: Average relative error in temperature of the WLTPC and TAPC using the opacity time step controller on Problem 8.

As expected, for smaller time step sizes the WLTPC and TAPC methods approach the same solution. This result implies that the assumption of the functional form of the opacities is *not* the source of the accuracy improvements in the WLTPC. Noting this distinction, the TAPC method could be a substitute for the WLTPC approach for sufficiently small time step sizes.

Next, Problem 9 is examined with the WLTPC and the CETDOPC like Problem 8 to determine the effectiveness of each method. As before, the WLTPC appears more accurate than the CETDOPC approach as shown in Fig. 5.22 while using a similar number of time steps. The reduced average relative error of the WLTPC method occurs despite there being no $1/T^3$ dependency in Problem 9.

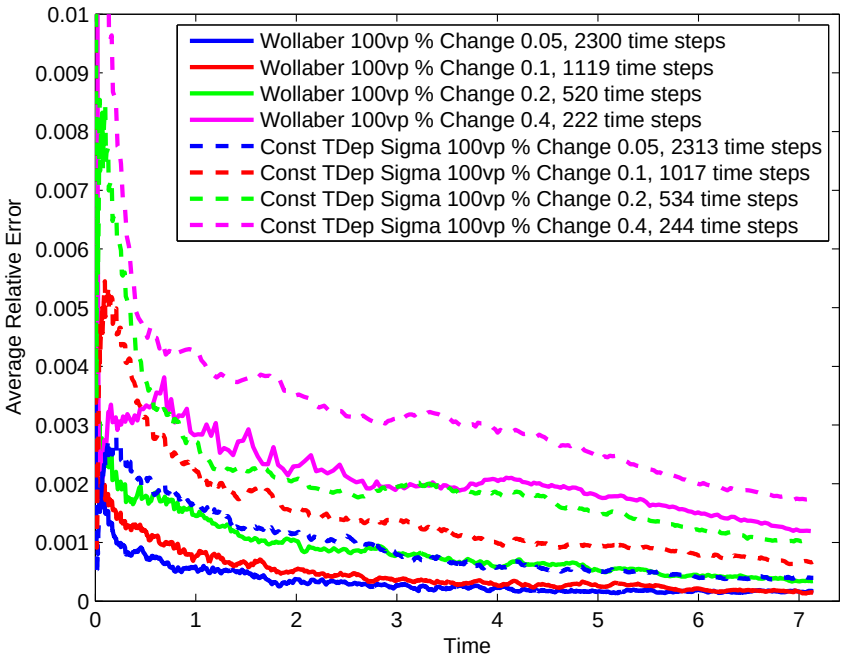

Figure 5.22: Average relative error in temperature of the CETDOPC and WLTPC using the opacity time step controller on Problem 9.

Comparing the WLTPC with the opacity time step controller to the simple opacity time step controller, it is clear in Fig. 5.23 that the WLTPC is much more accurate over the development of the problem. The least accurate WLTPC with opacity TSC

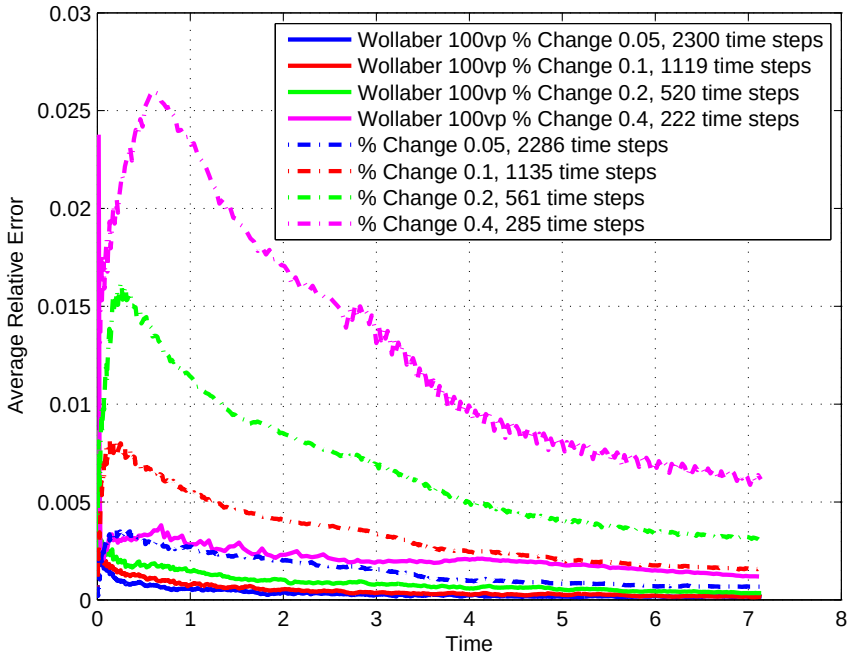

Figure 5.23: Average relative error in temperature of the CETDOPC and WLTPC using the opacity time step controller on problem 9.

run is competitive with the second most accurate opacity TSC approach. The WLTPC method yields an overall more accurate solution using 222 time steps ($\eta_{target} = 0.4$) compared to the opacity TSC use of 1135 time steps ($\eta_{target} = 0.1$). This represents a significant reduction in required time steps for a given accuracy. The numerical comparison between the different methods can be seen in Table 5.6.

Like in Problem 8, both the WLTPC and the CETDOPC give more accurate results for a similar number of time steps than the simple opacity TSC in Problem 9. The CETDOPC method is computationally competitive for a given accuracy with the opacity TSC approach for $\eta_{target} \leq 0.1$. Like in Problem 8, the WLTPC method appears to be the most accurate solution for a given run time up to $\eta_{target} = 0.05$. This dramatic improvement in accuracy over the simple opacity TSC can be seen again when applying the TAPC as seen in Fig. 5.24. This again reinforces the notion that the assumption of the opacity model is not the crucial assumption that makes the WLTPC with opacity TSC more accurate than the CETDOPC with opacity TSC.

Table 5.6: Characteristics of the opacity time step controller, WLTPC and CETDOPC with the opacity time step controller on Problem 9.

Average of the summed average relative error.			
% Change\Method	Opacity TSC	WLTPC	CETDOPC
0.4	0.01302	0.00222	0.00407
0.2	0.00676	0.00094	0.00234
0.1	0.00332	0.00056	0.00160
0.05	0.00145	0.00041	0.00097
Number of time steps used.			
% Change\Method	Opacity TSC	WLTPC	CETDOPC
0.4	285	222	244
0.2	561	520	534
0.1	1135	1119	1017
0.05	2286	2300	2313
Run time (wall time) for simulation in minutes.			
% Change\Method	Opacity TSC	WLTPC	CETDOPC
0.4	144.2	127.3	172.4
0.2	175.6	170.7	217.4
0.1	242.8	255.8	353.2
0.05	377.0	441.4	540.0

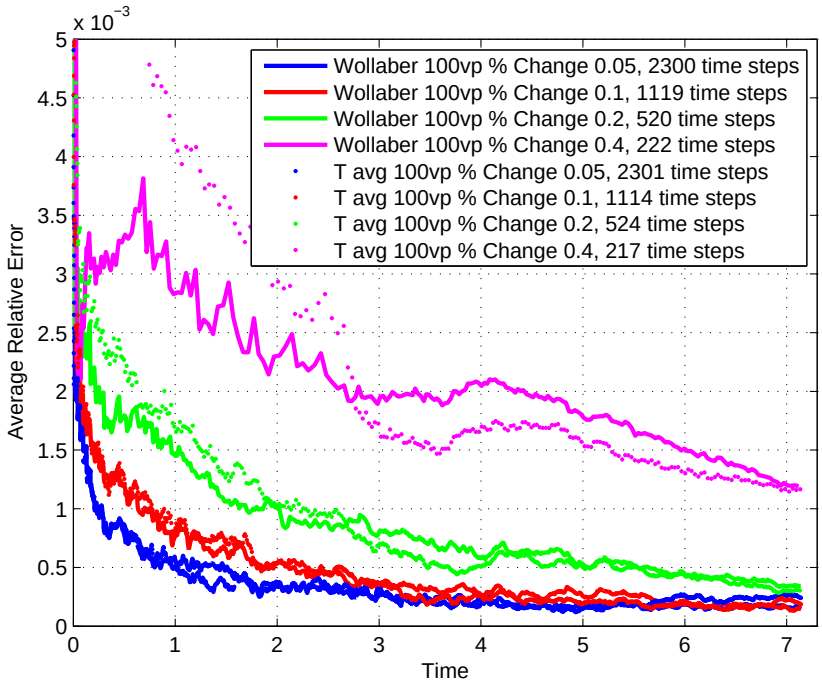

Figure 5.24: Average relative error in temperature of the WLTPC and TAPC using the opacity time step controller on Problem 9.

Chapter 6

Conclusions

In this thesis we have examined the Implicit Monte Carlo method in an attempt to better understand the effects of the assumptions used. Concurrently, the Carter-Forest method was also examined to compare and contrast the differences between these two methods. While both methods have been in existence for over thirty years, there has been little work detailing the sources of error in each approximation. The focus of this thesis has been detailing the sources of error in the equations and how this knowledge can be used to develop improved methods.

6.1 Chapter Review

In Chapter 2 we explored a 0D gray linear problem with both the IMC and CF method. In this particular problem, the CF method gives an exact solution to the linear coupled set of equations. This allowed us to examine the bias in the solution of the IMC method related to problem parameters and the user selection of parameter α. The results showed analytically that when $\alpha = 1$, the IMC method would maintain a cooler material temperature during a warming transient than would be physically correct. In contrast, during a cooling transient with $\alpha = 1$, the IMC method would yield a warmer material temperature than is physically correct. As the time step size Δt is decreased, the IMC bias is reduced. However, when $\alpha = 0.5$ the IMC bias became an $O(\Delta t^2)$ source of global error instead of $O(\Delta t)$. For stability reasons, $\alpha = 1$ is the common user choice.

Next, a detailed truncation analysis explored the propagation of error related to fixing the values of the opacity σ and parameter β as constant during a time step. Both the IMC and CF method turned out to be $O(\Delta t)$ error methods even though

the CF method makes fewer approximations. The detailed truncation analysis also demonstrated that the approximation of β as constant was not a leading source of error, while the approximation of σ as constant was. Because of this, a predictor-corrector method was introduced to improve the approximation of σ during a time step.

The analytical results of the predictor-corrector method showed that the Carter-Forest method was an $O(\Delta t^2)$ method globally while the IMC method remained $O(\Delta t)$ for a nonlinear problem. The IMC method with $\alpha \neq 0.5$ is only $O(\Delta t)$ because the IMC method has another leading order error term besides the opacity truncation. This second leading order error is the IMC bias that was previously mentioned when $\alpha \neq 0.5$. These analytical results were confirmed numerically in Chapter 3.

In Chapter 3 we were able to demonstrate numerically the effects of the IMC bias in simplified problems. The expected influence of the user selected parameter α on the resulting temperature bias can be seen in different linear and nonlinear problems. Furthermore, this bias is eliminated only when $\alpha = 0.5$. These results verify the analytical results that were produced in Chapter 2 with the residual error analysis.

Next, the predictor-corrector method was implemented numerically. The CF method becomes an $O(\Delta t^2)$ method globally in the 0D Gray nonlinear problem using a predictor-corrector scheme. However, the IMC method was shown to be an $O(\Delta t)$ accurate method even when the previously mentioned predictor-corrector was applied. Applying a predictor-corrector with the value of $\alpha = 0.5$, the IMC method becomes $O(\Delta t^2)$ accurate. This result confirms that the leading error terms in the IMC solution come from the estimation of the opacity and the bias introduced by assumption of the functional form of $U_r(t)$ in Eq. 2.66.

The order of accuracy for both the IMC and CF methods is confirmed using different variations on the predictor-corrector scheme. A predictor-corrector that averages opacity, averages temperature, or preserves the time integrated average opacity can be used successfully to improve the order of error of the CF method (and IMC method if $\alpha = 0.5$). Therefore both the CF and IMC method can gain significant improvements by using a predictor-corrector scheme. However, the IMC method may have unphysical behavior when $\alpha \neq 1$.

Chapter 4 introduces a spatial dependency into the Gray Thermal Radiative Transfer (GTRT) equations; this requires spatial discretization. This discretization adds another source of error into the solution of the equations, known as "photon teleportation." Photon teleportation occurs because of the difference between the distribution of absorption locations and the emission locations within a cell. When the difference of these two distributions becomes large, unphysical transport phenomenon

can occur. Photon teleportation can change the amount of energy that leaks from a cell, causing significant alteration of the Marhsak wave front location. Functional Expansion Tallies (FET's) are introduced to minimize the effect of photon teleportation. Using the Legendre Polynomial Maximum Entropy FET, significant reduction in photon teleportation is observed over different types of problems.

Like the zero dimensional results, the one dimensional results also show the IMC bias. In these spatially dependent problems, the IMC bias is usually most pronounced at the wave fronts where the difference between $cU_r(t)$ and $\phi(t)$ is the largest. The bias can significantly alter the wave front location and shape when a large time step size is used. As the time step size is decreased, the bias in the IMC method is reduced and the solution approaches the same solution as the CF method.

Predictor-corrector methods become more complicated with the addition of a spatial dependence in the problem. Unlike in the zero dimensional results, a simple opacity estimation will yield poor results except for very small time step sizes. While the predictor-corrector method using the Wollaber-Larsen temperature estimate yields a more accurate result, it assumes a functional form of the opacity. A new predictor-corrector method is therefore introduced called the Time Dependent Opacity predictor-corrector (TDOPC).

The TDOPC uses the predictor step's estimate of the opacity at time t_{n+1} and then assumes a linear dependency from the beginning to the end of the time step as $\sigma(t) = (\sigma_{n+1} - \sigma_n)\frac{t-t_n}{\Delta t} + \sigma_n$ where $t_n \leq t \leq t_{n+1}$. In the corrector step, a particle is born or taken from the time census at a given time $t^{'}$ with an opacity $\sigma(t^{'})$. Next, the distance to next collision must be determined in an optically changing media. A direct solution technique is employed to solve for the flight distance, requiring a transcendental root solve for each particle move. While this technique is accurate, it is computationally costly to employ. To simply this procedure, a Constant Emission Time Dependent Opacity predictor-corrector (CETDOPC) was created.

The CETDOPC method still employs the time dependent opacity technique by assuming a linear interpolation between the beginning and end of time step opacities, however the opacity is kept constant between interactions. In other words, a particle is tracked starting at time $t^{'}$ with a constant opacity $\sigma(t^{'})$. At the next interaction at time t^{*}, the opacity is updated to $\sigma(t^{*})$ and this is treated as constant until the next interaction. Since the CETDOPC method does not require a root solve for every transport distance, it is much faster than the TDOPC method, yet it achieves a similar accuracy.

However, all predictor-corrector methods can be computationally costly since the

time step must be run twice. To reduce the required computation time, a Variable-Weight Predictor-Corrector (VWPC) scheme is introduced. The VWPC uses a different number of particles to simulate the predictor step than the number that is used in the corrector step. Fewer particles with higher energy-weight are used in the predictor step to get a rough estimate of the end of time step values. Then the original number of particles at their normal weight are used in the corrector step. The result is that the VWPC scheme drastically reduces the run time of every predictor-corrector scheme while maintaining similar accuracy. For an IMC simulation, shown in Fig. 4.23a, with a given accuracy of 0.008, the 100VWPC WLTPC run required 148 minutes while the traditional IMC approach required 173 minutes. This time change represents a %14 reduction in required computation time for the same accuracy.

Chapter 5 introduces a new implementation of time step controllers in Radiative Transfer. Traditionally, the relative change of temperature in the radiation or material field has been used as a heuristic to determine the size of the next time step. In practice, using the relative change of temperature in the radiation field as proposed by Knoll and Rider (8; 18) does not work effectively in a Monte Carlo simulation due to excessive noise (4). Furthermore, this heuristic is fundamentally a poor constraint since a percent change in the temperature of the radiation field has no clear effect on the change of material temperature or the error terms in the discrete equations. In a non-homogeneous problem, the heat capacities of different materials will affect the material temperature response to a given energy deposition.

By examining the truncation analysis that was developed in Chapter 2, we have developed a time step controller that controls the change of opacity. Since the change of opacity is a leading source of error in the radiative transfer solutions, controlling the change of the opacity should directly control simulation error. Controlling the change of opacity is also more intuitive since if the opacity has changed by eighty-percent, say, over one time step, there can be little confidence that the radiation transport simulation for that time step bears much resemblance to the actual problem. The time step controller based on the change of opacity is correlated strongly with the number of time steps required to conduct a simulation. For example, by making the constraint smaller by a factor of two, the required time steps are roughly doubled for a given simulation. In contrast, when examining the material temperature time step controller, there was no linear correlation between the constraint and the resulting number of time steps required.

The time step controller method was also combined with a predictor-corrector scheme. By using our variable weight predictor-corrector, an end of time step value

of the opacity can be estimated. Using this information, a new time step size can be determined for the corrector step to control the relative change in the opacity or material temperature. The value of the opacities or material temperatures is then linearly interpolated to determine the new time step size for the corrector step. The combined time step controller predictor-corrector scheme showed a great combination of accuracy with a significant reduction in the number of time steps required to arrive at a solution. The results of this chapter also indicated that the WLTPC and the TAPC approaches were nearly indistinguishable at smaller time step sizes. This was due to the common approximation between the two approaches that the temperature would change linearly from the beginning and end of time step temperatures for sufficiently small time step sizes.

The CF time step controller approach on Problem 8, shown in Table 5.5, had an accuracy of 0.00252 for a run time of 189 minutes. Using a time step controller with a variable weight predictor-corrector yielded an accuracy of 0.00264 for a run time of 128 minutes. Therefore the time step controller with variable weight predictor-corrector scheme was %32 faster than the basic implementation of the opacity time step controller. This is a significant reduction of computation time that is shown when using the combined time step controller and variable weight predictor-corrector scheme over a basic time step controller.

6.2 Future Work

The Legendre Polynomial Maximum Entropy (Legendre-ME) FET's proved to be a significant improvement over the current source tilting approach. However, the exponential form of the FET does not match the actual concave down shape of the Marshak wave in a nonlinear problem. Therefore, a higher order Legendre-ME FET should be examined. By allowing for another constraint, the Legendre-ME FET would have a functional form of

$$p(x) = \alpha \exp[\beta x + \gamma x^2]. \tag{6.1}$$

This new FET would allow for a shape that would better fit for the Marshak wave front.

The truncation analysis in Chapter 2 indicated that the time dependent Fleck factor proposed by Wollaber-Larsen could be an order Δt^2 method in 0D with a predictor-corrector. It is quite possible that the proposed method could have all of the

benefits of the CF method with the reduced computational cost of the IMC method. For this reason, and the general familiarity of the community with the IMC approach, a time dependent Fleck factor predictor-corrector warrants further examination.

To reduce the computational effort associated with the Time Dependent Opacity predictor-corrector, opacity tables depending on time could be generated for each material cell. While these tables would require additional memory and computation time at the beginning of a time step, they could be referenced quickly afterwards to determine flight distances. Of course, this procedure would probably only produce computational savings for large numbers of particles.

A more realistic time step controller should also be considered. This thesis has focused largely on the upper bounds of one constraint being used by the time step controllers. However, we have largely avoided examination of time step size selection which is a critical component of any time step controller. The crude time step selection by the DM controller should be replaced to avoid the large and abrupt changes in time step size selection. In practice, smoothly and slowly changing the time step sizes is preferred to not induce oscillations in the solution (21). By including a more realistic time step size selection, we will be able to test the effect of a realistic time step controller with the improved constraint against the current approach.

Finally, we should relax the assumption of a mono-energetic one dimensional universe.

Bibliography

[1] C. Ahrens and E.W. Larsen. An exact monte carlo method for linear radiative transfer problems. *Transactions of the American Nuclear Society*, 83:340–341, 2000.

[2] Forrest B. Brown and William R. Martin. Direct sampling of monte carlo flight paths in media with continuously varying cross-sections. *LA-UR-02-6530, Los Alamos National Laboratory*, 2002.

[3] Forrest B. Brown and William R. Martin. Improved method for implicit monte carlo. *American Nuclear Society Transactions*, 86:212–215, 2002.

[4] Tom Brunner. Personal communication. Email Communication, 2009.

[5] J. A. Fleck and J. D. Cummings. An implicit monte carlo scheme for calculating time and frequency dependent nonlinear radiation transport. *Journal of Computational Physics*, 8:313, 1971.

[6] Joe D. Hoffman. *Numerical Methods for Engineers and Scientists*. Marcel Dekker, Inc., second edition, 2001.

[7] Shunsuke Ihara. *Information Theory for Continuous Systems*. World Scientific Publishing Co. Pte. Ltd., 1993.

[8] D.A. Knoll, W.J. Rider, and G.L. Olson. Nonlinear convergence, accuracy, and time step control in nonequilibrium radiation diffusion. *Journal of Quantitative Spectroscopy and Radiative Transfer*, 70:25–36, 2001.

[9] Edward W. Larsen and Bertrand Mercier. Analysis of a monte carlo method for nonlinear radiative transfer. *Journal of Computational Physics*, 71:50–64, 1987.

[10] Carter L.L. and Forest C.A. Nonlinear radiation transport simulation with an implicit monte carlo method. *LA-5038, Los Alamos National Laboratory*, 1973.

[11] William R. Martin and Forrest B. Brown. Comparison of monte carlo methods for nonlinear radiation transport. In *American Nuclear Society Math and Computation Transactions*, 2001.

[12] William R. Martin and Forrest B. Brown. Comparison of monte carlo methods for nonlinear radiation transport. In *American Nuclear Society Math and Computation Slide Presentations*, 2001.

[13] Michael Scott McKinley, Eugene D. Brooks III, and Abraham Szoke. Comparison of implicit and symbolic implicit monte carlo line transport with frequency weight vector extension. *Journal of Computational Physics*, 189:330–349, 2003.

[14] Dimitri Mihalas and Barbara Weilbel-Mihalas. *Foundations of Radiation Hydrodynamics*. Dover Publications, INC., 1999.

[15] Scott Mosher and Jeffery Densmore. Stability and monotonicity conditions for linear, grey, 0-d implicit monte carlo calculations. *American Nuclear Society Transactions*, 93:520, 2005.

[16] Scott W. Mosher. Exact solution of a nonlinear, time-dependent, infinite-medium, grey radiative transfer problem. *Transactions of the American Nuclear Society*, 95:744–746, 2006.

[17] Gerald C. Pomraning. *The Equations of Radiation Hydrodynamics*. Dover Publications, INC., 2005.

[18] William J. Rider and Dana A. Knoll. Time step size selection for radiation diffusion calculations. *Journal of Computational Physics*, 152:790–795, 1999.

[19] Bingjing Su and Gordon L. Olson. An analytical benchmark for non-equilibrium radiative transfer in an isotropically scattering medium. *Annuals of Nuclear energy*, 24:1035–1055, 1997.

[20] Allan B. Wollaber. *Advanced Monte Carlo Methods for Thermal Radiation Transport*. PhD thesis, University of Michigan, 2008.

[21] Mike Zika. Personal communication. Informal Discussion, 2009.